De novo macrocyclic peptides for inhibiting, stabilising and probing the function of the Retromer endosomal trafficking complex

Kai-En Chen[1], Qian Guo[1], Yi Cui[2], Amy K. Kendall[3,4], Timothy A. Hill[5], Ryan J. Hall[1], Joanna Sacharz[6], Suzanne J. Norwood[1], Boyang Xie[3,4], Natalya Leneva[1,6], Zhe Yang[2], Rajesh Ghai[1,7], David A. Stroud[6], David Fairlie[5], Hiroaki Suga[8], Lauren P. Jackson[3,4], Rohan D. Teasdale[2], Toby Passioura[8,9], Brett M. Collins[1]*

1. The University of Queensland, Institute for Molecular Bioscience, St. Lucia, Queensland, 4072, Australia.
2. The University of Queensland, School of Biomedical Sciences, St Lucia, Queensland, 4072, Australia.
3. Department of Biological Sciences, Vanderbilt University, Nashville, TN 37232, USA.
4. Center for Structural Biology, Vanderbilt University, Nashville, TN 37232, USA.
5. ARC Centre of Excellence for Innovations in Peptide and Protein Science, Institute for Molecular Bioscience, The University of Queensland, Brisbane, Qld 4072, Australia.
6. Department of Biochemistry and Molecular Biology, Bio21 Molecular Science and Biotechnology Institute, University of Melbourne, Parkville, 3052 Victoria, Australia.
7. Current address: Cambridge Institute for Medical Research, Cambridge, CB2 0XY, UK.
8. Current address: CSL Ltd, Parkville, Victoria, 3052, Australia.
9. Department of Chemistry, Graduate School of Science, The University of Tokyo, 7-3-1 Hongo, Bunkyo-Ku, Tokyo 113-0033, Japan.
10. Sydney Analytical, School of Life and Environmental Sciences and School of Chemistry, The University of Sydney, Camperdown, New South Wales 2050, Australia.

***Corresponding author**: Brett M. Collins, Tel: +61-7-3346-2043, b.collins@imb.uq.edu.au

Running title: Cyclic peptides targeting Retromer

ABSTRACT (150 words)

The Retromer complex (Vps35-Vps26-Vps29) is essential for endosomal membrane trafficking and signalling. Mutations in Retromer cause late-onset Parkinson's disease, while viral and bacterial pathogens can hijack the complex during cellular infection. To modulate and probe its function we have created a novel series of macrocyclic peptides that bind Retromer with high affinity and specificity. Crystal structures show the majority of cyclic peptides bind to Vps29 via a Pro-Leu-containing sequence, structurally mimicking known interactors such as TBC1D5, and blocking their interaction with Retromer *in vitro* and in cells. By contrast, macrocyclic peptide RT-L4 binds Retromer at the Vps35-Vps26 interface and is a more effective molecular chaperone than reported small molecules, suggesting a new therapeutic avenue for targeting Retromer. Finally, tagged peptides can be used to probe the cellular localisation of Retromer and its functional interactions in cells, providing novel tools for studying Retromer function.

INTRODUCTION

Endosomal compartments serve as central hubs for transmembrane protein and lipid sorting, and as platforms for cell signalling. Transmembrane protein cargos that arrive in the endosomal network via endocytosis or anterograde trafficking are routed either for lysosomal degradation or recycling to other compartments including the trans-Golgi network (TGN) and the cell surface. Endosomal trafficking thus plays a pivotal role in maintaining cellular homeostasis and is controlled by a number of essential protein machineries [1-3].

The evolutionarily conserved Retromer complex is a 150 kDa heterotrimer composed of Vps35, Vps29 and Vps26; with two paralogues Vps26A or Vps26B in vertebrates [4]. Retromer is a master regulator of endosomal dynamics responsible for cargo sorting and recycling within tubulovesicular transport carriers [2, 5-9], and in higher eukaryotes cooperates with an array of cargo adaptors and accessory proteins to allow membrane recruitment, cargo sorting and trafficking to occur [2, 3, 10]. Known accessory or regulatory proteins include the small GTPase Rab7, the Rab7 GTPase activating protein (GAP) TBC1 domain family member 5 (TBC1D5), VPS9-ankyrin-repeat protein (VARP/Ankrd27), and Fam21, a subunit of the WASP and scar homology (WASH) complex. The known cargo adaptors are derived from the sorting nexin (SNX) protein family and include SNX3 and SNX27. SNX3-Retromer mediated trafficking is primarily thought to mediate the trafficking of cargos from endosomes to the TGN [11, 12], whereas SNX27-Retromer is important for retrieval of endocytosed cargos from endosomes back to the cell surface [13-15].

Retromer mutation or dysregulation in humans leads to defective endosomal and lysosomal function implicated in neurodegenerative disorders including Parkinson's disease (PD) [16-30], Alzheimer's disease (AD) [31-37] and amyotrophic lateral sclerosis (ALS)[38]. Notably, generalised dysregulation of endosomal, lysosomal and autophagic organelles is a common hallmark of neurodegenerative disorders including familial and sporadic AD, PD, ALS and hereditary spastic paraplegia (HSP) [20, 39-44]. Retromer dysfunction impacts endosomal and lysosomal homeostasis in neurons and microglia in multiple ways [20, 45]; involving deficits in regulatory protein interactions such as WASH and Leucine-rich repeat kinase 2 (LRRK2)[19, 23, 27], mis-sorting of specific endosomal cargos [18, 26, 28, 46-51], defects in mitochondrial function and mitophagy [21, 29, 52, 53], and other widespread deficiencies in lysosomal and autophagic degradation of toxic material [23, 24, 32, 34, 37, 54-57].

Retromer is also a prominent target hijacked by intracellular pathogens to facilitate their transport and replication. This includes viruses such as SARS-CoV-2, human immunodeficiency virus (HIV), hepatitis C virus (HCV), and human papilloma virus (HPV) [58-70], and intracellular bacteria such as *Coxiella burnetii* and *Legionella pneumophila* [71-77]. Mechanistic studies have shown that the secreted effector protein RidL from *L. pneumophila* binds directly to Vps29, competing with endogenous regulators TBC1D5 and VARP, inhibiting Retromer mediated cargo transport, and supporting the growth of *L. pneumophila* in intracellular endosome-derived vacuoles [71, 73, 76, 77]. Similarly, the minor capsid protein L2 from human Papilloma virus (HPV) is thought to hijack Retromer-SNX3-mediated endosomal transport by mimicking sequence motifs found in endogenous cargoes such as the cation-independent mannose-6-phosphate receptor (CI-MPR) and divalent metal transporter 1-II (DMT1-II) [63, 66, 78, 79].

Given the importance of Retromer in endosomal trafficking, neurodegenerative disease, and cellular infection, there is significant interest in developing molecular approaches to either inhibit or enhance Retromer activity. Inhibition of Retromer may provide a novel avenue for targeting infectious pathogens; with peptide-based inhibitors of Retromer, derived from the HPV L2 protein, able to reduce infection by HPV by slowing the normal retrograde transport of incoming virions [66, 78, 79]. Conversely, because of its neuroprotective role, it has been proposed that a Retromer-binding 'molecular chaperone' could be used to enhance Retromer function in diseases including AD and PD [80-83], with the goal of boosting normal endosome-dependent clearance pathways to reduce accumulation of toxic aggregates of proteins such as amyloid β (Aβ), tau and α-synuclein. Previously a small molecule called R55 (a thiophene thiourea derivative, also called TPT-260) was identified, which can bind with modest affinity to Retromer at the interface between Vps35 and Vps29 and stabilise its structure [84]. This molecule has since been shown to have activity in stabilising Retromer in cells, and as predicted can enhance the transport of essential receptors and reduce the accumulation of toxic material including Aβ and α-synuclein in cell, fly, and mouse models [54, 84-90]. Recently a derivative of R55 was found to improve Retromer stability and lysosomal dysfunction in a model of ALS [38]. Nonetheless, the low potency and specificity of these compounds mean that other molecules are actively being sought.

We have adopted a novel screening strategy, referred to as the RaPID (Random nonstandard Peptides Integrated Discovery) system, to identify a series of eight *de novo* macrocyclic peptides with high affinity and specificity for Retromer, possessing either inhibitory or stabilising activities. These peptides bind to Retromer with affinities (K_d) ranging from 0.2 to 850 nM and can be classified into two groups based on their binding sites. Most interact specifically with the Vps29 subunit, and crystal structures show that these peptides associate with a highly conserved pocket on Vps29 that is also used by the accessory proteins TBC1D5 and VARP, as well as the bacterial protein RidL, and are potent inhibitors of both TBC1D5 and VARP binding. We also identified one peptide, RT-L4, that shows significant promise as a molecular chaperone. RT-L4 stabilizes Retromer assembly via binding to the interface between Vps26 and Vps35, does not disrupt Retromer's association with known accessory proteins and cargo adaptors, and indeed allosterically enhances binding to several ligands including SNX27 and TBC1D5. Finally, we show that these macrocyclic peptides can also be used as tools for probing Retromer function. Using reversible cell permeabilization and fluorescent peptides, we demonstrate that they can specifically co-label Vps35-positive endosomal structures and can be used as baits for isolating Retromer from cells. These macrocyclic peptides thus provide novel research tools to enhance our understanding of Retromer-mediated endosomal trafficking and suggest potential new avenues for developing therapeutic modifiers of Retromer function.

RESULTS

Identification of highly potent Retromer-binding macrocyclic peptides

The procedure of the RaPID system (**Fig. 1A**) exploits the diverse molecular topology of macrocyclic peptide populations numbering >10^{12} unique sequences to enrich for and amplify low abundance, high-affinity ligands [27, 91-94]. We performed the RaPID selection using purified His-tagged human Retromer complex as bait: a puromycin-linked semi-randomized messenger RNA library, of the general form AUG-$(NNK)_{4-15}$-UGC, was translated in an *in vitro* translation reaction to generate peptides covalently linked to their cognate mRNAs through the puromycin moiety. Macrocyclization was effected through genetic code reprogramming of initiating AUG (methionine) codons to incorporate either *N*-chloroacetyl-L-tyrosine (ClAc-L-Tyr) or *N*-chloroacetyl-D-tyrosine (ClAc-D-Tyr), leading to spontaneous reaction with a downstream UGC-encoded cysteine to form a library of thioether bridged cyclic peptides each linked to their cognate mRNA (total diversity >10^{12} molecules). Retromer ligands were then identified through iterative cycles of affinity selection against immobilised Retromer complex followed by RT-PCR recovery, transcription and regeneration of peptide-mRNA fusion libraries, with deconvolution of the final enriched library achieved through next-generation sequencing.

We selected the four most abundant peptides from each of the ClAc-L-Tyr or ClAc-D-Tyr initiated libraries (**Fig. 1B**; **Fig. S1; Table S1**) for further characterisation, and each was synthesised using standard Fmoc chemistry. These were validated against the Retromer complex by surface plasmon resonance (SPR) and all were confirmed to bind very strongly to Retromer with affinities (K_ds) in the range of <0.2 to 30 nM (**Fig. S2**). Secondary SPR comparisons showed that these molecules also bound the purified Retromer complex from *Danio rerio* (zRetromer) (**Fig. S2**) and the thermophilic yeast *Chaetomium thermophilum* (ctRetromer) with a similar range of binding affinities, indicating that they associate with evolutionarily conserved sites in the complex.

Macrocyclic peptide binding to Retromer was validated using isothermal titration calorimetry (ITC). Among the eight cyclic peptides tested, six were confirmed to bind Retromer with nanomolar binding affinity while the peptides RT-D4 and RT-L3 were not sufficiently soluble for ITC experiments (**Figs. 1C and 1D; Table S2**). Affinities for Retromer measured by ITC were systematically lower but correlated well with those measured by SPR, ranging from 25 to 850 nM. These affinities are comparable to or better than the high affinities for the Retromer binding regulatory protein TBC1D5 (220 nM) [95], or the bacterial effector RidL (150 nM) [76, 77].

The Retromer structure consists of a long Vps35 α-helical solenoid, with Vps26A or Vps26B bound to the N-terminus and Vps29 bound at the C-terminus (**Fig. 1E**) [96-100]. We examined the specific subunits of Retromer required for binding each of the cyclic peptides by testing either Vps29 alone, Vps26A alone, the Vps35-Vps29 heterodimer, or sub-complexes of Vps26A with N-terminal fragments of Vps35 (**Fig. 1D; Table 1)**. Full-length Vps35 is relatively unstable on its own and was not tested separately. Interestingly, RT-D1, RT-D2, RT-D3, RT-L1 and RT-L2 all bind specifically to either Vps29 alone or to the Vps35-Vps29 heterodimer, but not to Vps26A. Their affinities for Vps29 alone were not significantly different to their

binding to the Retromer holo-complex or Vps35-Vps29 heterodimer, ranging from 8 to 783 nM. This indicates they bind specifically and exclusively to the Vps29 subunit. Although peptides RT-D4 and RT-L3 were not tested for binding specific subunits, it is likely they also bind to Vps29 as they possess a Pro-Leu motif that we show below mediates Vps29 interaction by the other five peptides (**Figs. 1B and 1E**).

In contrast to other peptides, RT-L4 did not bind to any of the Retromer subunits individually or to the Vps35-Vps29 dimer, but rather only to sub-complexes that contained *both* Vps26A and Vps35 (**Fig. 1C**). N-terminal fragments of Vps35 in complex with Vps26A, including $Vps35_{1-390}$, and $Vps35_{1-224}$ supported binding to the RT-L4 peptide with a similar affinity to the Retromer trimeric holo-complex, while $Vps35_{1-390}$ on its own did not (**Fig. 1D**). When Vps35 was truncated to the shortest region still capable of Vps26A interaction ($Vps35_{1-172}$) a small but consistent decrease in binding affinity was observed, suggesting that α-helix 8 in Vps35 (residues 175 to 195) of Vps35 contributes to the binding but is not essential. Overall, we have found that the cyclic peptides RT-D1, RT-D2, RT-D3, RT-L1 and RT-L2 (and likely RT-D4 and RT-L3) bind specifically to Vps29, but RT-L4 binding occurs at the interface between the Vps26A and Vps35 subunits (**Fig. 1E**).

Macrocyclic peptides bind to Vps29 through a conserved site mimicking endogenous accessory proteins

To understand the molecular basis of how the discovered macrocyclic peptides bind to Retromer, we next co-crystallized Vps29 with RT-D1, RT-D2, RT-D3, RT-L1 and RT-L2. With extensive crystallization trials, we successfully solved structures of human Vps29 in complex with RT-D1, RT-D2, RT-L1 and RT-L2 (**Fig. 2; Table S3**). For RT-D3, the complex structure was successfully determined using Vps29 from *C. thermophilum* (ctVps29). In all five complex structures the conformation of Vps29 is highly similar to apo Vps29 (root mean square deviation ranges from 0.6 Å to 1.3 Å), with cyclic peptide density clearly visible (**Fig. 2A; Fig. S3A**). Surprisingly, although the precise details differed for each macrocyclic peptide, they all bound to the same hydrophobic surface groove on Vps29 composed of multiple conserved residues including Leu2, Leu25, Leu152, Tyr163, Tyr165 and Val174 (human numbering) (**Fig. 2B**). This hydrophobic cavity is highly conserved throughout evolution (**Fig. 2B**) and is located on the opposite surface of Vps29 relative to the Vps35 binding region (**Fig. 2C**).

Each cyclic peptide adopts a different conformation when bound to Vps29, as expected from their lack of sequence identity (**Fig. 2D; Fig. S3B**). However, a notable feature of all of the Vps29 binding peptides is a Pro-Leu di-peptide motif present in a β-hairpin structure that inserts into the conserved hydrophobic site on Vps29 (**Fig. 1B; Figs. 2D and 2E**). Further analysis reveals the residue in front of the Pro-Leu motif (position -1, with the Pro designated as position '0') is important for stabilizing the β-hairpin like configuration, forming multiple hydrogen bonds with nearby residues including the side-chain hydroxyl group of Vps29 Tyr165 (**Figs. 2D and 2E**). Notably TBC1D5, VARP and the bacterial hijacking molecule RidL all engage Vps29 at the same site, employing a similar Pro-Leu dipeptide at their core (**Fig. 2F**) [71, 76, 77, 95, 101-103]. The Vps29-binding peptides that we have identified thus mimic these natural interactions but exhibit higher affinities.

In addition to the core Pro-Leu di-peptide motif, the residues at positions +4 to +7 of the cyclic peptides also form extensive contacts with a surface groove composed of Vps29 side chains Val172, Lys173 and Val174 (**Fig. 2D; Fig. S3B**). This particular interaction network is shifted by 8 Å towards Lys188 in the ctVps29 – RT-D3 structure (equivalent to Arg176 in human Vps29), which may explain the weaker binding of ctVps29 to RT-D3 compared to Vps29 (**Fig. 2D; Fig. S3C**). To confirm that the Pro-Leu motif is a key feature for these cyclic peptides to recognize Vps29, we altered the Leu at position +1 in RT-D1 to Glu, binding to Retromer was almost abolished (**Fig. 2G**). Another noteworthy observation was found in the Vps29 – RT-L1 structure, where a potential secondary cyclic peptide binding pocket was identified, surrounded by helix 3 and Ile91 of Vps29 (**Fig. S3D**), a region known to be required for Vps35 binding. In this binding pocket, we found two RT-L1 peptides are bound to each other, forming extensive contacts with residues located on helix 3 and adjacent loop region of Vps29 (**Fig. S3E**). This binding of RT-L1 to a secondary site in Vps29 is likely due to a crystallisation-induced contact, but it could suggest a potential site for targeting the Vps29-Vps35 interaction in the future.

The RT-L4 macrocyclic peptide is a molecular chaperone that binds to the interface between Vps26A and Vps35

One of our initial goals was to identify potential molecular chaperones that can stabilise the Retromer complex, hence we next assessed the impact of the macrocyclic peptides on the thermal stability of Retromer using differential scanning fluorimetry (DSF) (**Fig. S4A**). The Vps29-binding peptides RT-D1, RT-D2, RT-D3, RT-L1 and RT-L2 all increased the melting temperature (T_m) of Vps29 upon addition of a 20-fold molar excess (**Fig. S4A**), consistent with their high affinities. In contrast however, none of the Vps29-specific macrocyclic peptides had a significant impact on the thermal stability of the trimeric Retromer holo-complex (**Fig. S4B**). This suggests that increasing the thermal stability of Vps29 alone is insufficient to enhance the stability of the entire Retromer complex in solution. In contrast, the addition of RT-L4 resulted in a substantial 2°C to 6.5°C enhancement in the T_m of the Retromer holo-complex in a dose-dependent manner (**Fig. 3A; Figs. S4C and S4D**). Similarly, the RT-L4 peptide resulted in an 8°C increase in T_m for the Vps26A-Vps35$_{1-390}$ sub-complex, and as expected in control experiments it did not affect the thermal stability of either Vps26A or Vps29 alone (**Fig. S4C**). Using mass photometry, we found that the Retromer holo-complex was maintained at its trimeric state upon the addition of cyclic peptides, suggesting that the enhancement in the T_m of the Retromer was not the result of high-order oligomer formation (**Fig. S5A**). These results together indicate that RT-L4 stabilizes Retromer through its interaction at the interface between Vps26A and Vps35, possibly by acting as a molecular 'staple' between the two subunits. In parallel, we also compared the thermal stability effect of RT-L4 against the previously published Retromer chaperone R55 [84]. Surprisingly we were unable to detect any improvement in the T_m of Retromer in the presence of R55 under the same experimental conditions as RT-L4 (**Fig. S5B**). Even in the presence of 1 mM R55 (> 300-fold molar excess) no impact on Retromer stability was detectable (**Fig. S5C**), although a second unfolding event was observed that might indicate partial stabilisation of the Vps29-Vps35 complex [84]. This difference is likely explained by the much lower binding affinity of R55 to

193 Retromer with a K_d of 15 μM (**Fig. S5D**). Our results indicate that RT-L4 can act as a potent molecular
194 stabiliser of Retromer in solution.

195 Next, we sought to map the exact binding region of RT-L4 to better investigate the mechanism of its
196 interaction and how this results in the enhanced thermal-stability of Retromer. Using ITC we found that RT-
197 L4 binds to zRetromer with a K_d of 80 nM, which is highly comparable to human Retromer or the Vps26A-
198 Vps35$_{1-390}$ sub-complex (**Table S2**; **Fig. S6A**). In contrast, RT-L4 binds with lower affinity to ctRetromer with
199 a K_d of 6 μM (**Table S2**; **Fig. S6B**). As our data indicated that RT-L4 binds to a site that is formed by a
200 combined interface on Vps35-Vps26A, to investigate the residues required to the binding we performed
201 directed mutagenesis of residues surrounding the human Vps35-Vps26A interface based on the previous
202 crystal structure [98]. Streptavidin agarose beads coated with biotinylated RT-L4 were used to pulldown purified
203 Vps26A-Vps35$_{1-390}$ incorporating several specific point mutations, and this revealed that peptide binding was
204 abolished by the D128R mutation in Vps35 (**Fig. 3B**). The Asp128 side-chain is part of a conserved surface
205 adjacent to the Vps35-Vps26A interface (**Fig. 3C**), and makes a minor contact with the extended N-terminus
206 of SNX3 when in a ternary complex with the SNX3 adaptor and ΩΦ[LV] sequence containing-cargo peptides
207 (where Ω and Φ are aromatic and hydrophobic side-chains) [3, 98].

208 We further explored validated the site where RT-L4 binds Retromer using single particle cryo-electron
209 microscopy (cryoEM). In previous work, wild-type Retromer was found to form a mixed population of
210 hetetrotrimers and multiple higher order oligomers in vitreous ice, so we used an established mutant called
211 "3KE Retromer" (point mutations E615A/D616A/E617A in Vps35) that favours the heterotrimeric species
212 over higher order oligomers for our analyses [100]. We determined structures of both apo and RT-L4-bound 3KE
213 Retromer under the same conditions to ascertain whether the RT-L4 binding site could be identified (**Fig. 3D-**
214 **F**; **Figs. S6C-F**; **Table S4**). At the current resolution we detected no structural differences between wild-type
215 heterotrimer [100] and the 3KE mutant. Comparison of our reconstructions indicates there is additional density
216 at the Vps26-Vps35 interface in the presence of the RT-L4 peptide, although the estimated resolution of apo
217 and RT-L4/Retromer structures (~5.0 Å; 0.143 FSC cut-off in RELION) is too low to unambiguously assign
218 peptide density (**Figs. 3D-F**; **Figs. S6C and S6D**). We note RT-L4/Retromer exhibits more preferred
219 orientation in vitreous ice than does apo Retromer, which limits particle views (**Fig. S6D**). We observe "top-
220 down" views of RT-L4/Retromer, but we lack views rotated by 180 degrees (**Fig. S6D**). One explanation for
221 this difference may be relatively low solubility for the RT-L4 peptide, which in turn may influence how RT-
222 L4/Retromer behaves at the air-water interface. Although not conclusive, these reconstructions support our
223 biophysical and mutagenesis data, providing additional evidence RT-L4 binds and stabilizes Retromer at the
224 Vps26/Vps35 interface, but higher resolution data will be required to identify residues in both Retromer and
225 the peptide that specifically mediate the interaction.

226

227 ***The impact of cyclic peptides on the interactions between Retromer and known regulatory proteins***

228 Given the high affinity and specificity of the macrocyclic peptides for Retromer, it was critical to assess their
229 potential effects on Retromer's interaction with essential regulatory, accessory and adaptor proteins. We used
230 RT-L4, with its distinct affinity for the Vps26-Vps35 complex, and RT-D3 as a representative Vps29-binding
231 peptide, and tested Retromer binding proteins for which binding mechanisms were known including
232 TBC1D5[95], SNX3[98], Fam21[104], and SNX27[105] (**Figs. 4A-E**). GST-tagged TBC domain of human TBC1D5
233 ($TBC1D5_{TBC}$) bound Retromer in pulldowns, and this interaction was inhibited by addition of RT-D3 as
234 expected based on their overlapping binding site (**Fig. 4A**). A similar result was observed using ITC, where
235 we observed binding between $TBC1D5_{TBC}$ and Retromer with a K_d of 370 nM (consistent with previous reports
236 [95]), while binding was undetectable in the presence of competing RT-D3 (**Fig. 4B, Table S5**). In contrast,
237 while the addition of RT-D3 blocked Retromer from interacting with $TBC1D5_{TBC}$ as would be predicted from
238 their overlapping binding sites, it had no impact on Retromer binding to either SNX27 or SNX3 as assessed in
239 pulldowns and ITC experiments (**Figs. 4A, 4C, and 4D**). Note that for ITC and pull-down experiments with
240 SNX3, we found it was necessary to include a synthetic peptide corresponding to DMT1-$II_{550-568}$ containing a
241 ΩΦ[LV] cargo motif (where Ω = an aromatic side-chain and Φ = a hydrophobic side-chain) [98]. In the absence
242 of this peptide we could not detect binding of SNX3 to Retromer, likely because SNX3 and cargo motifs form
243 a co-dependent binding interface with the Retromer complex [3, 98]. To our surprise, the addition of RT-D3
244 modestly affected Retromer binding to Fam21 C-terminal LFa repeats 19 to 21 (**Figs. 4A and 4E**), a sequence
245 known to associate with a C-terminal region of Vps35 [19, 104]. It is therefore likely that Vps29 contributes
246 partially to the binding of LFa sequences of Fam21, and RT-D3 either directly competes with Fam21 or
247 allosterically affects the Fam21 binding site. These results were further validated using qualitative pulldowns
248 from HeLa cell lysates with biotinylated RT-D3 peptide, where specific loss of TBC1D5 and VARP binding
249 was seen, without any effect on the association of other Retromer ligands SNX27, Fam21, SNX3 and SNX27
250 (**Fig. 4F**). Altogether our data indicates RT-D3 can specifically inhibit binding to TBC1D5, and most likely
251 will also compete with other proteins such as VARP and RidL that bind to the same conserved hydrophobic
252 cavity on Vps29.

253 In contrast to RT-D3, we found that the RT-L4 peptide had little negative impact on the interaction of
254 Retromer with any ligands tested. In GST-pulldowns using purified proteins or using biotinylated peptides and
255 HeLa lysates Retromer was able to interact with TBC1D5, VARP, Fam21, SNX27 and the SNX3-DMT1-II
256 complex in the presence of RT-L4 (**Figs. 4A and 4E**). Interestingly, by ITC we found that the affinity and
257 enthalpy of binding between Retromer for either $SNX27_{PDZ}$, $TBC1D5_{TBC}$, or $Fam21_{R19-R21}$ were substantially
258 improved by the addition of RT-L4 (**Figs. 4B, 4D and 4E; Fig. S7A; Table S5**). Binding between $SNX27_{PDZ}$
259 and PDZ-dependent cargo peptide, $PTHR_{586-593}$, was also further improved to a K_d of 700 nM by the presence
260 of RT-L4 (**Fig. 4G**). This suggests that the stabilization of Retromer by RT-L4 may be able to enhance binding
261 to some of its key partners and possibly also improve cargo recognition. However, we did observe a modest
262 reduction in the binding affinity of Retromer for the SNX3-DMT1-II complex from 154 μM to 230 μM in the
263 presence of RT-L4 (**Fig. 4C; Table S6**). We speculate that there may be a small degree of overlap between
264 the binding site for RT-L4 and the first part of the N-terminal loop of SNX3, although not enough to perturb

265 the interaction dramatically. Given this subtle change however, we then asked whether the peptide would
266 perturb the interactions between Retromer and SNX3 in the presence of a lipid membrane. To do this, we
267 performed a liposome binding assay, where we fused a palmitoylated fatty acid to the N-terminus of a cargo
268 peptide. For these experiments we used a sequence derived from the CI-MPR ($CIMPR_{2347-2376}$) and allowed it
269 to insert into liposomes compose of Folch I lipids supplemented with the SNX3-binding phosphatidylinositol-
270 3-phosphate (PtdIns3*P*) (**Fig. 4H; Figs. S7B and S7C**). In our control experiments, we found that SNX3 alone
271 was capable of binding Folch I - PtdIns3*P* liposomes both in the presence and absence of cargo peptide. In
272 contrast, Retromer only bound stably to PtdIns3*P*-containing liposomes when both SNX3 *and* cargo peptides
273 were added, similar to previous studies [106]. In the presence of RT-L4 we observed a subtle reduction of
274 Retromer binding to SNX3-CI-MPR cargo-PtdIns3*P* liposomes, consistent with the slightly lower affinity
275 observed by ITC (**Fig. S7D**). In summary, peptides binding to Vps29 have a strong and specific impact on a
276 subset of Retromer-associated proteins including TBC1D5 and VARP, without affecting interactions that
277 occur near the Vps35-Vps26 interface (**Fig. 4I**). The stabilising RT-L4 peptide does not prevent binding of
278 any known ligands (**Fig. 4I**), which is an important property of a potential molecular chaperone, although it
279 does have subtle effects on these interactions depending on their respective binding sites.
280

281 ***RT-L4 reveals an unexpected autoinhibitory role for the C-terminal disordered tails of Vps26A and***
282 ***Vps26B***

283 During our analyses of RT-L4 we noted that it showed a lower binding affinity for the paralogous Vps26B-
284 $Vps35_{1-390}$ subcomplex when compared to Vps26A-$Vps35_{1-390}$ (**Fig. 5A; Table S2**). According to the sequence
285 alignment of Vps26, the residues responsible for Vps35 interaction are highly conserved, while the extended
286 C-terminal tails (residues 298 to 327 in Vps26A) are highly divergent apart from the QRF/YE motif (**Fig 5B;**
287 **Fig. S7E**). Strikingly when the disordered C-terminal domains of either Vps26A or Vps26B are removed
288 (Vps26AΔC and Vps26BΔC respectively) the binding affinity for RT-L4 is increased to ~40 nM K_d and is now
289 identical for both sub-complexes (**Fig. 5A**). We also find a similar improved affinity of RT-L4 for *C.*
290 *thermophilum* Retromer when the tail of Vps26 is removed (**Fig. S8**). This shows that the C-terminal tails of
291 Vps26A and Vps26B have an autoinhibitory effect on binding to RT-L4, with the Vps26B C-terminus
292 inhibiting the interaction more strongly.

293 Given that the RT-L4 peptide also subtly affects binding of Retromer to SNX3 and cargos, we were
294 interested to determine whether the C-terminal tails of Vps26 might also influence SNX3 interactions.
295 Intriguingly, SNX3 (in the presence of DMT1-II cargo) binds to Vps26AΔC-$Vps35_{1-390}$ with a significantly
296 increased affinity compared to full-length Vps26A-$Vps35_{1-390}$ (**Fig. 5C; Table S2**). This suggests that there is
297 a self-association of the C-terminal tail that weakens the SNX3-cargo interaction. Previous proteomics have
298 shown that the C-terminal disordered sequences of human and mouse Vps26A and Vps26B can be
299 phosphorylated, although the role of these post-translational modifications (PTMs) and their regulation has
300 not been studied [107] (**Fig. 5B)**. We engineered a Vps26A variant with three phosphomimetic mutations in its

301 C-terminal tail and tested the affinity of the $Vps35_{1-390}$/Vps26A phosphomimic complex for SNX3 in the
302 presence of DMT1-II by ITC (**Fig. 5C**). Interestingly this mutant showed an enhanced affinity to the cargo-
303 adaptor complex, although not to quite the extent of the complete removal of the Vps26A tail. Similar
304 enhancement of binding to SNX3 cargo-adaptor complex was also observed when we mutated the conserved
305 QRFE motif of Vps26A to polyalanine (**Figs. 5D and 5E**). Together, our data indicates that the tails of Vps26A
306 and Vps26B play an unexpected autoinhibitory role in the functional interaction of Retromer with the SNX3
307 adaptor and associated cargos such as Dmt1-II and CI-MPR, and phosphorylation of these tails could activate
308 Retromer to enhance SNX3-cargo interactions (**Fig. 5F**). Vps26B is more strongly autoinhibited than Vps26A,
309 and this observation would explain previous studies showing that the CI-MPR does not bind to Retromer
310 containing Vps26B in cells, but that deletion of the Vps26B tail allows CI-MPR interaction to occur [108].
311
312 ***Macrocyclic peptides as molecular probes to study Retromer mediated endosomal trafficking***
313 With established mechanisms of binding *in vitro* we sought to assess the basic utility of these macrocyclic
314 peptides as novel molecular tools for the study of Retromer. In the first instance we examined their use as
315 fluorescent probes of Retromer localisation in cells (**Fig. 6**). As the peptides were not membrane permeable
316 for cellular uptake we used a reversible cell permeabilization approach with the pore-forming bacterial toxin
317 Streptolysin O (SLO) [109]. After permeabilization cells were treated with FITC-labelled RT-D3 and RT-L4 and
318 then processed for imaging and co-labelling with specific endosomal markers. In the absence of SLO
319 permeabilization no intracellular fluorescence was detected for the FITC-labelled peptides indicating they are
320 not crossing the membrane or being non-specifically internalised into the lumen of endosomal compartments
321 (**Fig. 6A**). In permeabilised cells however, both FITC-labelled RT-D3 and RT-L4 were recruited to endosomal
322 structures labelled with SNX1 (**Fig. 6A**). Using Airyscan super-resolution microscopy we found that the
323 peptides also co-labelled endosomal structures marked with mCherry-tagged Vps35 (**Fig. 6B**). Lastly, we
324 examined the impact of the peptides on the endosomal recruitment of TBC1D5, which has previously been
325 shown to depend on interaction with Retromer [71, 76, 77, 95, 110]. As expected, addition of unlabelled RT-L4 had
326 no discernible effect on TBC1D5 localisation; however, RT-L3, which binds to the same site on Vps29 as
327 TBC1D5, caused significant dispersal of TBC1D5 from endosomal structures (**Fig. 6C**). Overall, our data
328 suggests that the Retromer-binding macrocyclic peptides are capable of acting as molecular probes for
329 Retromer localisation.
330
331
332

DISCUSSION

De novo macrocyclic peptides that target the Retromer endosomal trafficking complex

In this work the versatile RaPID screen was used to identify a series of potent Retromer-targeting macrocyclic peptides. These bind with high affinity and specificity to Retromer using two distinct evolutionarily conserved binding sites on either Vps29, or at the interface between Vps26 and Vps35. The cyclic peptides in the inhibitor sub-group (RT-D1, RT-D2, RT-D3, RT-L1 and RT-L2) reveal strong binding through the highly conserved surface groove of Vps29, lying on the opposite surface to that bound by the Vps35 subunit. Detailed structural analyses showed that these cyclic peptide inhibitors all form a β-hairpin configuration with a core Pro-Leu motif. Although not tested here, it is likely that these will also be effective at blocking association with the bacterial hijacking molecule RidL, which is known to bind the same site as TBC1D5 and VARP using a similar β-hairpin structure [71, 76, 77]. It is intriguing that all of the Vps29-binding peptides have been selected for the presence of this Pro-Leu dipeptide, and that this peptide has also evolved to mediate binding of endogenous ligands of the Retromer complex such as TBC1D5, VARP and the bacterial effector RidL. The *de novo* macrocyclic peptide screening has therefore inadvertently identified an evolutionarily conserved binding mechanism, and interestingly previous screens of BET domain-binding peptides also uncovered sequence preferences that partly mimicked known endogenous ligands [111]. Given that Vps29 is also a component of the Retriever complex, a Retromer-related assembly containing homologous subunits Vps35L/C16orf62 and Vps26C/DSCR3 [112, 113], these cyclic peptide inhibitors may provide valuable tools for studies of Retriever. Although whether the same binding site in Vps29 is accessible within the Retriever complex remains to be confirmed.

Among the identified macrocyclic peptides RT-L4 binds specifically to the interface between the N-terminal domain of Vps35 and the C-terminal sub-domain of Vps26 and is the sole molecule to show a significant ability to stabilise the Retromer complex. In the recent cryoEM structure of mammalian Retromer it was found that Vps26 and the N-terminal portion of Vps35 exhibit substantial flexibility compared with other regions of the complex [100]. We speculate that the improved thermal stability of Retromer in the presence of RT-L4 may be partly due to reduced flexibility in these two subunits. Importantly, the RT-L4 peptide did not inhibit the binding of Retromer to its essential interacting partners including SNX27, Fam21, TBC1D5 and VARP, and in fact led to a general increase in their binding affinity *in vitro*. RT-L4 did have a minor effect however on binding of Retromer to SNX3 and ΩΦ[LV] motif-containing cargo, consistent with the fact that the RT-L4 binding site partially overlaps with the site where the N-terminal disordered domain of SNX3 engages Vps26 and Vps35 [98].

Macrocyclic peptides as molecular tools for the study of Retromer function

The series of macrocyclic peptides discovered here provide novel molecular probes for the study of Retromer and endosomal trafficking. Firstly, using a simple reversible permeabilization approach, we have successfully delivered the cyclic peptides RT-D3 and RT-L4 into cells and find they are specifically targeted to the

369 Retromer-positive endosomal structures. Thus, the peptides can be used to examine endogenous Retromer
370 localisation *in situ* and could feasibly be used to study Retromer in live cells or using super-resolution
371 approaches with different types of fluorescent dyes apart from the simple FITC labelling strategy used here.
372 The RT-D3 peptide also impacts recruitment of proteins such as TBC1D5 that depend on binding to the Vps29
373 subunit of the complex, and therefore could be used to probe the impact of acutely disrupting this interaction
374 in the future. In addition to studying the localisation of Retromer, the RT-L4 peptide provided a highly specific
375 substrate for purification of the Retromer complex from cells, and in the future could be useful for proteomic
376 studies of Retromer in diverse cells, tissues, and organisms. We also envisage that these peptides will provide
377 tools for enhancing Retromer stability for future structural studies of its interactions with accessory and
378 regulatory proteins by cryoEM and X-ray crystallography.

379 Our studies of the RT-L4 peptide binding to the Vps26–Vps35 interface revealed an autoinhibitory role
380 for the C-terminus of the Vps26A and Vps26B paralogues. Removal of their divergent C-terminal tails
381 significantly increased the affinity of both Retromer complexes for the RT-L4 peptide to similar levels, leading
382 us to then test the impact of the Vps26A and Vps26B tail domains on binding to the SNX3–DMT1-II cargo-
383 adaptor complex, a native ligand that engages Retromer at a similar location. Again, removal of the C-terminal
384 disordered domains significantly improved the affinity of Retromer for SNX3–DMT1-II, confirming their
385 autoinhibitory activity has a functional importance. Furthermore, this may be regulated by phosphorylation of
386 the Vps26A and Vps26B tails, as phosphomimetic mutants have a higher affinity for SNX3-DMT1-II than the
387 wild-type proteins. Since the discovery of the Vps26B paralogue of Vps26A it was clear that the most
388 significant difference between the two proteins was the sequence of their C-terminal domains [4, 114]. Later it
389 was shown that Vps26A but not Vps26B Retromer bound to the SNX3-dependent cargo CI-MPR, however,
390 CI-MPR binding and trafficking by Vps26B was restored when its tail was deleted [108]. Our data demonstrates
391 a direct role for both the Vps26A and Vps26B tails in negatively regulating the binding of SNX3-cargo *in*
392 *vitro*, with the Vps26B tail possessing a more potent autoinhibitory sequence than that of Vps26A. This
393 suggests that an activating switch such as phosphorylation of Vps26 proteins or binding of another regulatory
394 protein may promote the recruitment of SNX3-cargo complexes by Retromer in cells, although the specific
395 nature of this switch remains to be determined.

396

397 ***Towards therapeutic targeting of Retromer***

398 Endolysosomal trafficking and regulation of proteostasis is emerging as an attractive target in the treatment of
399 a range of diseases, including neurodegenerative disorders like AD and PD, infection by viral and bacterial
400 pathogens, and other diseases impacted by defective endosomal signalling such as cancer. There is an
401 increasing interest in developing molecules for both inhibition and enhancement of Retromer activity in these
402 processes [20, 39, 40]. As shown previously, peptides that target Retromer and compete with the viral L2 protein
403 can reduce HPV infection in cell and animal models [66, 78, 79], while a small molecule with Retromer chaperoning
404 activity can reduce cellular accumulation of toxic material causing neurodegeneration [54, 80-90]. However, these

405 peptides and small molecules have only a relatively low affinity for Retromer, and their specificities and
406 pharmacological profiles are essentially unknown.

407 Because of their typically high affinity and larger surface area coverage, macrocyclic peptides are
408 emerging as an important class of molecules for the design of new drugs and molecular probes targeting
409 proteins and protein-protein interactions, often considered difficult using traditional small molecule
410 approaches [93, 115-118]. The peptides we have discovered can be classified as either Retromer inhibitors or
411 stabilizers, and we provide a comprehensive biochemical and structural explanation for how each cyclic
412 peptide associates with Retromer and affects its native molecular interactions. The Retromer inhibitors we
413 identified were able to potently block TBC1D5 and VARP binding and will likely also preclude interaction of
414 the bacterial effector RidL, suggesting a conserved site in Retromer primed for targeting by peptide or small
415 molecule-based inhibition. The stabilising peptide RT-L4 enhanced Retromer association with known
416 regulatory proteins, and its mechanism of action and superior affinity to the R55 small molecule highlights the
417 potential of targeting the Vps26 and Vps35 interface for the design of novel pharmacological chaperones of
418 Retromer in future studies. While the macrocyclic peptides described here are potential leads to therapeutic
419 targeting of Retromer, notable hurdles include cell permeability, oral availability, and an ability to cross the
420 blood brain barrier when targeting neurological diseases. However, new approaches show promise in
421 overcoming these barriers, including the use of non-standard amino acids with novel activities and solubility
422 profiles, coupling to various cell-targeting peptides, and novel delivery methods [118-121]. Alternatively, the
423 peptides discovered here could provide the basis for competitive screening for drug-like molecules that target
424 the same binding sites.

425 In summary, we have identified a series of Retromer-targeting macrocyclic peptides and demonstrate
426 their potential for Retromer inhibition and activation based on a comprehensive understanding of their different
427 mechanisms of action. They will be a valuable resource for the study of Retromer function at the cellular and
428 molecular level and represent promising leads for the targeting of Retromer in a variety of diseases caused by
429 dysregulation or disruption of the endosomal membrane trafficking system.

430

431

432 **MATERIALS AND METHODS**

433 *Chemicals and antibodies*

434 Rabbit polyclonal anti-TBC1D5 was purchased from Proteintech (17078-1-AP). Mouse monoclonal anti-
435 SNX1 was purchased from BD Transduction Laboratories (611483). Mouse monoclonal anti–α-tubulin (clone
436 DM1A; T9026) was purchased from Sigma-Aldrich. Goat polyclonal anti-Vps35 (NB100-1397) was
437 purchased from Novus Biologicals. Secondary donkey anti-mouse IgG Alexa Fluor 647 (A31571), and donkey
438 anti-rabbit IgG Alexa Fluor 555 (A31572) were purchased from Thermo Fisher Scientific. The linear peptides
439 DMT1-II$_{550-568}$ (AQPELYLLNTMDADSLVSR) and palmitoylated CI-MPR$_{2347-2375}$ with N-terminal di-lysine
440 (KKSNVSYKYSKVNKEEETDENETEWLMEEIQ) were both synthesised by Genscript (USA).

441

442 *Molecular Biology and Cloning*

443 pmCherry-SNX1 was generated by subcloning the full-length open reading frame of human SNX1 from
444 pEGFP-SNX1 described previously [122], into the multiple cloning site of pmCherry-C1. pmCherry-Vps35 was
445 generated by subcloning the full-length open reading frame of human Vps35 from pEGFP-Vps35 described
446 previously [18], into the multiple cloning site of pmCherry-N1.

447 For bacterial expression, Retromer constructs encoding full-length human and zebrafish Vps29,
448 Vps26A and Vps35 were cloned into either pET28a and pGEX4T-2 vectors as described previously [99, 123].
449 *Chaetomium thermophilum* Vps29, Vps26 and Vps35 were also cloned using protocol described previously [97].
450 In all cases, Vps26A was cloned as a N-terminal His$_6$-tag fusion protein and Vps29 was cloned into pGEX4T-
451 2 vector as a cleavable N-terminal GST fusion protein. For mouse Vps26B, full-length cDNA was inserted
452 into pMW172Kan vector [114]. For the truncation constructs, the DNA sequence encoding the N-terminal part
453 of Vps35 (Vps35$_{1-172}$, Vps35$_{1-224}$ and Vps35$_{1-390}$) was cloned into pGEX4T-2 vector. Vps26 ΔC-term. tail (ΔC)
454 constructs (Vps26A$_{9-298}$ and Vps26B$_{7-296}$) were cloned into pET28a vector containing His$_6$-tag. Full-length
455 Vps26A pm mutant (substituted S315E, S318E and S321E), Vps26A$_{QRFE-AAAA}$ (substituted residues 311 - 314
456 to alanine) and Vps26B pm mutant (S302E, S304E, S311E, S319E, T325E, S327E, and S330E substitution)
457 were synthetic genes by Genscript Corporation. cDNA encoding full-length human SNX3 was cloned into
458 pGEX4T-2 vector. Similarly, the cDNA encoding the human Fam21 LFa motif repeats 19 to 21 was cloned
459 into pGEX4T-2 vector. The TBC domain of human TBC1D5 was cloned into the pMCSG9 vector containing
460 a N-terminal GST and a TEV cleavage site. Full-length mouse SNX27 was cloned into the pMCSG7 vector
461 containing a N-terminal His and a TEV cleavage site [124]. PDZ domain of mouse SNX27 was cloned into the
462 pGEX4T2 vector similar to the one described previously [14]. Site-directed mutagenesis was performed to
463 generate mutant constructs with custom-designed primers. All constructs were verified using DNA
464 sequencing.

465

466 *RaPID screening*

For the first round of RAPID selection, an mRNA library was generated by T7 polymerase mediated *in vitro* transcription of a PCR assembled DNA template, purified by PAGE, and covalently ligated to a puromycin linked oligonucleotide with T4 RNA ligase. 1.2 μM puro-linked mRNA library was translated in a 150 μL *in vitro* translation reaction (genetically reprogrammed to incorporate L- or D- ClAC-Tyr in place of the initiator formyl-methionine) at 37°C for 30 min. Peptide-mRNA fusion molecules were released from the ribosome by treatment with 17 mM EDTA for 30 min. at 37°C, reverse transcribed using MMLV reverse transcriptase (H-)(Promega) at 42°C for 1 hour and buffer exchanged to TBS-T using sephadex G-25. The resulting cyclic peptide-mRNA:cDNA library was counter-selected 3 times against His Pull-Down Dynabeads (Thermo Fisher), and affinity selected against 200 nM bead-immobilised Retromer for 30 min. at 4°C, with the beads washed 3 times with TBS-T, overlaid with 0.1% triton-X100 and heated to 95°C to elute the cDNA for recovery by PCR.

For the second and subsequent rounds of selection, the translation reaction was scaled down to 2.5 μL total volume, and 6 iterative counter-selections using uncoated beads were conducted prior to affinity selection against Retromer. Following 5 iterative rounds of selection, Retromer ligands were identified by sequencing the final enriched cDNA using a MiSeq sequencer (Illumina).

Synthesis of Cyclic Peptides

Untagged peptides were synthesized at 25 μM scale on NovaPEG Rink Amide resin (0.53 mmol/g) using Fmoc-based chemistry on a Syro I peptide synthesizer (Biotage). Fmoc-protected amino acid (6 eq.), (2-(1H-benzotriazol-1-yl)-1,1,3,3-tetramethyluronium hexafluorophosphate (HBTU, 6 eq.), hydroxybenzotriazole (HOBt, 6 eq.) and disopropylethylamine (DIPEA, 12 eq.) with 30 min coupling cycles. Deprotection of fmoc was achieved with 40% piperidine/DMF for 1 × 3 min. then 1 x 12 min. Chloroacetic acid was coupled manually after the final deprotection using the same conditions.

Linear peptides were cleaved from resin with TFA/TIS/H_2O/EDT (92.5:2.5:2.5:2.5) over 2 h. Crude peptides were precipitated and washed (5x cold Et_2O), redissolved in DMSO, and cyclized by adding DIPEA until basic followed by incubating at room temperature. Cyclic peptides were acidified, diluted to 50% DMSO with water and purified by RP-HPLC using a Chromolith C18 column with a gradient of 10 to 70% buffer B (99.9% CH_3CN/0.1% TFA in buffer A, 0.1% TFA in water) over 40 min and lyophilized, before the TFA salt was exchanged to HCl by triplicate lyophilization from 5 mM HCl aq.

Synthesis of biotinylated and FITC labelled cyclic peptides

Biotin and FITC labelled peptides were synthesized (100 μM scale) on Rink Amide MBHA resin (0.6 mmol/g) using Fmoc-based chemistry and a peptide synthesizer (Symphony, Protein Technologies) Fmoc -Lys(Mtt)-OH in position 1. Fmoc-protected amino acid (4 eq.), 2-(6-chloro-1H-benzotriazole-1-yl)-1,1,3,3 tetramethylaminium hexafluorophosphate (HCTU, 4 eq.), and disopropylethylamine (DIPEA, 4 eq.) were used in 2 × 30 min coupling cycles. Fmoc deprotection was achieved by treatment with 1:2 piperidine/DMF for 2

× 3 min. Chloroacetic acid was coupled manually after the final deprotection using chloroacetic acid (4 eq.) and HATU (4 eq.), and DIPEA (4 eq.) in N,N-dimethylformamide (DMF). Selective side-chain deprotection of the methyl trityl (Mtt) group on lysine was achieved using 3% TFA in dichloromethane (DCM) (5 × 2 min). Biotin was coupled using biotin 2-(1H-7-azabenzotriazol-1-yl)-1,1,3,3-tetramethyl uraniumhexafluorophosphate methanaminium (HATU, 2 eq.) and DIPEA in DMF. FITC was coupled using FITC (2 eq.) and DIPEA.

Linear peptides were cleaved from the resin by treatment with TFA/TIS/H_2O (95:2.5:2.5) for 2 h. The crude peptides were precipitated and washed with cold Et_2O, redissolved in 50% acetonitrile/0.05% TFA in water, and lyophilized. Peptides were purified by RP-HPLC using a Phenomenex Luna C18 column eluting at a flow rate of 20 mL/min and a gradient of 20 to 70% buffer B (90% CH_3CN/10% H_2O/0.1% TFA in buffer A, 0.1% TFA in water) over 30 min and lyophilized.

Cyclization to form the thioether was achieved by dissolving the linear peptide in DMF with DIPEA (10 eq.) and the reaction monitored by UP-LCMS. After no more linear peptide was detected, DMF was removed *in vacuo* and the cyclic peptide purified by RP-HPLC using a Phenomenex Luna C18 column eluting at a flow rate of 20 mL/min and a gradient of 20 to 70% buffer B (90% CH_3CN/10% H_2O/0.1% TFA in buffer A, 0.1% TFA in water) over 30 min and lyophilized.

Peptides were characterised and purity determined by analytical RP-UPLC and UPLC-MS methods. UPLC was performed on Shimadzu Nexre UPLC with PDA using an AgilentEclipse plus C18RRHD 1.8 µm, 2.1´100 mm UPLC Column., and a gradient of 0 to 80% buffer B (90% CH_3CN/10% H_2O/0.1% TFA in buffer A, 0.1% TFA in water) over 6 min. UPLC-MS was performed on Shimadzu Nexre UPLC system connected to LCMS-2020 single quadrupole mass spectrometer using an phenomonex Aeris Peptide 1.7 µm XB-C18 column 50 x 2.1 mm and a gradient of 0 to 80% buffer B (90% CH_3CN/10% H_2O/0.1% formic acid in buffer A, 0.1% formic acid in water) over 6 min.

Cell culture and transfection

HeLa cells (ATCC CCL-2) were maintained in high glucose Dulbecco's Modified Eagle Medium (DMEM; Thermo Fisher Scientific) supplemented with 10% fetal bovine serum (FBS) and 2 mM L-glutamine (Thermo Fisher Scientific) in a humidified 37 °C incubator with 5% CO_2. Transfection was performed using Lipofectamine 2000 (Thermo Fisher Scientific) according to the manufacturer's instructions.

Reversible permeabilization and peptide delivery

Reversible permeabilization of HeLa cells with Streptolysin O (SLO; 25,000 - 50,000 U; Sigma-Aldrich) was performed as previously described [125]. In brief, an aliquot of SLO stock was reduced by 10 mM DTT (Sigma Aldrich) for 20 min at 37°C, then diluted to working concentration (200x) in DPBS containing 1 mM $MgCl_2$. HeLa cells grown on coverslips were incubated in the SLO containing solution for 9 min at 37°C, washed

538 twice with DPBS containing 1 mM $MgCl_2$, then incubated with ice-cold transport buffer (140 mM NaCl, 5
539 mM KCl, 1 mM $MgCl_2$, 10 mM HEPES, 10 mM glucose, pH 7.4) containing fluorescent peptides (5 µg/ml)
540 on ice for 5 min. After labeling, the cells were washed with ice-cold transport buffer twice and incubated with
541 the recovery medium (DMEM, 10% FBS, 1.8 mM $CaCl_2$, without antibiotics) for 20 min at 37 °C. Cells were
542 fixed with 4% PFA or ice-cold methanol and subjected for microscopy analysis.

543

544 *Indirect immunofluorescence and image analysis*

545 HeLa cells grown on coverslips were routinely fixed and permeabilized in ice-cold methanol for 5 min at
546 −20°C, unless otherwise cited. After blocked with 2% BSA in PBS for 30 min, cells were labeled with anti-
547 TBC1D5 (1:200) and anti-SNX1 (1:100) for 1 hr at room temperature followed by the incubation with Alexa
548 Fluor 555 and 647 conjugated secondary antibodies. Coverslips were mounted on glass microscope slides
549 using Fluorescent Mounting Medium (Dako), and the images were taken at room temperature using the Leica
550 DMi8 SP8 inverted confocal equipped with 63x Plan Apochromatic objectives or the Zeiss LSM880 Axiovert
551 200 inverted confocal with AiryScan FAST detector equipped with 63x Plan Apochromatic objectives. For
552 quantification, images were taken from multiple random positions for each sample.

553 Images were processed using ImageJ software. Colocalization analysis was performed as described
554 previously [12]. In brief, single cells were segregated from fields of view by generating regions of interest,
555 cropped, split into separated channels, and applied for threshold processing. Colocalization analysis was
556 conducted on three independent experiments and represented as Pearson's correlation coefficient.
557 Colocalization values were exported to R studio and tabulated accordingly.

558

559 *Recombinant Protein Expression and Purification*

560 All the Retromer constructs were expressed using BL21 Star^{TM} (DE3) cells and induced by the addition of
561 IPTG to a final concentration of 1 mM at an OD_{600} of ~ 0.8. The temperature was then reduced to 18°C and
562 incubated overnight. To obtain the Retromer trimer complex (including human, zebrafish and *Chaetomium*
563 *thermophilum*), full-length GST-tagged Vps29 co-expressed with Vps35 was mixed with cell pellet of Vps26A
564 and lysed through a Constant System TS-Series cell disruptor in lysis buffer containing 50 mM HEPES pH
565 7.5, 200 mM NaCl, 5% glycerol, 50 µg/ml benzamidine and DNase I. The homogenate was cleared by
566 centrifugation and loaded onto Talon® resin (Clonetech) for purification. To obtain the correct stoichiometry
567 ratio of the Retromer complex, the purified elution from Talon® resin was further passed through the
568 glutathione sepharose (GE healthcare). Removal of the GST-tag from human and zebrafish Vps29 was
569 performed using on-column cleavage with thrombin (Sigma-Aldrich) overnight at 4°C. For *Chaetomium*
570 *thermophilum* Vps29, the GST-tag was cleaved using PreScission protease overnight at 4°C. The flow-through
571 containing Retromer complex with GST-tag removed was further purified using size-exclusion
572 chromatography (SEC) on a Superdex200 column equilibrated with a buffer containing 50 mM HEPES pH

573 7.5, 200 mM NaCl, 5% glycerol and 0.5 mM TCEP. Production of Retromer individual subunits (Vps29,
574 Vps26A and Vps35) and subcomplexes (Vps29 - Vps35, Vps26A - $Vps35_{1-172}$, Vps26A - $Vps35_{1-224}$, Vps26A
575 - $Vps35_{1-390}$, $Vps26A_{\Delta C\text{-term. tail}}$ - $Vps35_{1-390}$, $Vps26A_{pm}$ - $Vps35_{1-390}$, $Vps26A_{QRFE\text{-}AAAA}$ - $Vps35_{1-390}$, Vps26B -
576 $Vps35_{1-390}$, $Vps26B_{\Delta C\text{-term. tail}}$ - $Vps35_{1-390}$, and $Vps26B_{pm}$ - $Vps35_{1-390}$) were expressed and purified under the
577 same method. In brief, glutathione sepharose was used for Vps29, Vps35 and subcomplexes purification, and
578 Talon® resin was applied for Vps26A.

579 Expression and purification of GST-tagged SNX3, GST-tagged $Fam21_{R19\text{-}R21}$, $TBC1D5_{TBC}$, $SNX27_{PDZ}$
580 and His-tagged SNX27 were performed using similar methods described previously [14, 95, 98, 124]. Cell pellets
581 were lysed by Constant System TS-Series cell disruptor using the same buffer as Retromer. All proteins were
582 passed through either Talon® resin or Glutathione sepharose depending on the affinity tag. Removal of fusion
583 tag was performed on-column overnight using either thrombin for SNX3, and TEV protease for $SNX27_{PDZ}$
584 and $TBC1D5_{TBC}$. The flow-through containing GST-tag removed SNX3, TBC1D5 and $SNX27_{PDZ}$ were further
585 purified using SEC in the same way as Retromer. For, His-tagged SNX27, the fractions eluted from Talon®
586 resin was further purified SEC directly using the same buffer as described above. Similarly, the GST-tagged
587 $Fam21_{R19\text{-}R21}$ eluted from Glutathione sepharose was directly injected into SEC for final purification.

588 Retromer 3KE construct design, expression, and purification has previously been described [100].
589 Briefly, Retromer plasmids were co-transformed into BL21(DE3) Rosetta2 pLysS cells (Millipore). Cells were
590 grown to OD_{600} between 0.8-1.0 and induced for 16-20 hours at 20°C with 0.4 mM IPTG. Cells were lysed by
591 a disruptor (Constant Systems Limited). Protein was purified in 10 mM Tris-HCl (pH 8.0), 200 mM NaCl, 2
592 mM βME using glutathione sepharose (GE Healthcare). Protein was cleaved overnight using thrombin
593 (Recothrom, The Medicines Company) at room temperature and batch eluted in buffer. Retromer was further
594 purified by gel filtration on a Superdex S200 10/300 column (GE Healthcare) into 10 mM Tris-HCl (pH 8.0),
595 200 mM NaCl.

596

597 *Biotinylated Cyclic Peptides Pull-down Assay*

598 Culture dishes (15 cm) with HeLa cells at approximately 90% confluency were washed with PBS and lyzed
599 by the lysis buffer containing 50 mM HEPES pH 7.5, 200 mM NaCl, 1% Triton, 25 µg/ml DNase I and one
600 protease-inhibitor cocktail tablet per 50 ml lysis buffer. Soluble and insoluble fractions were separated by
601 centrifugation at 13,000 *g* for 20 min at 4°C. After centrifugation, supernatant was then added to the
602 streptavidin agarose (Thermo Scientific) pre-incubated with 140 µM of either biotinylated RT-D3 or
603 biotinylated RT-L4 cyclic peptides for 2 h at 4°C. Both cyclic peptides were carefully prepared without
604 forming precipitation before mixing with streptavidin agarose.

605 In the case of capturing SNX3, roughly 5 µM of $DMT1\text{-}II_{550\text{-}568}$ peptide was added to the supernatant
606 prior mixing with the streptavidin agarose. Beads were then spun down at 2,000 g for 2 min and washed five
607 times with washing buffer containing 50 mM HEPES pH 7.5, 200 mM NaCl, 5% glycerol, 0.05% triton X-

100 and 0.5 mM TCEP. Bound complex was eluted from the streptavidin agarose by boiling in 100 mM DTT added SDS loading buffer (Life Science) and subjected to SDS-PAGE analysis and western blotting.

RT-L4 Binding Site Screening Assay

Mapping the potential binding region of RT-L4 was carried out using purified Vps26A, $Vps35_{1-390}$, Vps26-$Vps35_{1-390}$ subcomplex and the associated mutants. First, 10 µM of purified proteins were incubated with fresh streptavidin agarose containing either 100 µM of RT-L4 or equivalent percentage (v/v) of DMSO. The mixture was incubated in binding buffer containing 50 mM HEPES pH 7.5, 200 mM NaCl, 5% glycerol, 0.5 mM TCEP for 30 min at 4°C. Beads were then washed three times with binding buffers followed by SDS-PAGE analysis.

GST Pull-down Assay

GST pull-down assay was carried out using either GST-tagged Retromer, GST-$Fam21_{R19-R21}$, or GST-$TBC1D5_{TBC}$ as bait protein. For pull-down assays containing either SNX27 or SNX3 + DMT1-$II_{550-568}$ peptide, GST-tagged Retromer and GST alone were first incubated with fresh glutathione sepharose bead for 2 hours at 4°C. To avoid precipitation caused by cyclic peptides, SNX3/SNX27 - cyclic peptides mixture were centrifuged at 17,000 rpm for 20 min at 4°C before added into the glutathione sepharose bead samples. The reaction mixtures were incubated for at least 4 hours in binding buffer containing 50 mM HEPES pH 7.5, 200 mM NaCl, 5% glycerol, 0.1% triton X-100 and 0.5 mM TCEP. Beads were then washed four times with binding buffers and samples of beads were analyzed by SDS-PAGE. Retromer - TBC1D5 and Retromer – Fam21 pull-down assay were performed using identical protocol as described above. For Retromer - TBC1D5 pull-down assay, GST-$TBC1D5_{TBC}$ was used in order to differentiate GST-Vps29 and $TBC1D5_{TBC}$ on the SDS-PAGE.

Crystallization and Data Collection

Crystallization screening was performed using hanging drop vapour diffusion method under 96-well format at 20°C. To co-crystallize Vps29 with cyclic peptides, a 1.5-fold molar excess of the RT-D1, RT-D2, RT-D3, RT-L1 and RT-L2 peptides were added separately to the purified hVps29 to a final concentration of 14 mg/ml. Initial crystals were obtained in hVps29 - RT-D1, hVps29 - RT-D2 and hVps29 - RT-L2 complex samples. For hVps29 - RT-D1, plate shape crystals were observed in many different commercial screen conditions, but the best quality crystals were obtained in a condition comprising 3.5 M sodium formate. For hVps29 – RT-D2, the optimized crystals were obtained by streak-seeding crystals grown in 0.1 M potassium thiocyanate, 30% PEG 2000 MME into the same condition prepared with protein at 8 mg/ml. For hVps29 – RT-L2 sample, precipitation was observed after the addition of the cyclic peptide. Precipitation was removed by centrifugation and diamond shape crystals were obtained after overnight incubation in condition consisted of 0.1 M HEPES pH 7.0, 1 M succinic and 1% PEG2000 MME. Initial attempts to co-crystallize hVps29 – RT-D3 and hVps29 – RT-L1 were unsuccessful. For hVps29 – RT-L1, small long needle shape crystals were observed in condition consisted of 1.4 M sodium malonate pH 6.0 using 26 mg/ml protein with 1.5 fold molar excess of RT-L1 and

645 10 fold molar excess of 18-crown-6. Diffraction quality crystals were obtained by streak-seeding crystals
646 grown in the 26 mg/ml into the same condition prepared with protein at 15.5 mg/ml. To grow crystals
647 containing RT-D3, we substituted hVps29 to ctVps29, and managed to obtain diffraction quality crystals in
648 condition consisted of 0.18 M ammonium citrate dibasic and 20% PEG 3350 using 14 mg/ml protein with 2-
649 fold molar excess RT-D3. Prior to data collection, all the crystals were soaked in the appropriate cryoprotectant
650 solutions. X-ray diffraction data were measured on the MX1 and MX2 beamlines at the Australian Synchrotron
651 at 100 K.
652
653 *Crystal Structure Determination*
654 All the data collected were indexed and integrated by AutoXDS [126] and scaled using Aimless [127]. Crystal
655 structures of hVps29 - RT-D1, hVps29 - RT-D2, ctVps29 - RT-D3, hVps29 - RT-L1 and hVps29 - RT-L2
656 were solved by molecular replacement using Phaser [128] with native hVps29 crystal structure (PDB ID: 1W24)
657 as the initial model. The initial electron density map obtained from the best solution guided the locations of
658 the cyclic peptides and 18-crown-6. Structure refinement was performed using the PHENIX suite [129] with
659 iterative rebuilding of the model. The refined model was manually rebuilded using Coot guided by F_o - F_c
660 difference maps. Coordinates for D-tyrosine and sulfanylacetic acid linking N-terminal and C-terminal of the
661 peptides were generated using LIBCHECK from Coot. The quality and geometry of the refined structures were
662 evaluated using MolProbity [130]. Data collection and refinement statistics are summarized in **Table S3**.
663 Sequence conservation was based on a *T-Coffee* multiple sequence alignment [131] and calculated using the
664 ConSurf Server [132]. Structure comparison was analysed using DALI [133] and molecular figures were generated
665 using PyMOL.
666
667 *Surface Plasmon Resonance*
668 SPR experiments were conducted at room temperature using a Biacore T-200 instrument (Cytiva) in HBS-P+
669 buffer (10 mM HEPES, 150 mM NaCl, 0.05 % (v/v) surfactant P20, pH 7.4) containing 0.1% (v/v) DMSO.
670 100 nM human or zebrafish Retromer was immobilized on a Ni^{2+}-primed Series S Sensor Chip NTA (Cytiva)
671 following the manufacturer's instructions. A single cycle kinetics protocol involving five 120 s injections of
672 peptide as analyte at a flow rate 60 $\mu L.min^{-1}$ was employed, with kinetics determined using a 1:1 binding
673 model.
674
675 *Isothermal Titration Calorimetry*
676 ITC experiments were conducted at 25°C using a Microcal ITC200 (Malvern) in buffer containing 50 mM
677 HEPES pH 7.4, 200 mM NaCl, 5% glycerol, 0.5 mM TCEP. Cyclic peptides in the range of 120 μM to 300
678 μM were titrated into 6 – 20 μM of Retromer, subcomplexes or individual subunits. The interaction of
679 Retromer and $TBC1D5_{TBC}$ in the presence of cyclic peptide was carried out by titrating 80 μM of $TBC1D5_{TBC}$
680 into 6 μM of Retromer + 30 μM of either RT-D3 or RT-L4. In the native control, the cyclic peptide was
681 substituted with equivalent percentage (v/v) of DMSO. Similarly, the effect of the cyclic peptides on the

682 interaction of Retromer and $SNX27_{PDZ}$ was performed by titrating 1.3 mM of $SNX27_{PDZ}$ into 30 μM of
683 Retromer + 150 μM of either RT-D3 or RT-L4. The interaction of Retromer and Fam21 was performed by
684 titrating 300 μM of GST-$Fam21_{R19-R21}$ into 12 μM of Retromer + 60 μM of either RT-D3 or RT-L4. In the case
685 of SNX3, 1.2 mM SNX3 was titrated into 12 μM of Retromer + 180 μM DMT1-$II_{550-568}$ peptide + 60 μM of
686 either RT-D3 or RT-L4. Similarly, 1.2 mM SNX3 was titrated into 12 μM of Retromer + 180 μM $CIMPR_{2347-}$
687 $_{2376}$ peptide to examine its effect on Retromer and SNX3 interaction. To ensure that RT-L4 binds specifically
688 only to Retromer but not the accessory proteins, 90 μM of RT-L4 was titrated into 7 μM Retromer,
689 $TBC1D5_{TBC}$, SNX3 or SNX27 using buffer described above. The effect of Vps26 C-terminal disordered tail
690 on RT-L4 and SNX3 binding was first performed by titrating 90 μM of RT-L4 into 8 μM of Vps26A/B -
691 $Vps35_{1-390}$, or $Vps26A/B_{\Delta C\text{-term. tail}}$ - $Vps35_{1-390}$ subcomplexes. In the case of SNX3 binding, 970 μM of SNX3
692 was titrated into 17 μM of FL, pm mutant, QRFE-AAAA or ΔC Vps26A/B - $Vps35_{1-390}$ subcomplexes with
693 and without 255 μM DMT1-$II_{550-568}$ peptide. For the Retromer and R55 interaction, 120 μM - 640 μM of R55
694 was titrated into 9 μM – 16 μM of Retromer using the same buffer as the cyclic peptide ITC experiments.
695 In all cases, the experiments were performed with an initial 0.4 μl (not used in data processing)
696 followed by 12 serial injections of 3.22 μl each with 180 sec intervals. Data were analyzed with Malvern
697 software package by fitting and normalized data to a single-site binding model, yielding the thermodynamic
698 parameters K_d, ΔH, ΔG and $-T\Delta S$ for all binding experiments. The stoichiometry was refined initially, and if
699 the value was close to 1, then N was set to exactly 1.0 for calculation. All experiments were performed at least
700 in triplicate to check for reproducibility of the data.
701
702 *Differential Scanning Fluorimetry*
703 Thermal unfolding experiments were carried out through preferential binding of a fluorophore to unfolded
704 protein using a ViiA7 real-time PCR instrument (Applied Biosystems). In brief, 0.4 mg/ml of fresh Retromer,
705 subcomplex and individual subunits was pre-incubated with 30 - 60 molar excess of cyclic peptides for at least
706 30 min on ice followed by centrifugation at 17,000 rpm for 20 min at 4°C to remove all possible precipitation.
707 To measure thermal denaturation, freshly prepared SYPRO orange dye (Life Science) was then added to
708 protein-cyclic peptide complex mixture to a final concentration of 5X before loaded into the 96-well plate.
709 Relative fluorescence units (R.F.U.) were measured from 25°C to 90°C using the ROX dye calibration setting
710 at 1°C increments. Experiments were performed with four replicates and T_m was calculated using Boltzmann
711 sigmoidal in Prism version 8.0.1 (GraphPad software).
712
713 *Mass Photometry*
714 Molecular mass measurement of Retromer in the presence of cyclic peptide was performed using Refeyn
715 OneMP mass photometer (Refeyn Ltd). In brief, 10 μl of standard buffer containing 50 mM HEPES pH 7.5,
716 200 mM NaCl was applied. Next, 1 μl of 50 nM Retromer + RT-D3 & RT-L4 cyclic peptide was added to the
717 drop to a final concentration of 5 nM and 10000 frames were recorded. Calibration was performed using three
718 protein standards (i.e. 66, 146 and 480 kDa) (ThermoFisher Scientific).

Cryo-EM Grid Preparation and Data Collection

For cryo-electron microscopy of Retromer+RT-L4, Retromer 3KE at a final concentration of 0.5 mM in 20 mM Tris pH 8.0 / 100 mM NaCl / 2 mM DTT was combined with RT-L4 at a final concentration of 0.1 mM, incubated for 1 hour, and spun briefly in a tabletop centrifuge. 2 µl of the sample was applied to freshly glow discharged Quantifoil 1.2/1.3 300 mesh grids, and the grids were vitrified in liquid ethane using a ThermoFisher Mark IV Vitrobot, using a 3.5 second blot time at 100% humidity and 20°C. 4791 micrographs were collected on a ThermoFisher FEI Titan Krios G3i microscope in the Center for Structural Biology's Cryo-EM Facility at Vanderbilt. The microscope operated at 300 keV and was equipped with a ThermoFisher Falcon3 direct electron detector camera. The nominal magnification used during data collection was 120,000x, and the pixel size was 0.6811 Å/pix. The total electron dose was 50 e^-/A^2, and micrographs were collected at +/-30° tilts. Data collection was accomplished using EPU (ThermoFisher).

For cryo-electron microscopy of *apo* Retromer, 2 µl WT Retromer at a concentration of 0.5 mM in 20 mM Tris pH 8.0 / 100 mM NaCl / 2 mM DTT was applied to freshly glow discharged Quantifoil 1.2/1.3 300 mesh grids, and the grids were vitrified in liquid ethane using a ThermoFisher Mark IV Vitrobot, using a 2s blot time at 100% humidity and 8°C. 891 micrographs were collected on a ThermoFisher FEI Titan Krios microscope at the National Resource for Automated Molecular Microscopy (NRAMM). The microscope operated at 300 keV and was equipped with a Gatan BioQuantum energy filter with a slit width of 20eV and a Gatan K2 Summit direct electron detector camera. The nominal magnification used during data collection was 105,000x, and the pixel size was 1.0691 Å/pix. The total electron dose was 73.92e^-/A^2, and micrographs were collected at +/-15° tilts. Data collection was accomplished using Leginon [134]

Single Particle Cryo-EM Image & Data Processing

All images were motion corrected using MotionCor2 (Zheng et al., 2017). Micrographs from the *apo* Retromer data collection were rescaled to match the 1.096Å/pix pixel size from published data collections [100] using an NRAMM script written for MotionCor2. The CTF of each micrograph was determined using Gctf [135]. Defocus values for the Retromer/RT-L4 data varied between -0.8 and -2.6 µm; defocus values for the *apo* Retromer data varied between -0.8 and -4.7 µm. RELION-3 [136] was used for all image processing unless otherwise indicated.

Retromer/RT-L4 processing. Several thousand particles were manually selected to perform initial 2D classification to produce templates for autopicking. Template-based autopicking identified 1,683,975 particles. Multiple rounds of 2D classification yielded 272,349 particles suitable to continue to 3D classification. Initial models for 3D classification were generated by earlier single particle work with wild-type Retromer in the absence of RT-L4 [100]; models were filtered to 60 Å resolution for use in these experiments. The particles

underwent multiple rounds of CTF refinement and Bayesian polishing to produce a final set of 45,330 particles suitable for 3D refinement and postprocessing. The final masked model had a resolution of 5.0 Å and a Relion-determined B-factor of -189.

Apo Retromer processing. Data giving rise to the published Retromer *apo* reconstruction lacked tilted views (**Table S4**); an additional data set (**Table S4**; data collection #3) was collected to add tilted views and to improve the reconstruction for this study. Several thousand particles were manually selected from dataset #3 (**Table S4**) to perform initial 2D classification and produce templates for autopicking. Template-based autopicking identified 207,026 particles, which were subjected to initial 2D and 3D classification and refinement as well as CTF refinement. 250,500 particles from data collections #1 and #2 (**Table S4**) Retromer datasets[100] were imported to combine with data collection #3. Multiple rounds of 2D classification yielded 72,795 particles suitable to continue to 3D classification. Initial models for 3D classification [100] were filtered to 60 Å resolution for use in these experiments. The particles underwent multiple rounds of CTF refinement and Bayesian polishing to produce a final set of 43,808 particles suitable for 3D refinement and postprocessing. The final masked model had a resolution of 4.9Å and a Relion-determined B-factor of -113.799.

For both reconstructions, rigid-body docking and map visualization were performed in Chimera[137] using the Fit in Map routine. Models for N-VPS35 and VPS26A subunits were obtained from PDB 5F0J.

Liposome preparation

Sucrose-loaded liposome binding assay were performed using the standard extrusion method with some modification [138]. In brief, cargo loaded Folch liposomes were made by mixing 25 µl of 4 mg/ml N-terminal palmitoylated $CIMPR_{2347-2376}$ peptide, 50 µl of 10 mg/ml Folch fraction I (Sigma Aldrich) and 50 µl of 1 mg/ml di-C16 PtdIns(3)*P* (Echelon Biosciences), each freshly prepared in chloroform, to a total volume of 500 µl chloroform. The solution was dried down on the walls of a mini-round bottom flask under a N_2 stream and left overnight in a vacuum desiccator to yield a lipid film. This yields liposomes with a final PtdIns(3)P ratio of 10% (w/v). For PC/PE liposome, 50 µl of 10 mg/ml stock of 1-palmitoyl-2-oleoyl-sn-glycero-3-phosphocholine (POPC) and 1-palmitoyl-2-oleoyl phosphatidylethanolamine (POPE) in a 9:1 ratio (Avanti Polar Lipids) was freshly prepared in a 500 µl volume and lipid films formed using the same method as Folch liposomes. This results in a POPC/POPE liposome in a 90%:10% w/v ratio. To form multilamellar vesicles (MLV), the lipid films were hydrated with a buffer comprising 20 mM HEPES pH 7.5 and 220 mM sucrose with agitation follow by10 cycles of rapid freeze-thaw. The sucrose loaded heavy MLVs were centrifuged at 180,000 x *g* for 30 min at 4°C using Optima TL benchtop Ultracentrifuge (Beckman Coulter). The resulting pellets were buffer exchanged by resuspension into the assay buffer comprising 50 mM HEPES pH 7.5, 125 mM NaCl, 0.5 mM TCEP. To avoid buffer mismatch, the protein samples were also buffer exchanged into the same buffer.

Liposome-Binding Assays

The binding assay was performed in a total volume of 80 µl comprising 40 µl of sucrose-loaded MLVs and 7 µM Retromer, 7 µM SNX3 or 7 µM of Retromer – SNX3 mixture in 1 to 1 ratio. The reaction mixtures were incubated at room temperature for 15 min followed by centrifugation at 36000 x *g* using Optima TL benchtop ultracentrifuge (Beckman Coulter) for 15 min at 4°C. The supernatant and pelleted fractions were then carefully separated. The pellet was then resuspended in 80 µl of buffer containing 50 mM HEPES pH 7.5, 125 mM NaCl, 0.5 mM TCEP before analyzed by SDS-PAGE.

Statistics

Statistical analysis was completed in R studio using dplyr, ggplot2, ggpubr packages. Error bars on graphs were represented as the standard error of the mean (± SEM). P values were calculated using the two-tailed Student's *t*-test. $P < 0.05$ was considered as significant.

Data deposition

Crystal structural data have been deposited at the Protein data bank (PDB) under the accession number 6XS5 (hVPS29 – RT-D1), 6XS7 (hVPS29 – RT-D2), 6XS8 (ctVPS29 – RT-D3), 6XS9 (hVPS29 – RT-L1), and 6XSA (hVPS29 – RT-L2). CryoEM data has been deposited at the Electron Micrscopy Data Bank (EMDB) under accession numbers D_1000253118 and D_1000253090 for the apo and RT-L4-bound Retromer complexes respectively. All the relevant raw data related to this study is available from the corresponding authors on request.

Acknowledgments

We acknowledge the use of the Australian Microscopy and Microanalysis Research Facility at the Center for Microscopy and Microanalysis at The University of Queensland. We also acknowledge use of the University of Queensland Remote Operation Crystallization and X-ray (UQ ROCX) Facility and the assistance of Gordon King and Karl Byriel. X-ray data were collected on the MX1 and MX2 microfocus beamline at the Australian Synchrotron. This work is supported by funds from the Australian Research Council (ARC) (DP160101743; DP180103244, CE140100011), National Health and Medical Research Council (NHMRC) (APP1156493; APP1156732), and Bright Focus Foundation (A2018627S). BMC is supported by an NHMRC Senior Research Fellowship (APP1136021), DPF by an NHMRC Senior Principal Research Fellowship (1117017), and DAS is by an NHMRC Career Development Fellowship (APP1140851). This work was also supported by the Japan Agency for Medical Research and Development (AMED), Platform Project for Supporting Drug Discovery and Life Science Research (JP20am0101090) and the Japan Society for the Promotion of Science (JSPS), Specially Promoted Research (JP20H05618) to H.S. CryoEM data were collected at the Vanderbilt Center for Structural Biology Cryo-Electron Microscopy Facility. We thank Dr. Scott Collier and Dr. Melissa Chambers for data collection support. Some of this work was performed at the National Center for CryoEM Access and Training (NCCAT) and the Simons Electron Microscopy Center located at the New York Structural Biology Center, supported by the NIH Common Fund Transformative High Resolution Cryo-Electron Microscopy program (U24 GM129539), and by grants from the Simons Foundation (SF349247) and NY State Assembly. AKK, BX, and LPJ are supported by NIH R35GM119525. LPJ is a Pew Scholar in the Biomedical Sciences, supported by the Pew Charitable Trusts.

835 **FIGURE LEGENDS**

836

837 **Figure 1. Cyclic peptides reveal strong binding characteristics with Retromer.**

838 (**A**) Schematic diagram showing the RaPID system used to screen for cyclic peptides binding to Retromer. (**B**)
839 Eight Retromer-binding macrocyclic peptides were identified with either N-chloroacetyl-$_D$-tyrosine or N-
840 chloroacetyl-$_L$-tyrosine as initiating residues. (**C**) Binding of RT-D1, RT-D2, RT-D3, RT-L1, RT-L2, and RT-
841 L4 with Retromer (blue), Vps29 (light green), Vps26A (orange), Vps29 – Vps35 (red) and Vps26A – Vps35$_{1-}$
842 $_{390}$ (dark green) by ITC. SPR binding curves for each peptide are shown in **Fig. S3**. (**D**) ITC thermogram
843 showing that addition of α-helix 8 and 9 of Vps35 (residues 173 to 224) contributes to RT-L4 binding affinity
844 but is not essential for interaction. All ITC graphs represent the integrated and normalized data fit with 1 to 1
845 ratio binding. The binding affinity (K_d) is given as mean of at least three independent experiments (**Table S2**).
846 (**E**) Relative binding position of each cyclic peptide to Retromer based on the ITC measurements indicated on
847 the structure of the mouse Retromer complex (PDB ID 6VAC) [100].

848

849 **Figure 2. Crystal structures of Vps29 in complex with cyclic peptides.**

850 (**A**) Superimposition of the crystal structures of Vps29 in complex with five macrocyclic peptides. (**B**)
851 Sequence conservation mapped onto the hVPS29 structure surface highlights the conserved binding site for
852 each of the cyclic peptides, with RT-D1 shown as an example. (**C**) Superimposition of the Vps29 – RT-D1
853 peptide complex with the Vps29 - Vps35$_{483-780}$ crystal structure (PDB ID: 2R17) [96]. The cyclic peptides bind
854 opposite to the Vps35 interface. (D) Details of macrocyclic peptides in stick representation bound to Vps29.
855 Schematic diagrams indicate the number of intermolecular contacts (salt bridge, hydrogen bonds and
856 hydrophobic interactions) of each residue on the peptide with Vps29. The residues on the peptide with 0, 1, 2
857 and ≥3 contacts are shown in grey, light green, green and dark green boxes respectively. Each peptide utilises
858 a core Pro-Leu sequence forming a β-hairpin, labelled as position 0 and 1 for reference. Electron density for
859 each peptide is shown in **Fig. S3**. (E) Close-up of the β-hairpin conformation of the bound RT-D1 peptide. (**F**)
860 TBC1D5 (PDB ID 5GTU) [95], VARP (PDB ID 6TL0) [103] and RIDL (PDB ID 5OSH) [76] bind to the same site
861 of Vps29 using a similar β-hairpin comprised of a Pro-Leu dipeptide sequence. For clarity, only the key
862 residues involve in the contact are shown. (**G**) ITC thermogram for the titration of RT-D1 (purple) and RT-D1
863 L7E (blue) with Retromer showing the importance of Pro-Leu motif in the interaction. The graph represents
864 the integrated and normalized data fit with a 1 to 1 binding ratio.

865

866 **Figure 3. The RT-L4 macrocylic peptide is a molecular chaperone that binds Retromer at the Vps35-**
867 **Vps26 interface.**

868 (**A**) Bar graph summarizing the measured thermal unfolding temperatures (T_m) of Retromer in the presence of
869 cyclic peptides. Raw data is shown in **Fig. S4**. (**B**) Pull-down assay showing the interaction of biotinylated
870 RT-L4 bound to streptavidin-coated agarose beads with either wild-type Vps26A-Vps35$_{1-390}$ subcomplex or

871 indicated point mutants. Individual Vps26A and $Vps35_{1-390}$ proteins do not bind the peptide, while the D128R
872 mutation in $Vps35_{1-390}$ specifically blocks sub-complex interaction. (**C**) Sequence conservation map of
873 Vps26A-$Vps35_{12-470}$ subcomplex (PDB ID 5F0L) highlighting the proposed RT-L4 binding site, and its
874 relationship to known binding sites for SNX3 [98] and SNX27 [105]. (**D**) CryoEM reconstruction of the human
875 Retromer (apo form) and (**E**) in complex with RT-L4. CryoEM density shown as transparent molecular
876 envelope, with crystal structures of Retromer subcomplexes (PDB ID 2R17 and 5F0L) overlapped to the map
877 (contoured at 4.7σ). The additional density seen on addition of the cyclic peptide added Retromer supports the
878 mutagenesis data indicating RT-L4 binds at the Vps26 and Vps35 interface. (**F**) Enlarged view of the Vps26
879 and Vps35 interface highlighting the additional density in the CryoEM map of RT-L4 added Retromer but not
880 in the apo form. For clarity, D128 of Vps35 is highlighted in red.
881
882 **Figure 4. The effect of cyclic peptides on the interaction of Retromer with known regulatory and adaptor**
883 **proteins.**
884 (**A**) Interactions of Retromer with TBC1D5, SNX3, SNX27 and Fam21 in the presence of either RT-D3 or
885 RT-L4. GST-$TBC1D5_{TBC}$ and GST-$Fam21_{R19-R21}$ were used as baits for Retromer, while GST-tagged Retromer
886 (Vps29 subunit) was used as bait for SNX3 and SNX27. (**B**) ITC measurement of $TBC1D5_{TBC}$, (**C**) SNX3
887 (with DMT1-$II_{550-568}$ present), (**D**) SNX27, and (**E**) GST-$Fam21_{R19-R21}$ with Retromer in the presence or
888 absence of RT-D3 or RT-L4. (**F**) Hela cell lysates were incubated with streptavidin agarose coated with
889 biotinylated RT-D3 or RT-L4 and bound proteins subjected to SDS-PAGE and western blotting with
890 antibodies against indicated proteins. (**G**) ITC measurement of $PTHR_{586-593}$ cargo peptide [14] with $SNX27_{PDZ}$
891 alone (yellow), Retromer + RT-L4 (red), Retromer + $SNX27_{PDZ}$ (green) and Retromer + $SNX27_{PDZ}$ + RT-L4
892 (blue). RT-L4 allosterically enhances the affinity of Retromer + $SNX27_{PDZ}$ for cargo. The cargo peptide binds
893 to SNX27 All ITC graphs represent the integrated and normalized data fit with a 1 to 1 binding ratio. The
894 binding affinity (K_d) is given as mean of at least two independent experiments. (**H**) Liposome-binding assay
895 of Retromer with membrane-associated SNX3 cargo complex in the presence of cyclic peptides. Multilamellar
896 vesicles were composed of either control PC/PE lipids, or Folch I lipids containing added PtdIns(3)*P* and N-
897 terminal palmitoylated $CIMPR_{2347-2376}$ peptide (schematic diagram on top). "S" and "P" indicates unbound
898 supernatant and bound pellet respectively. Control experiments are shown in **Fig. S7B** and **S7C**. (**I**) Schematic
899 summarizing the effects of RT-D3 and RT-L4 on Retromer engagement with known regulatory and adaptor
900 proteins.
901
902 **Figure 5. An autoinhibitory role for the disordered C-terminal tail of Vps26 in binding RT-L4 and**
903 **SNX3**.
904 (**A**) ITC thermogram for the titration of RT-L4 with $Vps35_{1-390}$ sub-complex with either full-length or C-
905 terminal truncated Vps26A and Vps26B paralogues. (**B**) Sequence alignment of the C-terminal region of
906 Vps26 highlighting the low-sequence similarity of the unstructured C-terminal tail. Sites of phosphorylation
907 are indicated in blue (www.phosphosite.org) [107]. Hs, *Homo sapiens*; Dr, *Danio rerio*; Ct, *Chaetomium*

908 *thermophilum*; Pf, *Plasmodium falciparum*, Sc, *Saccharomyces cerevisiae.* (**C**) ITC measurement of SNX3
909 binding to native, phosphomimetic (pm), and C-terminal tail truncated (ΔC) versions of Vps26A/B – $Vps35_{1-}$
910 $_{390}$ subcomplexes. In each case, the presence of DMT1-II cargo peptide was required to detect SNX3 binding.
911 (**D**) ITC measurement of SNX3 binding to QRFE-AAAA mutant Vps26A – $Vps35_{1-390}$. ITC thermograms in
912 (**A**), (**C**) and (**D**) represent the integrated and normalized data fit with a 1 to 1 binding ratio. (**E**) Summary of
913 binding affinities of SNX3 for each Vps26A/B – $Vps35_{1-390}$ subcomplex in the presence of DMT1-$II_{550-568}$
914 cargo peptide. For clarity, the association constant (K_d^{-1}) is shown. The binding affinity is given as mean of at
915 least two independent experiments. (**F**) A proposed model for the autoinhibitory role of the Vps26 disordered
916 C-terminal tails. Our data suggests that these tails can self-associate and reduce affinity for SNX3-cargo
917 complexes, while removal of these tails or their release upon phosphorylation enhances SNX3-cargo
918 association. The C-terminal sequence of Vps26B has greater autoinhibitory activity than Vps26A.
919
920 **Figure 6. Macrocyclic peptides can be used to study Retromer localization in cells.**
921 (**A**) Specific targeting of endosomal structures by streptolysin O (SLO) delivered cyclic peptides. HeLa cells
922 transiently expressing SNX1-mCherry were exposed to SLO at 37°C for 9 min before incubating with the
923 cyclic peptide RT-D3-FITC or RT-L4-FITC on ice for 5 min. Permeabilized cells were recovered in the
924 recovery medium containing Hoechst 33342 for 20 min, then fixed in 4% PFA. The negative control (-SLO)
925 shows no labeling of intracellular structures. Scale bar, 10 µm. Graphs show the fluorescence intensity of RT-
926 D3-FITC or RT-L4-FITC in HeLa cells (means ± SEM). Two-tailed Student's *t-test* was used to determine the
927 statistical significance (n=3). **, $P < 0.01$. (**B**) HeLa cells transiently expressing Vps35-mCherry were labeled
928 by SLO-delivered cyclic peptide RT-D3-FITC or RT-L4-FITC, fixed in 4% PFA, and imaged by Airyscan
929 super-resolution microscopy. Scale bar, 5 µm. (**C**) HeLa cells treated with SLO-delivered RT-D3-FITC, RT-
930 L4-FITC, or DMF control were incubated in recovery medium for 2 h, fixed in ice-cold methanol, and co-
931 immunolabeled with antibodies against endogenous TBC1D5 and SNX1, followed by Alexa Fluor-conjugated
932 fluorescent secondary antibodies. Scale bar, 10 µm. The colocalization between TBC1D5 and SNX1 was
933 quantified by Pearson's correlation coefficient and represented in the graph (means ± SEM). Two-tailed
934 Student's *t-test* was utilized to determine the statistical significance (n=3). ****, $P < 0.0001$; ns, not significant.
935
936

937 **SUPPLEMENTARY INFORMATION.**

938

939 **Figure S1. MALDI-TOF spectra of the Retromer associated cyclic peptides.**

940 The molecular mass of RT-D1, RT-D2, RT-D3, RT-D4, RT-L1, RT-L2, RT-L3 and RT-L4 are shown in the
941 spectrum.

942

943 **Figure S2. Preliminary SPR binding kinetics of Retromer-associated cyclic peptides.**

944 (**A**) Single cycle kinetics experiments were performed using SPR with His-tagged human or zebrafish
945 Retromer with varying concentrations of cyclic peptides. In each case, 2-fold serial dilutions of peptide were
946 tested starting from a highest concentration of 200 or 1000 nM as indicated. (**B**) Binding kinetics of
947 macrocyclic peptides for human and zebrafish Retromer complexes as determined by SPR. (**C**) Gels showing
948 purity of human and zebrafish Retromer complexes used for Rapid peptide screening and SPR experiments.

949

950 **Figure S3. Interaction analysis of Vps29 and cyclic peptides.**

951 (**A**) Structures of the Vps29 bound cyclic peptides, RT-D1, RT-D2, RT-D3, RT-L1 and RT-L2. For clarity,
952 the main chain backbones are shown in ribbon and side chains are shown in stick form. The electron density
953 shown corresponds to a simulated-annealing OMIT Fo - Fc map contoured at 3σ. (**B**) Highlighted details of
954 the residues involved in the interactions between Vps29 and bound macrocyclic peptides. (**C**) ITC thermogram
955 for the titration of RT-D2 (red line) and RT-D3 (blue line) with ctVps29. The graph represents the integrated
956 and normalized data fit with a 1 to 1 binding ratio. The binding affinity (K_d) is given as mean of three
957 independent experiments. (**D**) Surface and (**E**) cartoon representations of the human Vps29 – RT-L1 structure
958 highlighting the secondary binding site located opposite to the primary common binding site. Residues involve
959 in contact with Vps35 are shown in light blue.

960

961 **Figure S4. RT-L4 enhances the thermal stability of Retromer in solution.**

962 (**A**) Temperature dependent unfolding of Vps29 in the presence of 30-fold molar excess of RT-D1, RT-D2,
963 RT-D3, RT-L1 and RT-L2. (**B**) Temperature dependent unfolding of native Retromer in the presence of 30-
964 fold molar excess of RT-D1, RT-D2, RT-D3, RT-L1 and RT-L2 complexes, and (**C**) in the presence of 30-
965 fold molar excess of RT-L4. Melting temperatures (Tm) were assessed by differential scanning fluorimetry.
966 The sigmoidal curve is characteristic of cooperative thermal denaturation of a folded protein. A shift in melting
967 temperature indicates the stabilization of the proteins upon the addition of cyclic peptide. (**D**) Dose-response
968 curve of Retromer in the presence of RT-L4 (red line) or RT-D3 (green line).

969

970 **Figure S5. R55 does not significantly increase the thermal-stability of Retromer.**

971 **(A**) Molecular mass of Retromer in the presence of RT-D3 and RT-L4 monitored by mass photometry. In this
972 experiment, Retromer shows a mass of 151 kDa, corresponding to the heterotrimeric state of Retromer. (**B**)
973 Temperature dependent unfolding of 3 μM Retromer (blue dot) compared with samples containing 60 μM of

R55 (red arrow) or 60 μM RT-L4 (green square). (**C**) Same as (**B**) but with 1 mM of R55 showing two stages of unfolding. Note that preparation of 1 mM RT-L4 in aqueous buffer was not possible due to the lower solubility characteristics. (**D**) ITC thermogram for the titration of R55 with Retromer. The graph represents the integrated and normalized data fit with a 1 to 1 binding ratio. The binding affinity (K_d) is given as mean of three independent experiments.

Figure S6. Binding of RT-L4 to Retromer from different species and assessed by cryoEM.
(**A**) ITC thermograms for the titration of RT-L4 with zebrafish Retromer showing a strong binding similar to human Retromer. (**B**) ITC thermograms for the titration of RT-L4 with *C. thermophilum* Retromer shows a lower affinity compared to zebrafish or human Retromer. The graphs represents the integrated and normalized data fit with a 1 to 1 binding ratio. The binding affinity (K_d) is given as mean of at least three independent experiments. (**C**) CryoEM density map of human Retromer (apo form) and in complex with RT-L4 displayed as mesh surface, with crystal structures of Retromer subcomplexes (PDB ID 2R17 and 5F0L) overlapped to the map. Red arrow indicates the Vps35 model fitting into α helices. Yellow arrow indicates the extra density observed between Vps26 and Vps35 interface in the RT-L4-bound Retromer. (**D**) Three different views of the Retromer CryoEM structure reconstructions highlighting the Vps35 and Vps26 interface. The cryoEM density from apo Retromer (grey mesh) is overlayed with the cryoEM density from RT-L4-bound Retromer (light blue surface). (**E**) Fourier Shell Correlation (FSC) plots highlighting masked and unmasked resolution estimates from RELION are shown for Retromer (apo form) and in complex with RT-L4. The intersections of the curve with FSC=0.143 (grey dotted line) are shown. (**F**) Angular distribution of the particles used for the final round of refinement. The height and colour of the cylinder bars is proportional to the number of particles in those views.

Figure S7. Binding of SNX3 and Retromer in the presence CIMPR$_{2347-2376}$ cargo peptide.
(**A**) ITC measurements of RT-L4 with Retromer, SNX27$_{PDZ}$, TBC1D5$_{TBC}$ and SNX3 demonstrate the binding specificity of the cyclic peptide to Retromer. (**B**) Liposome-binding assay of SNX3 and Retromer using Folch I liposomes containing 10% PtdIns(3)*P* and 10% N-terminal palmitoylated CIMPR$_{2347-2376}$ peptide. (**C**) Liposome-binding assay of Retromer and SNX3 mixture as in (**B**) except Folch I liposomes contain only 10% PtdIns(3)*P* without the CI-MPR cargo. Retromer binds only weakly to Folch liposomes in the absence of either SNX3 or cargo sequence. In all three SDS-PAGE gels, "S" indicates unbound supernatant and "P" indicates bound pellet after ultracentrifugation. (**D**) ITC measurement of SNX3 with Vps26A –Vps35$_{1-390}$ subcomplex in the presence of CIMPR$_{2347-2376}$ cargo peptide. The graph represents the integrated and normalized data fit with a 1 to 1 binding ratio. The binding affinity (K_d) is given as mean of at two three independent experiments. (**E**) Sequence alignment of the C-terminal region of Vps26 and (**F**) the N-terminal region of Vps35 showing the similarity between species. Key residues involve in contacts with Vps35 (yellow arrow) and Vps26 (blue dots) are labelled on top of the sequence. h, *Homo sapiens*; zf, *Danio rerio*; Ct, *Chaetomium thermophilum*; m, *Mus musculus.*

1011

1012 **Figure S8. ctVps26 C-terminal disordered tail reveals similar autoinhibitory characteristics.**

1013 ITC measurement of RT-L4 with native and ctVps26 C-terminal tail truncated ctRetromer. The graph
1014 represents the integrated and normalized data fit with a 1 to 1 ratio binding. The binding affinity (K_d) is given
1015 as mean of at least three independent experiments.

1016

1017 **Figure S9. Unprocessed original scans of western blots for the main figure.**

1018 Unprocessed images of all blots in this study.

1019 **Table S1: List of synthesized cyclic peptides.**

Name	Sequence	Ext. Co.	MW. (Da)	Purity % UPLC
Cyclic peptides from initial screen				
RT-D1	Ac-yIIDTPLGVFLSSLKRC-NH2	1490	1963.9	>95
RT-D2	Ac-yTTIYWTPLGTFPRIRC-NH2	8480	2126.9	>95
RT-D3	Ac-yGYDPLGLKYFAC-NH2	4470	1548.6	>95
RT-D4	Ac-yGWDPLYVNYFVC-NH2	9970	1677.7	>95
RT-L1	Ac-YIKTPLGTFPNRHGC-NH2	1490	1742.9	>95
RT-L2	Ac-YLPTITGVGHLWHPLC-NH2	6990	1845.9	>95
RT-L3	Ac-YLEFDPLYVRLFYVNC-NH2	4470	2093.0	>95
RT-L4	Ac-YWISNSWTTYRYVSTC-NH2	15470	2068.9	>95
Modified cyclic peptides				
RT-D1 L7E	Ac-yIIDTPEGVFLSSLKRC-NH2	1490	1979.86	>95
RT-D3-scramble	Ac-yGLYLKYGFPDAC-NH2	4470	1548.6	>95
Biotinylated RT-D3	Ac-[yGYDPLGLKYFAC]AGAGK(Biotin)-NH2	4470	2195.36	>95
Biotinylated RT-L4	Ac-[YWISNSWTTYRYVSTC]AGAGK(Biotin)-NH2	15470	2715.66	>95
RT-D3-FITC	Ac-[yGYDPLGLKYFAC]AGAGK(FITC)-NH2	4470	2340.43	>95
RT-L4-FITC	Ac-[YWISNSWTTYRYVSTC]AGAGK(FITC)-NH2	15470	2860.73	>95

1020

1021 **Table S2: Thermodynamic parameters for the binding of Retromer with cyclic peptides by ITC.**

	K_d (nM)	ΔH (kcal/mol)	ΔG (kcal/mol)	$-T\Delta S$ (kcal/mol)
Retromer				
RT-D1	130 ± 9	-11.5 ± 0.5	-9.4 ± 0.08	2.1 ± 0.6
RT-D2	53 ± 6	-9.7 ± 1.6	-9.9 ± 0.08	0.5 ± 0.2
RT-D3	25 ± 1	-13.4 ± 1.4	-10.4 ± 0.06	3.9 ± 0.1
RT-L1	96 ± 1	-11.0 ± 0.9	-9.5 ± 0.06	1.4 ± 0.9
RT-L2	852 ± 14	-16.0 ± 0.7	-8.2 ± 0.06	7.7 ± 0.7
RT-L4	273 ± 7	-7.0 ± 0.1	-8.9 ± 0.08	-2.0 ± 0.1
Vps29				
RT-D1	95 ± 1	-14.2 ± 0.3	-9.5 ± 0.06	4.6 ± 0.3
RT-D2	64 ± 1	-11.6 ± 0.1	-9.8 ± 0.08	1.7 ± 0.1
RT-D3	8 ± 2	-17.4 ± 1.4	-11.1 ± 0.21	6.4 ± 1.2
RT-L1	64 ± 5	-13.0 ± 1.1	-9.8 ± 0.08	3.2 ± 1.0
RT-L2	783 ± 7	-9.1 ± 1.6	-8.4 ± 0.06	1.6 ± 0.9
RT-L4		No binding detected		
Vps29-Vps35				
RT-D1	106 ± 4	-10.5 ± 0.4	-9.5 ± 0.09	0.9 ± 0.3
RT-D2	65 ± 5	-11.2 ± 1.0	-9.8 ± 0.07	1.4 ± 0.9
RT-D3	29 ± 2	-11.6 ± 1.3	-10.3 ± 0.08	2.4 ± 1.1
RT-L1	90 ± 3	-7.9 ± 1.2	-9.6 ± 0.07	1.8 ± 1.0
RT-L2	763 ± 12	-8.7 ± 1.7	-8.4 ± 0.08	2.1 ± 1.1
RT-L4		No binding detected		
Vps26-Vps35 truncations				
Vps26A_Vps35$_{1-390}$: RT-L4	165 ± 8	-6.8 ± 1.2	-9.2 ± 0.06	-2.5 ± 1.2
Vps26B_Vps35$_{1-390}$: RT-L4	491 ± 27	-2.7 ± 1.2	-8.6 ± 0.10	-5.4 ± 0.4
Vps26A_Vps35$_{1-224}$: RT-L4	222 ± 4	-7.0 ± 1.7	-9.1 ± 0.11	-2.1 ± 1.7
Vps26A_Vps35$_{1-172}$: RT-L4	339 ± 7	-6.3 ± 2.5	-8.8 ± 0.10	-2.5 ± 2.5
Vps26A$_{9-298}$_Vps35$_{1-390}$: RT-L4 (Δ C-term. tail complex)	33 ± 2	-11.9 ± 1.0	-10.2 ± 0.07	1.7 ± 1.0
Vps26A				
RT-D1, D2, D3, L1, L2, L4		No binding detected		
zfRetromer				
RT-L4	88 ± 11	-6.9 ± 1.8	-9.6 ± 0.08	-2.6 ± 2.0
ctRetromer				

RT-L4	5030 ± 900	-7.4 ± 0.3	-7.3 ± 0.10	-2.7 ± 1.9
ctRetromer ΔC-term. tail				
RT-L4	1770 ± 170	-6.0 ± 0.7	-7.9 ± 0.06	-1.9 ± 0.7
ctVps29				
RT-D2	135 ± 3	-10.5 ± 1.0	-9.3 ± 0.08	1.1 ± 0.9
RT-D3	603 ± 6	-7.4 ± 0.3	-8.5 ± 0.07	-0.9 ± 0.1

1022

1023

1024 **Table S3. Summary of crystallographic structure determination statistics**

Data collection statistics	Vps29 - RT-D1	Vps29 - RT-D2	ctVps29 - RT-D3	Vps29 – RT-L1	Vps29 - RT-L2
PDB ID	6XS5	6XS7	6XS8	6XS9	6XSA
Space group	C121	$P2_12_12$	$P3_121$	$P4_12_12$	$P2_12_12$
Resolution (Å)	42.41 – 2.01 (2.06 – 2.01)	48.00 – 1.58 (1.61 – 1.58)	42.75 – 1.83 (1.87 – 1.83)	49.16 – 2.69 (2.82 – 2.69)	44.10 – 1.83 (1.87 – 1.83)
a, b, c (Å)	114.39, 43.77, 43.14	38.06, 144.01, 43.02	47.52, 47.52, 170.99	119.44, 119.44, 125.63	37.48, 132.30, 39.87
α, β, γ (°)	90.0, 100.5, 90.0	90.0, 90.0, 90.0	90.0, 90.0, 120.0	90.0, 90.0, 90.0	90.0, 90.0, 90.0
Total observations	98,823 (7,278)	440,767 (17,466)	217,001 (12,613)	142,659 (11,469)	125,257 (6,931)
Unique reflections	14,170 (1,030)	33,360 (1,514)	20,529 (1,206)	25,371 (3,013)	18,052 (1,041)
Completeness (%)	99.9 (98.8)	99.6 (92.7)	99.6 (99.0)	97.8 (88.9)	98.6 (93.5)
R_{merge}[+]	0.077 (0.585)	0.062 (0.712)	0.039 (0.146)	0.085 (0.557)	0.080 (0.264)
R_{pim}*	0.032 (0.235)	0.018 (0.213)	0.013 (0.047)	0.053 (0.421)	0.035 (0.110)
CC1/2	0.999 (0.917)	1.000 (0.867)	1.000 (0.995)	0.997 (0.879)	0.996 (0.976)
$\langle I/\sigma(I)\rangle$	12.2 (2.5)	18.9 (2.6)	28.0 (9.5)	8.2 (1.3)	15.5 (6.4)
Multiplicity	6.9 (7.0)	13.0 (11.5)	10.2 (10.5)	5.6 (3.8)	6.3 (6.6)
Molecule/asym	1	1	1	2	1
Refinement statistics					
R_{work}/R_{free} (%) ¶#	19.0/22.5	17.8/19.1	20.5/25.1	24.7/28.8	19.0/22.7
No. protein atoms	1469	1523	1483	2986	1481
Waters	87	179	165	38	191
Ligand (peptide)	143	155	110	492	131
Wilson B ($Å^2$)	26.4	19.2	16.9	68.9	17.1
Average B ($Å^2$)^	32.3	24.2	21.5	111.0	20.6
Protein	32.3	22.5	20.1	108.0	19.6
Cyclic peptide	27.9	27.7	30.9	101.8	21.1
Water	35.9	36.4	26.6	88.5	28.4
rmsd bonds (Å)	0.007	0.011	0.011	0.017	0.007
rmsd angles (°)	1.210	1.101	1.314	1.968	0.968
Ramachandran plot:					
Favored/outliers (%)	96.5/1.0	98.6/0.0	99.0/0.0	95.3/1.4	98.0/0.5

1025 Values in parentheses refer to the highest resolution shell. [+]$R_{merge} = \Sigma|I - \langle I\rangle| / \Sigma\langle I\rangle$, where I is the intensity of each individual reflection. *R_{pim} indicates
1026 all I^+ & I^-. ¶$R_{work} = \Sigma h|F_o - F_c| / \Sigma_i|F_o|$, where F_o *and* F_c are the observed and calculated structure-factor amplitudes for each reflection h. #R_{free} was
1027 calculated with 10% of the diffraction data selected randomly and excluded from refinement. ^Calculated using Baverage.

1028

1029 **Table S4: CryoEM data collection parameters for 3KE Retromer complex in the presence of the RT-**
1030 **L4 cyclic peptide.**
1031

	Retromer + RT-L4		***apo* Retromer**	
EMDB ID	D_1000253090		D_1000253118	
Microscope	ThermoFisher FEI Titan Krios G3i Vanderbilt V-CEM	FEI Titan Krios Krios2 NRAMM Data collection 1	FEI Titan Krios Krios3 NRAMM Data collection 2	FEI Titan Krios Krios3 NRAMM Data collection 3
Cs	2.7 mm	2.7 mm	2.7 mm	2.7 mm
Voltage	300 keV	300 keV	300 keV	300 keV
Detector	ThermoFisher Falcon 3 direct electron detector	Gatan K2 Summit direct electron detector	Gatan K2 Summit direct electron detector	Gatan K2 Summit direct electron detector
Magnification	120,000x	105,000x	105,000x	105,000x
Pixel size	0.6811Å/pix	1.096Å/pix	1.06Å/pix (rescaled to 1.096Å/pix with motioncorr2 script)	1.06Å/pix (rescaled to 1.096Å/pix with motioncorr2 script)
Dose rate	$1.4e^-/Å^2/sec$	$\sim 8e^-/Å^2/sec$	$\sim 8e^-/Å^2/sec$	$\sim 8e^-/Å^2/sec$
Total dose	$50e^-/A^2$	$69.34e^-/Å^2$	$73.92e^-/Å^2$	$73.92e^-/Å^2$
Tilt	+/-30°	N/A	N/A	+/-15°
Defocus range	-0.8 to -2.6µm	-0.7 to 2.6µm	-0.8 to -4.4µm	-0.8 to -4.7µm
Number of micrographs	4,791	1,480	1,299	891
Total particles (autopicked)	1,683,975	(250,500 particles selected from these datasets; Kendall *et al*., 2020)		207,026
Box size (Å)	501 Å		241 Å	
Particles in 2D classification	273,172		72,795	
Particles in final 3D model	45,330		43,808	
Symmetry	C1		C1	
Map resolution (masked FSC 0.143, RELION)	5.0 Å		4.9Å	
B-factor	-189		-114	

1032

1033 **Table S5: Thermodynamic parameters for the binding of Retromer and its partners in the presence of**
1034 **RT-D3 or RT-L4 cyclic peptides.**

	K_d (μM)	ΔH (kcal/mol)	ΔG (kcal/mol)	$-T\Delta S$ (kcal/mol)
TBC1D5$_{TBC}$				
Retromer + DMSO (Native)	0.37 ± 0.02	-2.5 ± 0.8	-8.8 ± 0.03	-6.2 ± 0.8
Retromer + RT-D3		No binding detected		
Retromer + RT-L4	0.19 ± 0.01	-5.7 ± 0.1	-9.2 ± 0.06	-3.5 ± 0.1
SNX27$_{PDZ}$				
Retromer + DMSO (Native)	13.0 ± 0.5	-1.1 ± 0.1	-6.7 ± 0.03	-5.6 ± 0.2
Retromer + RT-D3	15.1 ± 0.4	-1.2 ± 0.3	-6.6 ± 0.08	-5.4 ± 0.2
Retromer + RT-L4	8.2 ± 1.0	-5.5 ± 0.3	-6.9 ± 0.07	-1.4 ± 0.4
PTHR$_{586-593}$				
mSNX27$_{PDZ}$	5.2 ± 0.4	-10.6 ± 0.4	-7.2 ± 0.05	3.3 ± 0.4
Retromer + mSNX27$_{PDZ}$	2.4 ± 0.3	-11.1 ± 1.8	-7.7 ± 0.08	3.5 ± 1.9
Retromer + mSNX27$_{PDZ}$ + RT-L4	0.7 ± 0.1	-12.5 ± 0.6	-8.4 ± 0.05	4.3 ± 0.3
SNX3				
Retromer + DMT1* + DMSO (Native)	154 ± 25	-32.4 ± 9.8	-5.2 ± 0.14	27.1 ± 9.8
Retromer + DMT1* + RT-D3	164 ± 3	-33.2 ± 0.4	-5.2 ± 0.02	28.0 ± 0.4
Retromer + DMT1* + RT-L4	230.0 ± 14	-14.0 ± 0.6	-5.0 ± 0.03	9.0 ± 0.6
GST-Fam21$_{R19-R21}$				
Retromer + DMSO (Native)	10.6 ± 0.7	-16.5 ± 0.6	-6.8 ± 0.04	9.8 ± 0.9
Retromer + RT-D3	25.8 ± 0.5	-9.3 ± 3.3	-6.3 ± 0.02	4.0 ± 1.9
Retromer + RT-L4	2.8 ± 0.8	-26.0 ± 1.6	-7.5 ± 0.02	18.4 ± 1.8

1035 DMT1* corresponds to DMT1-II$_{550-568}$.

1036

1037 **Table S6. Thermodynamic parameters for the binding of Vps26 – Vps35 subcomplex with**
1038 **SNX3 in the presence of cargo peptide**.

	K_d (μM)	ΔH (kcal/mol)	ΔG (kcal/mol)	$-T\Delta S$ (kcal/mol)
Vps26A – Vps35$_{1\text{-}390}$ – DMT1-II$_{550\text{-}568}$: SNX3				
Native	149 ± 9	-14.6 ± 0.3	-5.2 ± 0.05	10.4 ± 1.6
Phosphomimetic mutant (pm)	61 ± 3	-18.7 ± 0.7	-5.8 ± 0.03	13.0 ± 0.8
QRFE to AAAA mutant	50 ± 2	-23.0 ± 3.2	-5.9 ± 0.03	17.1 ± 3.0
ΔC-term. tail (ΔC)	32 ± 1	-28.3 ± 0.2	-6.1 ± 0.04	22.1 ± 0.4
Vps26A – Vps35$_{1\text{-}390}$ – CIMPR$_{2347\text{-}2376}$: SNX3				
Native	201 ± 9	-11.8 ± 0.9	-5.1 ± 0.03	6.6 ± 0.8
Vps26A – Vps35$_{1\text{-}390}$: SNX3				
Native		No binding detected		
Phosphomimetic mutant (pm)		No binding detected		
ΔC-term.tail (ΔC)		No binding detected		
Vps26B – Vps35$_{1\text{-}390}$ – DMT1-II$_{550\text{-}568}$: SNX3				
Native	193 ± 4	-13.8 ± 0.5	-5.1 ± 0.02	8.7 ± 0.6
Phosphomimetic mutant (pm)	64 ± 2	-12.3 ± 2.3	-5.7 ± 0.02	7.1 ± 1.5
ΔC-term.tail (ΔC)	34 ± 2	-24.7 ± 2.7	-6.1 ± 0.03	18.6 ± 2.7
Vps26B – Vps35$_{1\text{-}390}$: SNX3				
Native		No binding detected		
Phosphomimetic mutant (pm)		No binding detected		
ΔC-term.tail (ΔC)		No binding detected		

1039

1040 **References**

1041 1. Cullen, P.J. & Steinberg, F. To degrade or not to degrade: mechanisms and significance of endocytic
1042 recycling. *Nat Rev Mol Cell Biol* **19**, 679-696 (2018).

1043 2. Chen, K.E., Healy, M.D. & Collins, B.M. Towards a molecular understanding of endosomal
1044 trafficking by Retromer and Retriever. *Traffic* **20**, 465-478 (2019).

1045 3. Weeratunga, S., Paul, B. & Collins, B.M. Recognising the signals for endosomal trafficking. *Curr*
1046 *Opin Cell Biol* **In press** (2020).

1047 4. Kerr, M.C. *et al.* A novel mammalian retromer component, Vps26B. *Traffic* **6**, 991-1001 (2005).

1048 5. Burd, C. & Cullen, P.J. Retromer: a master conductor of endosome sorting. *Cold Spring Harb*
1049 *Perspect Biol* **6** (2014).

1050 6. Heucken, N. & Ivanov, R. The retromer, sorting nexins and the plant endomembrane protein
1051 trafficking. *J Cell Sci* **131** (2018).

1052 7. Ma, M. & Burd, C.G. Retrograde trafficking and plasma membrane recycling pathways of the
1053 budding yeast Saccharomyces cerevisiae. *Traffic* **21**, 45-59 (2020).

1054 8. Seaman, M.N.J. Retromer and Its Role in Regulating Signaling at Endosomes. *Prog Mol Subcell*
1055 *Biol* **57**, 137-149 (2018).

1056 9. Seaman, M.N., McCaffery, J.M. & Emr, S.D. A membrane coat complex essential for endosome-to-
1057 Golgi retrograde transport in yeast. *J Cell Biol* **142**, 665-681 (1998).

1058 10. Zhang, H. *et al.* The Retromer Complex and Sorting Nexins in Neurodegenerative Diseases. *Front*
1059 *Aging Neurosci* **10**, 79 (2018).

1060 11. Harterink, M. *et al.* A SNX3-dependent retromer pathway mediates retrograde transport of the Wnt
1061 sorting receptor Wntless and is required for Wnt secretion. *Nat Cell Biol* **13**, 914-923 (2011).

1062 12. Cui, Y. *et al.* Retromer has a selective function in cargo sorting via endosome transport carriers. *J*
1063 *Cell Biol* **218**, 615-631 (2019).

1064 13. Steinberg, F. *et al.* A global analysis of SNX27-retromer assembly and cargo specificity reveals a
1065 function in glucose and metal ion transport. *Nat Cell Biol* **15**, 461-471 (2013).

1066 14. Clairfeuille, T. *et al.* A molecular code for endosomal recycling of phosphorylated cargos by the
1067 SNX27-retromer complex. *Nat Struct Mol Biol* **23**, 921-932 (2016).

1068 15. Temkin, P. *et al.* SNX27 mediates retromer tubule entry and endosome-to-plasma membrane
1069 trafficking of signalling receptors. *Nat Cell Biol* **13**, 715-721 (2011).

1070 16. Vilarino-Guell, C. *et al.* VPS35 mutations in Parkinson disease. *Am J Hum Genet* **89**, 162-167
1071 (2011).

1072 17. Zimprich, A. *et al.* A mutation in VPS35, encoding a subunit of the retromer complex, causes late-
1073 onset Parkinson disease. *Am J Hum Genet* **89**, 168-175 (2011).

1074 18. Follett, J. *et al.* The Vps35 D620N mutation linked to Parkinson's disease disrupts the cargo sorting
1075 function of retromer. *Traffic* **15**, 230-244 (2014).

1076 19. McGough, I.J. *et al.* Retromer binding to FAM21 and the WASH complex is perturbed by the
1077 Parkinson disease-linked VPS35(D620N) mutation. *Curr Biol* **24**, 1670-1676 (2014).

1078 20. Small, S.A. & Petsko, G.A. Retromer in Alzheimer disease, Parkinson disease and other
1079 neurological disorders. *Nat Rev Neurosci* **16**, 126-132 (2015).

1080 21. Tang, F.L. *et al.* VPS35 Deficiency or Mutation Causes Dopaminergic Neuronal Loss by Impairing
1081 Mitochondrial Fusion and Function. *Cell Rep* **12**, 1631-1643 (2015).

1082 22. Tsika, E. *et al.* Parkinson's disease-linked mutations in VPS35 induce dopaminergic
1083 neurodegeneration. *Hum Mol Genet* **23**, 4621-4638 (2014).

1084 23. Zavodszky, E. *et al.* Mutation in VPS35 associated with Parkinson's disease impairs WASH complex
1085 association and inhibits autophagy. *Nat Commun* **5**, 3828 (2014).

1086 24. Chen, X. *et al.* Parkinson's disease-linked D620N VPS35 knockin mice manifest tau neuropathology
1087 and dopaminergic neurodegeneration. *Proc Natl Acad Sci U S A* **116**, 5765-5774 (2019).

1088 25. Cui, Y., Yang, Z. & Teasdale, R.D. The functional roles of retromer in Parkinson's disease. *FEBS*
1089 *Lett* **592**, 1096-1112 (2018).

1090 26. McMillan, K.J. *et al.* Atypical parkinsonism-associated retromer mutant alters endosomal sorting of
1091 specific cargo proteins. *J Cell Biol* **214**, 389-399 (2016).

1092 27. Otero-Ramirez, M.E., Passioura, T. & Suga, H. Structural Features and Binding Modes of Thioether-
1093 Cyclized Peptide Ligands. *Biomedicines* **6** (2018).

1094 28. Tang, F.L. *et al.* VPS35 in Dopamine Neurons Is Required for Endosome-to-Golgi Retrieval of
1095 Lamp2a, a Receptor of Chaperone-Mediated Autophagy That Is Critical for alpha-Synuclein

1096 Degradation and Prevention of Pathogenesis of Parkinson's Disease. *J Neurosci* **35**, 10613-10628
1097 (2015).

1098 29. Wang, W. *et al.* Parkinson's disease-associated mutant VPS35 causes mitochondrial dysfunction by
1099 recycling DLP1 complexes. *Nat Med* **22**, 54-63 (2016).

1100 30. Williams, E.T., Chen, X. & Moore, D.J. VPS35, the Retromer Complex and Parkinson's Disease. *J*
1101 *Parkinsons Dis* **7**, 219-233 (2017).

1102 31. Small, S.A. *et al.* Model-guided microarray implicates the retromer complex in Alzheimer's disease.
1103 *Ann Neurol* **58**, 909-919 (2005).

1104 32. Wen, L. *et al.* VPS35 haploinsufficiency increases Alzheimer's disease neuropathology. *J Cell Biol*
1105 **195**, 765-779 (2011).

1106 33. Vardarajan, B.N. *et al.* Identification of Alzheimer disease-associated variants in genes that regulate
1107 retromer function. *Neurobiol Aging* **33**, 2231 e2215-2231 e2230 (2012).

1108 34. Ansell-Schultz, A., Reyes, J.F., Samuelsson, M. & Hallbeck, M. Reduced retromer function results
1109 in the accumulation of amyloid-beta oligomers. *Mol Cell Neurosci* **93**, 18-26 (2018).

1110 35. Lucin, K.M. *et al.* Microglial beclin 1 regulates retromer trafficking and phagocytosis and is
1111 impaired in Alzheimer's disease. *Neuron* **79**, 873-886 (2013).

1112 36. Rovelet-Lecrux, A. *et al.* De novo deleterious genetic variations target a biological network centered
1113 on Abeta peptide in early-onset Alzheimer disease. *Mol Psychiatry* **20**, 1046-1056 (2015).

1114 37. Tammineni, P., Jeong, Y.Y., Feng, T., Aikal, D. & Cai, Q. Impaired axonal retrograde trafficking of
1115 the retromer complex augments lysosomal deficits in Alzheimer's disease neurons. *Hum Mol Genet*
1116 **26**, 4352-4366 (2017).

1117 38. Muzio, L. *et al.* Retromer stabilization results in neuroprotection in a model of Amyotrophic Lateral
1118 Sclerosis. *Nat Commun* **11**, 3848 (2020).

1119 39. Toh, W.H. & Gleeson, P.A. Dysregulation of intracellular trafficking and endosomal sorting in
1120 Alzheimer's disease: controversies and unanswered questions. *Biochem J* **473**, 1977-1993 (2016).

1121 40. Menzies, F.M. *et al.* Autophagy and Neurodegeneration: Pathogenic Mechanisms and Therapeutic
1122 Opportunities. *Neuron* **93**, 1015-1034 (2017).

1123 41. Follett, J., Bugarcic, A., Collins, B.M. & Teasdale, R.D. Retromer's Role in Endosomal Trafficking
1124 and Impaired Function in Neurodegenerative Diseases. *Curr Protein Pept Sci* **18**, 687-701 (2017).

1125 42. Abeliovich, A. & Gitler, A.D. Defects in trafficking bridge Parkinson's disease pathology and
1126 genetics. *Nature* **539**, 207-216 (2016).

1127 43. Vagnozzi, A.N. & Pratico, D. Endosomal sorting and trafficking, the retromer complex and
1128 neurodegeneration. *Mol Psychiatry* **24**, 857-868 (2019).

1129 44. Vidyadhara, D.J., Lee, J.E. & Chandra, S.S. Role of the endolysosomal system in Parkinson's
1130 disease. *J Neurochem* **150**, 487-506 (2019).

1131 45. McMillan, K.J., Korswagen, H.C. & Cullen, P.J. The emerging role of retromer in neuroprotection.
1132 *Curr Opin Cell Biol* **47**, 72-82 (2017).

1133 46. Munsie, L.N. *et al.* Retromer-dependent neurotransmitter receptor trafficking to synapses is altered
1134 by the Parkinson's disease VPS35 mutation p.D620N. *Hum Mol Genet* **24**, 1691-1703 (2015).

1135 47. Wang, C. *et al.* VPS35 regulates cell surface recycling and signaling of dopamine receptor D1.
1136 *Neurobiol Aging* **46**, 22-31 (2016).

1137 48. Fjorback, A.W. *et al.* Retromer binds the FANSHY sorting motif in SorLA to regulate amyloid
1138 precursor protein sorting and processing. *J Neurosci* **32**, 1467-1480 (2012).

1139 49. Ueda, N., Tomita, T., Yanagisawa, K. & Kimura, N. Retromer and Rab2-dependent trafficking
1140 mediate PS1 degradation by proteasomes in endocytic disturbance. *J Neurochem* **137**, 647-658
1141 (2016).

1142 50. Vieira, S.I. *et al.* Retrieval of the Alzheimer's amyloid precursor protein from the endosome to the
1143 TGN is S655 phosphorylation state-dependent and retromer-mediated. *Mol Neurodegener* **5**, 40
1144 (2010).

1145 51. Wang, C.L. *et al.* VPS35 regulates developing mouse hippocampal neuronal morphogenesis by
1146 promoting retrograde trafficking of BACE1. *Biol Open* **1**, 1248-1257 (2012).

1147 52. Jimenez-Orgaz, A. *et al.* Control of RAB7 activity and localization through the retromer-TBC1D5
1148 complex enables RAB7-dependent mitophagy. *EMBO J* **37**, 235-254 (2018).

1149 53. Wang, W., Ma, X., Zhou, L., Liu, J. & Zhu, X. A conserved retromer sorting motif is essential for
1150 mitochondrial DLP1 recycling by VPS35 in Parkinson's disease model. *Hum Mol Genet* **26**, 781-789
1151 (2017).

1152 54. Follett, J. *et al.* Parkinson Disease-linked Vps35 R524W Mutation Impairs the Endosomal
1153 Association of Retromer and Induces alpha-Synuclein Aggregation. *J Biol Chem* **291**, 18283-18298
1154 (2016).

1155 55. Miura, E. *et al.* VPS35 dysfunction impairs lysosomal degradation of alpha-synuclein and
1156 exacerbates neurotoxicity in a Drosophila model of Parkinson's disease. *Neurobiol Dis* **71**, 1-13
1157 (2014).

1158 56. Tang, F.L. *et al.* Coupling of terminal differentiation deficit with neurodegenerative pathology in
1159 Vps35-deficient pyramidal neurons. *Cell Death Differ* (2020).

1160 57. Appel, J.R. *et al.* Increased Microglial Activity, Impaired Adult Hippocampal Neurogenesis, and
1161 Depressive-like Behavior in Microglial VPS35-Depleted Mice. *J Neurosci* **38**, 5949-5968 (2018).

1162 58. Bayliss, R., Wheeldon, J., Caucheteux, S.M., Niessen, C.M. & Piguet, V. Identification of host
1163 trafficking genes required for HIV-1 virological synapse formation in dendritic cells. *J Virol* (2020).

1164 59. Ganti, K. *et al.* Interaction of the Human Papillomavirus E6 Oncoprotein with Sorting Nexin 27
1165 Modulates Endocytic Cargo Transport Pathways. *PLoS Pathog* **12**, e1005854 (2016).

1166 60. Groppelli, E., Len, A.C., Granger, L.A. & Jolly, C. Retromer regulates HIV-1 envelope glycoprotein
1167 trafficking and incorporation into virions. *PLoS Pathog* **10**, e1004518 (2014).

1168 61. Hsiao, J.C. *et al.* Intracellular Transport of Vaccinia Virus in HeLa Cells Requires WASH-
1169 VPEF/FAM21-Retromer Complexes and Recycling Molecules Rab11 and Rab22. *J Virol* **89**, 8365-
1170 8382 (2015).

1171 62. Kingston, D. *et al.* Inhibition of retromer activity by herpesvirus saimiri tip leads to CD4
1172 downregulation and efficient T cell transformation. *J Virol* **85**, 10627-10638 (2011).

1173 63. Lipovsky, A. *et al.* Genome-wide siRNA screen identifies the retromer as a cellular entry factor for
1174 human papillomavirus. *Proc Natl Acad Sci U S A* **110**, 7452-7457 (2013).

1175 64. Muscolino, E. *et al.* Herpesviruses induce aggregation and selective autophagy of host signalling
1176 proteins NEMO and RIPK1 as an immune-evasion mechanism. *Nat Microbiol* **5**, 331-342 (2020).

1177 65. Pim, D., Broniarczyk, J., Bergant, M., Playford, M.P. & Banks, L. A Novel PDZ Domain Interaction
1178 Mediates the Binding between Human Papillomavirus 16 L2 and Sorting Nexin 27 and Modulates
1179 Virion Trafficking. *J Virol* **89**, 10145-10155 (2015).

1180 66. Popa, A. *et al.* Direct binding of retromer to human papillomavirus type 16 minor capsid protein L2
1181 mediates endosome exit during viral infection. *PLoS Pathog* **11**, e1004699 (2015).

1182 67. Yin, P., Hong, Z., Yang, X., Chung, R.T. & Zhang, L. A role for retromer in hepatitis C virus
1183 replication. *Cell Mol Life Sci* **73**, 869-881 (2016).

1184 68. Daniloski, Z. *et al.* Identification of Required Host Factors for SARS-CoV-2 Infection in Human
1185 Cells. *Cell* (2020).

1186 69. Xie, J., Heim, E.N., Crite, M. & DiMaio, D. TBC1D5-Catalyzed Cycling of Rab7 Is Required for
1187 Retromer-Mediated Human Papillomavirus Trafficking during Virus Entry. *Cell Rep* **31**, 107750
1188 (2020).

1189 70. Pim, D., Broniarczyk, J., Siddiqa, A., Massimi, P. & Banks, L. Human Papillomavirus type 16 L2
1190 recruits both retromer and retriever complexes during retrograde trafficking of the viral genome to
1191 the cell nucleus. *J Virol* (2020).

1192 71. Barlocher, K. *et al.* Structural insights into Legionella RidL-Vps29 retromer subunit interaction
1193 reveal displacement of the regulator TBC1D5. *Nat Commun* **8**, 1543 (2017).

1194 72. Casanova, A. *et al.* A Role for the VPS Retromer in Brucella Intracellular Replication Revealed by
1195 Genomewide siRNA Screening. *mSphere* **4** (2019).

1196 73. Finsel, I. *et al.* The Legionella effector RidL inhibits retrograde trafficking to promote intracellular
1197 replication. *Cell Host Microbe* **14**, 38-50 (2013).

1198 74. McDonough, J.A. *et al.* Host pathways important for Coxiella burnetii infection revealed by
1199 genome-wide RNA interference screening. *mBio* **4**, e00606-00612 (2013).

1200 75. Miller, H.E., Larson, C.L. & Heinzen, R.A. Actin polymerization in the endosomal pathway, but not
1201 on the Coxiella-containing vacuole, is essential for pathogen growth. *PLoS Pathog* **14**, e1007005
1202 (2018).

1203 76. Romano-Moreno, M. *et al.* Molecular mechanism for the subversion of the retromer coat by the
1204 Legionella effector RidL. *Proc Natl Acad Sci U S A* **114**, E11151-E11160 (2017).

1205 77. Yao, J. *et al.* Mechanism of inhibition of retromer transport by the bacterial effector RidL. *Proc Natl*
1206 *Acad Sci U S A* **115**, E1446-E1454 (2018).

1207 78. Zhang, P., Monteiro da Silva, G., Deatherage, C., Burd, C. & DiMaio, D. Cell-Penetrating Peptide
1208 Mediates Intracellular Membrane Passage of Human Papillomavirus L2 Protein to Trigger
1209 Retrograde Trafficking. *Cell* **174**, 1465-1476 e1413 (2018).

1210 79. Zhang, P., Moreno, R., Lambert, P.F. & DiMaio, D. Cell-penetrating peptide inhibits retromer-
1211 mediated human papillomavirus trafficking during virus entry. *Proc Natl Acad Sci U S A* (2020).

1212 80. Boland, B. *et al.* Promoting the clearance of neurotoxic proteins in neurodegenerative disorders of
1213 ageing. *Nat Rev Drug Discov* **17**, 660-688 (2018).

1214 81. Eleuteri, S. & Albanese, A. VPS35-Based Approach: A Potential Innovative Treatment in
1215 Parkinson's Disease. *Front Neurol* **10**, 1272 (2019).

1216 82. Ringe, D. & Petsko, G.A. What are pharmacological chaperones and why are they interesting? *J Biol*
1217 **8**, 80 (2009).

1218 83. Small, S.A., Simoes-Spassov, S., Mayeux, R. & Petsko, G.A. Endosomal Traffic Jams Represent a
1219 Pathogenic Hub and Therapeutic Target in Alzheimer's Disease. *Trends Neurosci* **40**, 592-602
1220 (2017).

1221 84. Mecozzi, V.J. *et al.* Pharmacological chaperones stabilize retromer to limit APP processing. *Nat*
1222 *Chem Biol* **10**, 443-449 (2014).

1223 85. Chu, J. & Pratico, D. The retromer complex system in a transgenic mouse model of AD: influence of
1224 age. *Neurobiol Aging* **52**, 32-38 (2017).

1225 86. Li, J.G., Chiu, J., Ramanjulu, M., Blass, B.E. & Pratico, D. A pharmacological chaperone improves
1226 memory by reducing Abeta and tau neuropathology in a mouse model with plaques and tangles. *Mol*
1227 *Neurodegener* **15**, 1 (2020).

1228 87. Lin, G. *et al.* Phospholipase PLA2G6, a Parkinsonism-Associated Gene, Affects Vps26 and Vps35,
1229 Retromer Function, and Ceramide Levels, Similar to alpha-Synuclein Gain. *Cell Metab* **28**, 605-618
1230 e606 (2018).

1231 88. Singh, V. *et al.* Cholera toxin inhibits SNX27-retromer-mediated delivery of cargo proteins to the
1232 plasma membrane. *J Cell Sci* **131** (2018).

1233 89. Vagnozzi, A.N. *et al.* VPS35 regulates tau phosphorylation and neuropathology in tauopathy. *Mol*
1234 *Psychiatry* (2019).

1235 90. Young, J.E. *et al.* Stabilizing the Retromer Complex in a Human Stem Cell Model of Alzheimer's
1236 Disease Reduces TAU Phosphorylation Independently of Amyloid Precursor Protein. *Stem Cell*
1237 *Reports* **10**, 1046-1058 (2018).

1238 91. Bashiruddin, N.K. & Suga, H. Construction and screening of vast libraries of natural product-like
1239 macrocyclic peptides using in vitro display technologies. *Curr Opin Chem Biol* **24**, 131-138 (2015).

1240 92. Hipolito, C.J. & Suga, H. Ribosomal production and in vitro selection of natural product-like
1241 peptidomimetics: the FIT and RaPID systems. *Curr Opin Chem Biol* **16**, 196-203 (2012).

1242 93. Passioura, T. & Suga, H. A RaPID way to discover nonstandard macrocyclic peptide modulators of
1243 drug targets. *Chem Commun (Camb)* **53**, 1931-1940 (2017).

1244 94. Suga, H. Max-Bergmann award lecture:A RaPID way to discover bioactive nonstandard peptides
1245 assisted by the flexizyme and FIT systems. *J Pept Sci* **24** (2018).

1246 95. Jia, D. *et al.* Structural and mechanistic insights into regulation of the retromer coat by TBC1d5. *Nat*
1247 *Commun* **7**, 13305 (2016).

1248 96. Hierro, A. *et al.* Functional architecture of the retromer cargo-recognition complex. *Nature* **449**,
1249 1063-1067 (2007).

1250 97. Kovtun, O. *et al.* Structure of the membrane-assembled retromer coat determined by cryo-electron
1251 tomography. *Nature* **561**, 561-564 (2018).

1252 98. Lucas, M. *et al.* Structural Mechanism for Cargo Recognition by the Retromer Complex. *Cell* **167**,
1253 1623-1635 e1614 (2016).

1254 99. Norwood, S.J. *et al.* Assembly and solution structure of the core retromer protein complex. *Traffic*
1255 **12**, 56-71 (2011).

1256 100. Kendall, A.K. *et al.* Mammalian Retromer Is an Adaptable Scaffold for Cargo Sorting from
1257 Endosomes. *Structure* (2020).

1258 101. Hesketh, G.G. *et al.* VARP is recruited on to endosomes by direct interaction with retromer, where
1259 together they function in export to the cell surface. *Dev Cell* **29**, 591-606 (2014).

1260 102. Crawley-Snowdon, H. *et al.* Mechanism and evolution of the Zn-fingernail required for interaction
1261 of VARP with VPS29. *Nature Communications* **In Press** (2020).

1262 103. Crawley-Snowdon, H. *et al.* Mechanism and evolution of the Zn-fingernail required for interaction
1263 of VARP with VPS29. *Nat Commun* **11**, 5031 (2020).

1264 104. Jia, D., Gomez, T.S., Billadeau, D.D. & Rosen, M.K. Multiple repeat elements within the FAM21
1265 tail link the WASH actin regulatory complex to the retromer. *Mol Biol Cell* **23**, 2352-2361 (2012).

1266 105. Gallon, M. *et al.* A unique PDZ domain and arrestin-like fold interaction reveals mechanistic details
1267 of endocytic recycling by SNX27-retromer. *Proc Natl Acad Sci U S A* **111**, E3604-3613 (2014).

1268 106. Harrison, M.S. *et al.* A mechanism for retromer endosomal coat complex assembly with cargo. *Proc*
1269 *Natl Acad Sci U S A* **111**, 267-272 (2014).

1270 107. Hornbeck, P.V. *et al.* PhosphoSitePlus, 2014: mutations, PTMs and recalibrations. *Nucleic Acids Res*
1271 **43**, D512-520 (2015).

1272 108. Bugarcic, A. *et al.* Vps26A and Vps26B subunits define distinct retromer complexes. *Traffic* **12**,
1273 1759-1773 (2011).

1274 109. Teng, K.W. *et al.* Labeling proteins inside living cells using external fluorophores for microscopy.
1275 *Elife* **5** (2016).

1276 110. Harbour, M.E. *et al.* The cargo-selective retromer complex is a recruiting hub for protein complexes
1277 that regulate endosomal tubule dynamics. *J Cell Sci* **123**, 3703-3717 (2010).

1278 111. Patel, K. *et al.* Cyclic peptides can engage a single binding pocket through multiple, entirely
1279 divergent modes. *Biorxiv* **Epub** (2019).

1280 112. McNally, K.E. *et al.* Retriever is a multiprotein complex for retromer-independent endosomal cargo
1281 recycling. *Nat Cell Biol* **19**, 1214-1225 (2017).

1282 113. Banos-Mateos, S., Rojas, A.L. & Hierro, A. VPS29, a tweak tool of endosomal recycling. *Curr Opin*
1283 *Cell Biol* **59**, 81-87 (2019).

1284 114. Collins, B.M. *et al.* Structure of Vps26B and mapping of its interaction with the retromer protein
1285 complex. *Traffic* **9**, 366-379 (2008).

1286 115. Cardote, T.A. & Ciulli, A. Cyclic and Macrocyclic Peptides as Chemical Tools To Recognise
1287 Protein Surfaces and Probe Protein-Protein Interactions. *ChemMedChem* **11**, 787-794 (2016).

1288 116. Qian, Z., Dougherty, P.G. & Pei, D. Targeting intracellular protein-protein interactions with cell-
1289 permeable cyclic peptides. *Curr Opin Chem Biol* **38**, 80-86 (2017).

1290 117. Zorzi, A., Deyle, K. & Heinis, C. Cyclic peptide therapeutics: past, present and future. *Curr Opin*
1291 *Chem Biol* **38**, 24-29 (2017).

1292 118. Vinogradov, A.A., Yin, Y. & Suga, H. Macrocyclic Peptides as Drug Candidates: Recent Progress
1293 and Remaining Challenges. *J Am Chem Soc* **141**, 4167-4181 (2019).

1294 119. Nielsen, D.S. *et al.* Orally Absorbed Cyclic Peptides. *Chem Rev* **117**, 8094-8128 (2017).

1295 120. Rogers, J.M., Passioura, T. & Suga, H. Nonproteinogenic deep mutational scanning of linear and
1296 cyclic peptides. *Proc Natl Acad Sci U S A* **115**, 10959-10964 (2018).

1297 121. Walport, L.J., Obexer, R. & Suga, H. Strategies for transitioning macrocyclic peptides to cell-
1298 permeable drug leads. *Curr Opin Biotechnol* **48**, 242-250 (2017).

1299 122. Teasdale, R.D., Loci, D., Houghton, F., Karlsson, L. & Gleeson, P.A. A large family of endosome-
1300 localized proteins related to sorting nexin 1. *Biochem J* **358**, 7-16 (2001).

1301 123. Collins, B.M., Skinner, C.F., Watson, P.J., Seaman, M.N. & Owen, D.J. Vps29 has a
1302 phosphoesterase fold that acts as a protein interaction scaffold for retromer assembly. *Nat Struct Mol*
1303 *Biol* **12**, 594-602 (2005).

1304 124. Ghai, R. *et al.* Phosphoinositide binding by the SNX27 FERM domain regulates its localization at
1305 the immune synapse of activated T-cells. *J Cell Sci* **128**, 553-565 (2015).

1306 125. Teng, K.W. *et al.* Labeling Proteins Inside Living Cells Using External Fluorophores for
1307 Fluorescence Microscopy. *Elife* **6** (2017).

1308 126. Kabsch, W. Xds. *Acta Crystallogr D Biol Crystallogr* **66**, 125-132 (2010).

1309 127. Evans, P.R. & Murshudov, G.N. How good are my data and what is the resolution? *Acta Crystallogr*
1310 *D Biol Crystallogr* **69**, 1204-1214 (2013).

1311 128. McCoy, A.J. *et al.* Phaser crystallographic software. *J Appl Crystallogr* **40**, 658-674 (2007).

1312 129. Adams, P.D. *et al.* PHENIX: a comprehensive Python-based system for macromolecular structure
1313 solution. *Acta Crystallogr D Biol Crystallogr* **66**, 213-221 (2010).

1314 130. Chen, V.B. *et al.* MolProbity: all-atom structure validation for macromolecular crystallography. *Acta*
1315 *Crystallogr D Biol Crystallogr* **66**, 12-21 (2010).

1316 131. Notredame, C., Higgins, D.G. & Heringa, J. T-Coffee: A novel method for fast and accurate multiple
1317 sequence alignment. *J Mol Biol* **302**, 205-217 (2000).

1318 132. Ashkenazy, H. *et al.* ConSurf 2016: an improved methodology to estimate and visualize
1319 evolutionary conservation in macromolecules. *Nucleic Acids Res* **44**, W344-350 (2016).

1320 133. Holm, L. & Rosenstrom, P. Dali server: conservation mapping in 3D. *Nucleic Acids Res* **38**, W545-
1321 549 (2010).

1322 134. Carragher, B. *et al.* Leginon: An automated system for acquisition of images from vitreous ice
1323 specimens. *Journal of Structural Biology* **132**, 33-45 (2000).

1324 135. Zhang, K. Gctf: Real-time CTF determination and correction. *J Struct Biol* **193**, 1-12 (2016).

1325 136. Zivanov, J. *et al.* New tools for automated high-resolution cryo-EM structure determination in
1326 RELION-3. *Elife* **7** (2018).

1327 137. Pettersen, E.F. *et al.* UCSF Chimera--a visualization system for exploratory research and analysis. *J*
1328 *Comput Chem* **25**, 1605-1612 (2004).

1329 138. Chen, K.E., Tillu, V.A., Chandra, M. & Collins, B.M. Molecular Basis for Membrane Recruitment
1330 by the PX and C2 Domains of Class II Phosphoinositide 3-Kinase-C2alpha. *Structure* **26**, 1612-1625
1331 e1614 (2018).
1332

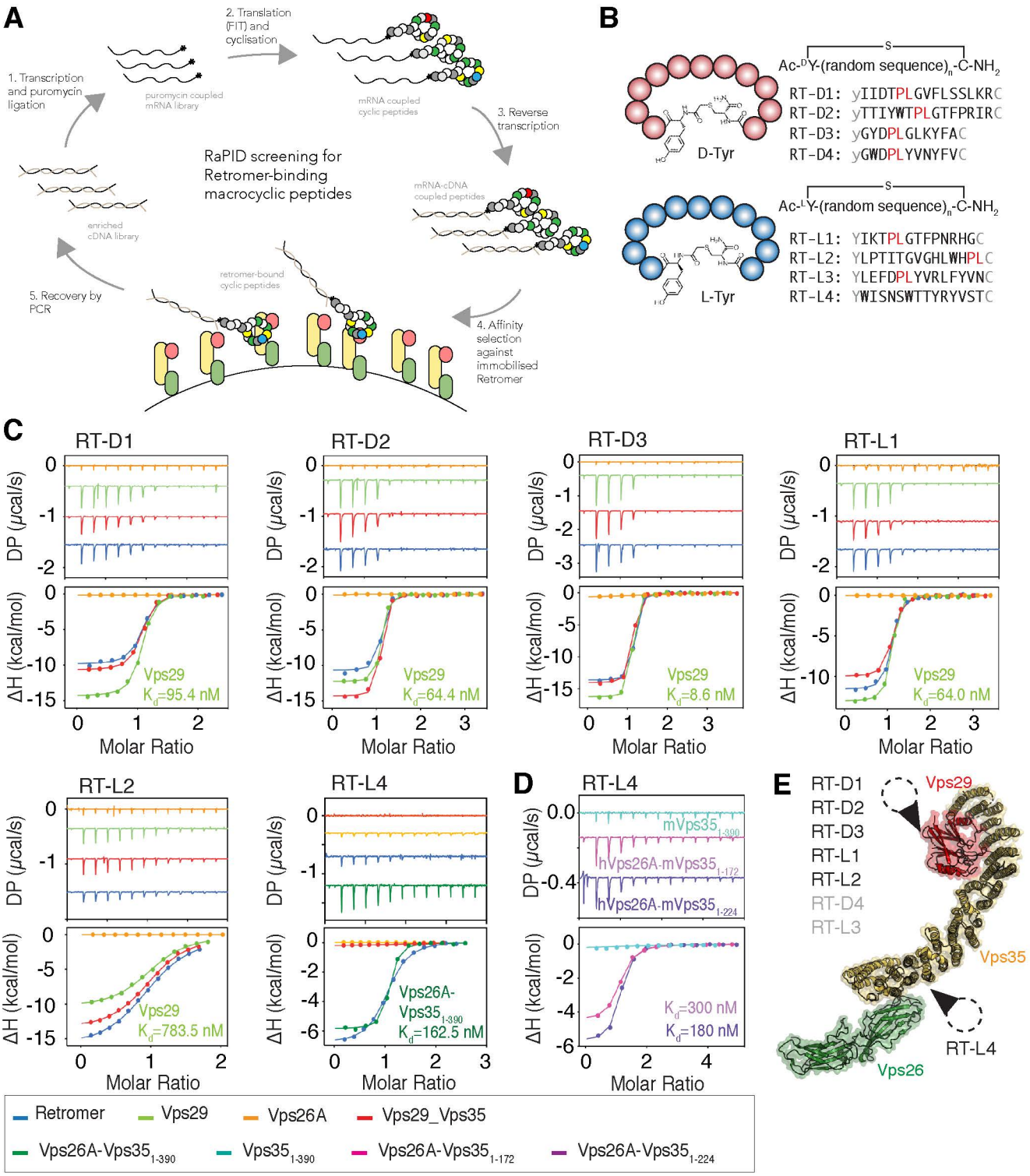

Figure 1. Cyclic peptides reveal strong binding characteristics with Retromer.
(A) Schematic diagram showing the RaPID system used to screen for cyclic peptides binding to Retromer. (B) Eight Retromer-binding macrocyclic peptides were identified with either N-chloroacetyl-D-tyrosine or N-chloroacetyl-L-tyrosine as initiating residues. (C) Binding of RT-D1, RT-D2, RT-D3, RT-L1, RT-L2, and RT-L4 with Retromer (blue), Vps29 (light green), Vps26A (orange), Vps29 – Vps35 (red) and Vps26A – Vps351-390 (dark green) by ITC. SPR binding curves for each peptide are shown in Fig. S3. (D) ITC thermogram showing that addition of α-helix 8 and 9 of Vps35 (residues 173 to 224) contributes to RT-L4 binding affinity but is not essential for interaction. All ITC graphs represent the integrated and normalized data fit with 1 to 1 ratio binding. The binding affinity (Kd) is given as mean of at least three independent experiments (Table S2). (E) Relative binding position of each cyclic peptide to Retromer based on the ITC measurements indicated on the structure of the mouse Retromer complex (PDB ID 6VAC) 100.

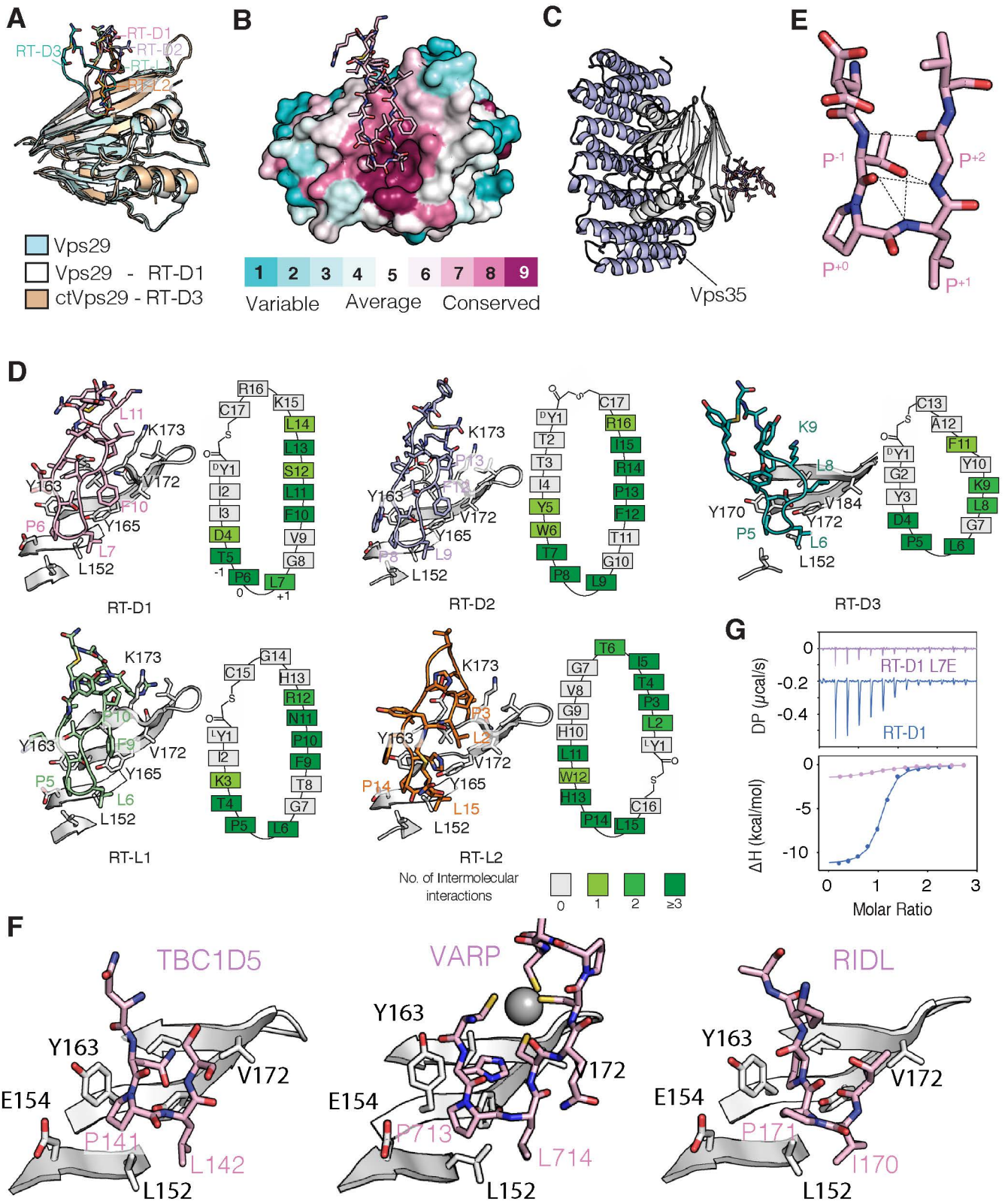

Figure 2. Crystal structures of Vps29 in complex with cyclic peptides.
(A) Superimposition of the crystal structures of Vps29 in complex with five macrocyclic peptides. (B) Sequence conservation mapped onto the hVPS29 structure surface highlights the conserved binding site for each of the cyclic peptides, with RT-D1 shown as an example. (C) Superimposition of the Vps29 – RT-D1 peptide complex with the Vps29 - Vps35483-780 crystal structure (PDB ID: 2R17) 96. The cyclic peptides bind opposite to the Vps35 interface. (D) Details of macrocyclic peptides in stick representation bound to Vps29. Schematic diagrams indicate the number of intermolecular contacts (salt bridge, hydrogen bonds and hydrophobic interactions) of each residue on the peptide with Vps29. The residues on the peptide with 0, 1, 2 and ≥3 contacts are shown in grey, light green, green and dark green boxes respectively. Each peptide utilises a core Pro-Leu sequence forming a ⊠-hairpin, labelled as position 0 and 1 for reference. Electron density for each peptide is shown in Fig. S3. (E) Close-up of the ⊠-hairpin conformation of the bound RT-D1 peptide. (F) TBC1D5 (PDB ID 5GTU) 95, VARP (PDB ID 6TL0) 103 and RIDL (PDB ID 5OSH) 76 bind to the same site of Vps29 using a similar ⊠-hairpin comprised of a Pro-Leu dipeptide sequence. For clarity, only the key residues involve in the contact are shown. (G) ITC thermogram for the titration of RT-D1 (purple) and RT-D1 L7E (blue) with Retromer showing the importance of Pro-Leu motif in the interaction. The graph represents the integrated and normalized data fit with a 1 to 1 binding ratio.

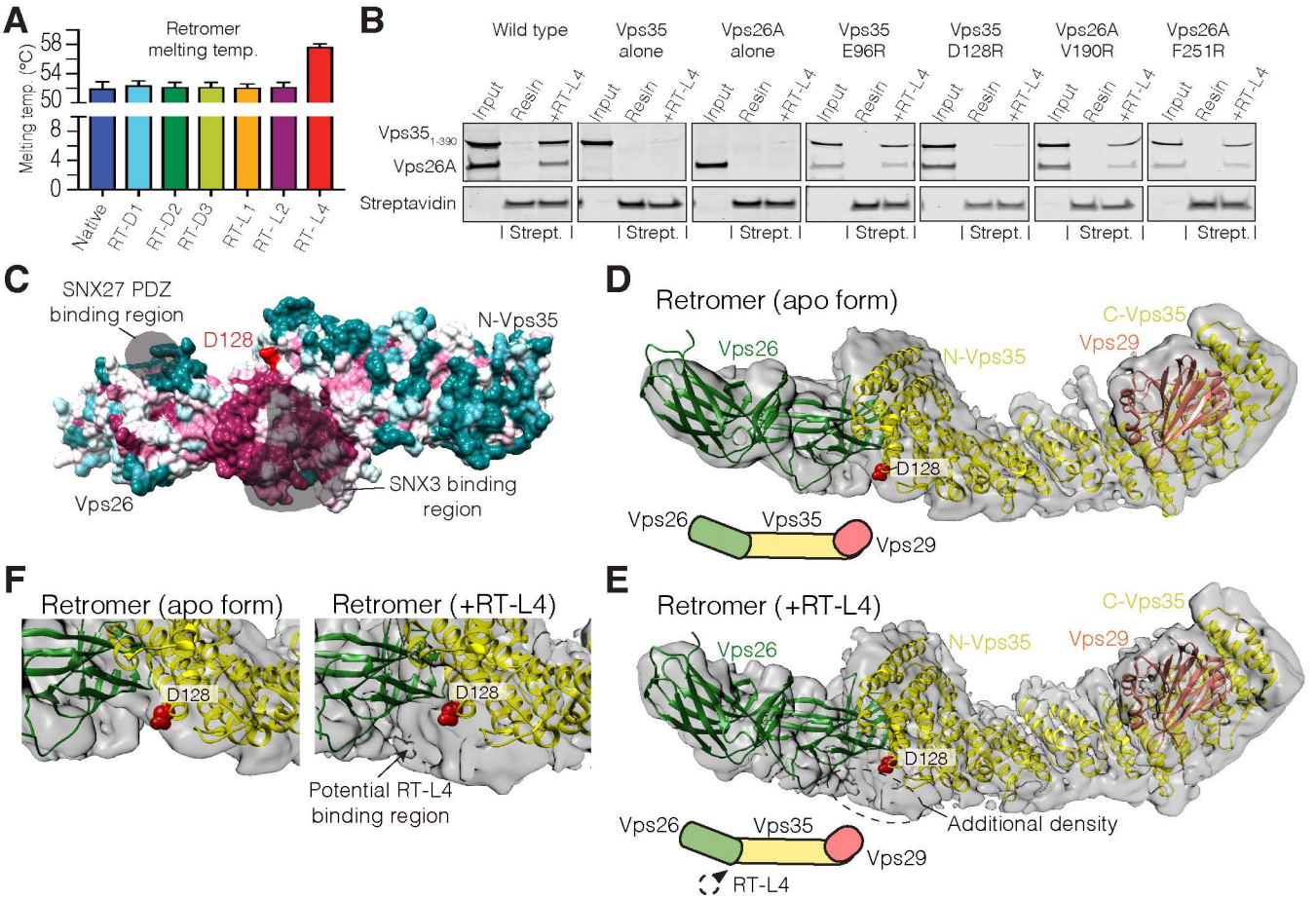

Figure 3. The RT-L4 macrocylic peptide is a molecular chaperone that binds Retromer at the Vps35-Vps26 interface.
(A) Bar graph summarizing the measured thermal unfolding temperatures (Tm) of Retromer in the presence of cyclic peptides. Raw data is shown in Fig. S4. (B) Pull-down assay showing the interaction of biotinylated RT-L4 bound to streptavidin-coated agarose beads with either wild-type Vps26A-Vps351-390 subcomplex or indicated point mutants. Individual Vps26A and Vps351-390 proteins do not bind the peptide, while the D128R mutation in Vps351-390 specifically blocks sub-complex interaction. (C) Sequence conservation map of Vps26A-Vps3512-470 subcomplex (PDB ID 5F0L) highlighting the proposed RT-L4 binding site, and its relationship to known binding sites for SNX3 98 and SNX27 105. (D) CryoEM reconstruction of the human Retromer (apo form) and (E) in complex with RT-L4. CryoEM density shown as transparent molecular envelope, with crystal structures of Retromer subcomplexes (PDB ID 2R17 and 5F0L) overlapped to the map (contoured at 4.7σ). The additional density seen on addition of the cyclic peptide added Retromer supports the mutagenesis data indicating RT-L4 binds at the Vps26 and Vps35 interface. (F) Enlarged view of the Vps26 and Vps35 interface highlighting the additional density in the CryoEM map of RT-L4 added Retromer but not in the apo form. For clarity, D128 of Vps35 is highlighted in red.

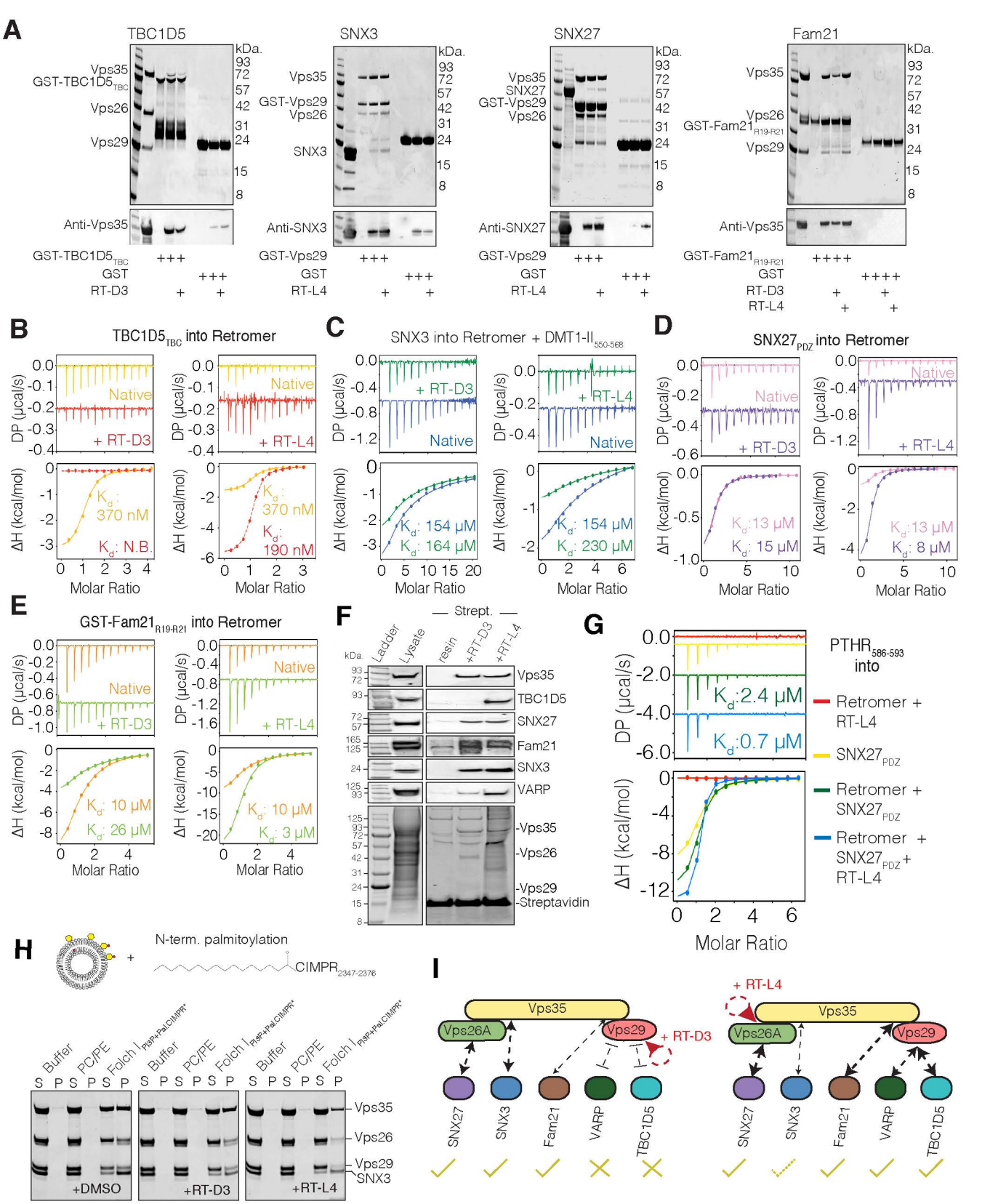

Figure 4. The effect of cyclic peptides on the interaction of Retromer with known regulatory and adaptor proteins.
(A) Interactions of Retromer with TBC1D5, SNX3, SNX27 and Fam21 in the presence of either RT-D3 or RT-L4. GST-TBC1D5TBC and GST-Fam21R19-R21 were used as baits for Retromer, while GST-tagged Retromer (Vps29 subunit) was used as bait for SNX3 and SNX27. (B) ITC measurement of TBC1D5TBC, (C) SNX3 (with DMT1-II550-568 present), (D) SNX27, and (E) GST-Fam21R19-R21 with Retromer in the presence or absence of RT-D3 or RT-L4. (F) Hela cell lysates were incubated with streptavidin agarose coated with biotinylated RT-D3 or RT-L4 and bound proteins subjected to SDS-PAGE and western blotting with antibodies against indicated proteins. (G) ITC measurement of PTHR586-593 cargo peptide 14 with SNX27PDZ alone (yellow), Retromer + RT-L4 (red), Retromer + SNX27PDZ (green) and Retromer + SNX27PDZ + RT-L4 (blue). RT-L4 allosterically enhances the affinity of Retromer + SNX27PDZ for cargo. The cargo peptide binds to SNX27 All ITC graphs represent the integrated and normalized data fit with a 1 to 1 binding ratio. The binding affinity (Kd) is given as mean of at least two independent experiments. (H) Liposome-binding assay of Retromer with membrane-associated SNX3 cargo complex in the presence of cyclic peptides. Multilamellar vesicles were composed of either control PC/PE lipids, or Folch I lipids containing added PtdIns(3)P and N-terminal palmitoylated CIMPR2347-2376 peptide (schematic diagram on top). "S" and "P" indicates unbound supernatant and bound pellet respectively. Control experiments are shown in Fig. S7B and S7C. (I) Schematic summarizing the effects of RT-D3 and RT-L4 on Retromer engagement with known regulatory and adaptor proteins.

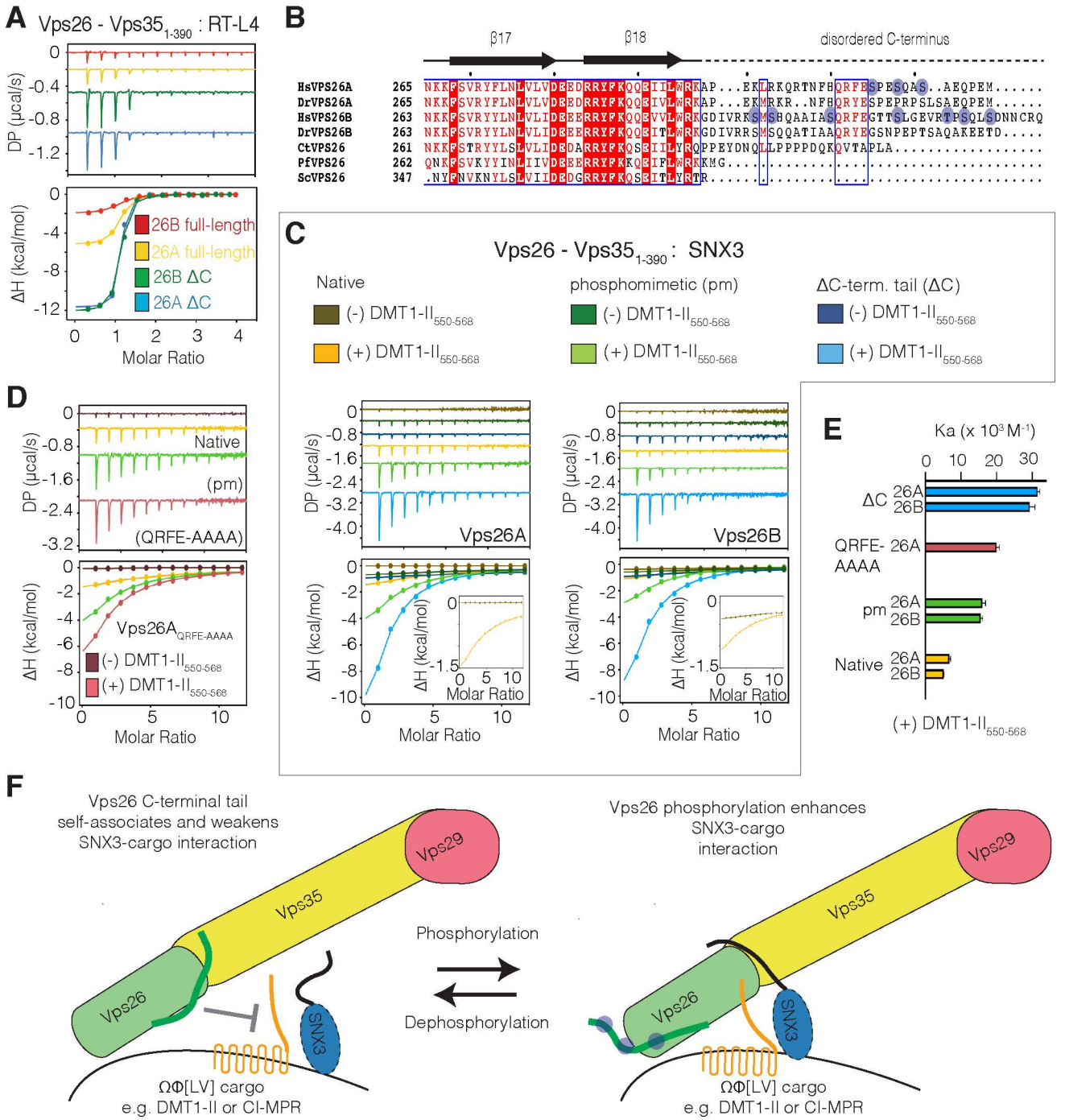

Figure 5. An autoinhibitory role for the disordered C-terminal tail of Vps26 in binding RT-L4 and SNX3.
(A) ITC thermogram for the titration of RT-L4 with Vps351-390 sub-complex with either full-length or C-terminal truncated Vps26A and Vps26B paralogues. (B) Sequence alignment of the C-terminal region of Vps26 highlighting the low-sequence similarity of the unstructured C-terminal tail. Sites of phosphorylation are indicated in blue (www.phosphosite.org) 107. Hs, Homo sapiens; Dr, Danio rerio; Ct, Chaetomium thermophilum; Pf, Plasmodium falciparum, Sc, Saccharomyces cerevisiae. (C) ITC measurement of SNX3 binding to native, phosphomimetic (pm), and C-terminal tail truncated (ΔC) versions of Vps26A/B – Vps351-390 subcomplexes. In each case, the presence of DMT1-II cargo peptide was required to detect SNX3 binding. (D) ITC measurement of SNX3 binding to QRFE-AAAA mutant Vps26A – Vps351-390. ITC thermograms in (A), (C) and (D) represent the integrated and normalized data fit with a 1 to 1 binding ratio. (E) Summary of binding affinities of SNX3 for each Vps26A/B – Vps351-390 subcomplex in the presence of DMT1-II550-568 cargo peptide. For clarity, the association constant (Kd¬-1) is shown. The binding affinity is given as mean of at least two independent experiments. (F) A proposed model for the autoinhibitory role of the Vps26 disordered C-terminal tails. Our data suggests that these tails can self-associate and reduce affinity for SNX3-cargo complexes, while removal of these tails or their release upon phosphorylation enhances SNX3-cargo association. The C-terminal sequence of Vps26B has greater autoinhibitory activity than Vps26A.

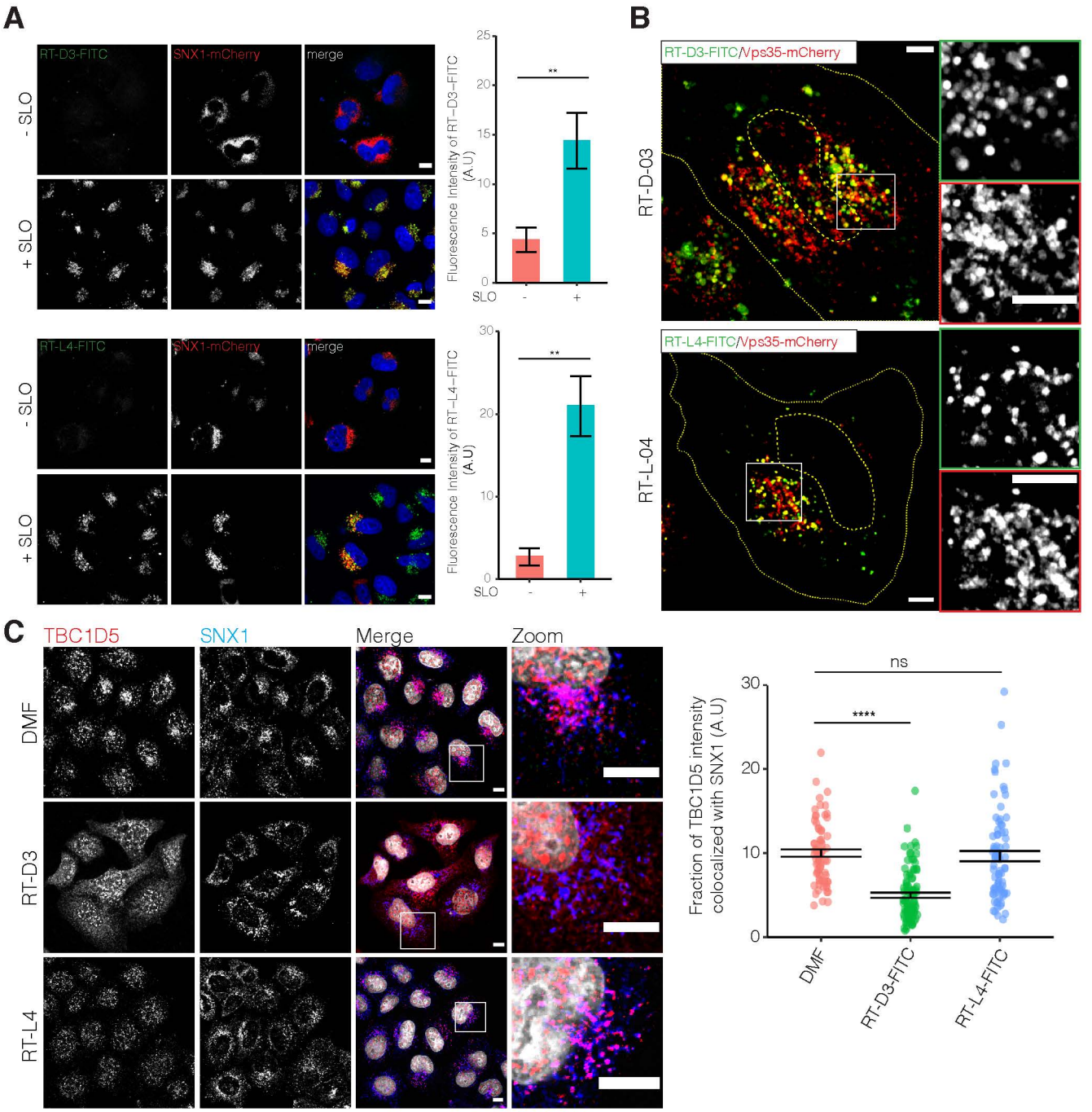

Figure 6. Macrocyclic peptides can be used to study Retromer localization in cells.
(A) Specific targeting of endosomal structures by streptolysin O (SLO) delivered cyclic peptides. HeLa cells transiently expressing SNX1-mCherry were exposed to SLO at 37°C for 9 min before incubating with the cyclic peptide RT-D3-FITC or RT-L4-FITC on ice for 5 min. Permeabilized cells were recovered in the recovery medium containing Hoechst 33342 for 20 min, then fixed in 4% PFA. The negative control (-SLO) shows no labeling of intracellular structures. Scale bar, 10 µm. Graphs show the fluorescence intensity of RT-D3-FITC or RT-L4-FITC in HeLa cells (means ± SEM). Two-tailed Student's t-test was used to determine the statistical significance (n=3). **, $P < 0.01$. (B) HeLa cells transiently expressing Vps35-mCherry were labeled by SLO-delivered cyclic peptide RT-D3-FITC or RT-L4-FITC, fixed in 4% PFA, and imaged by Airyscan super-resolution microscopy. Scale bar, 5 µm. (C) HeLa cells treated with SLO-delivered RT-D3-FITC, RT-L4-FITC, or DMF control were incubated in recovery medium for 2 h, fixed in ice-cold methanol, and co-immunolabeled with antibodies against endogenous TBC1D5 and SNX1, followed by Alexa Fluor-conjugated fluorescent secondary antibodies. Scale bar, 10 µm. The colocalization between TBC1D5 and SNX1 was quantified by Pearson's correlation coefficient and represented in the graph (means ± SEM). Two-tailed Student's t-test was utilized to determine the statistical significance (n=3). ****, $P < 0.0001$; ns, not significant.

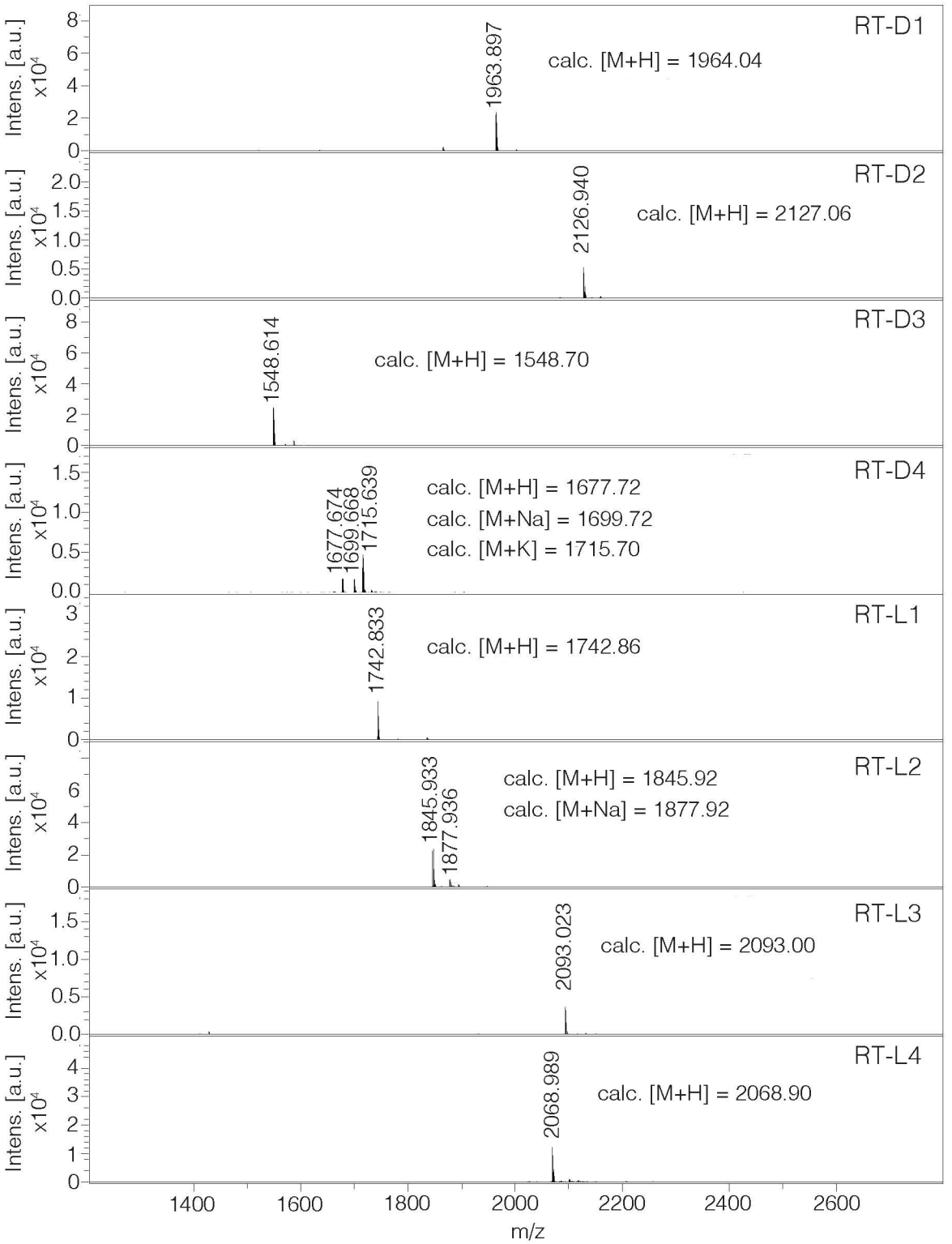

Figure S1. MALDI-TOF spectra of the Retromer associated cyclic peptides.
The molecular mass of RT-D1, RT-D2, RT-D3, RT-D4, RT-L1, RT-L2, RT-L3 and RT-L4 are shown in the spectrum.

A

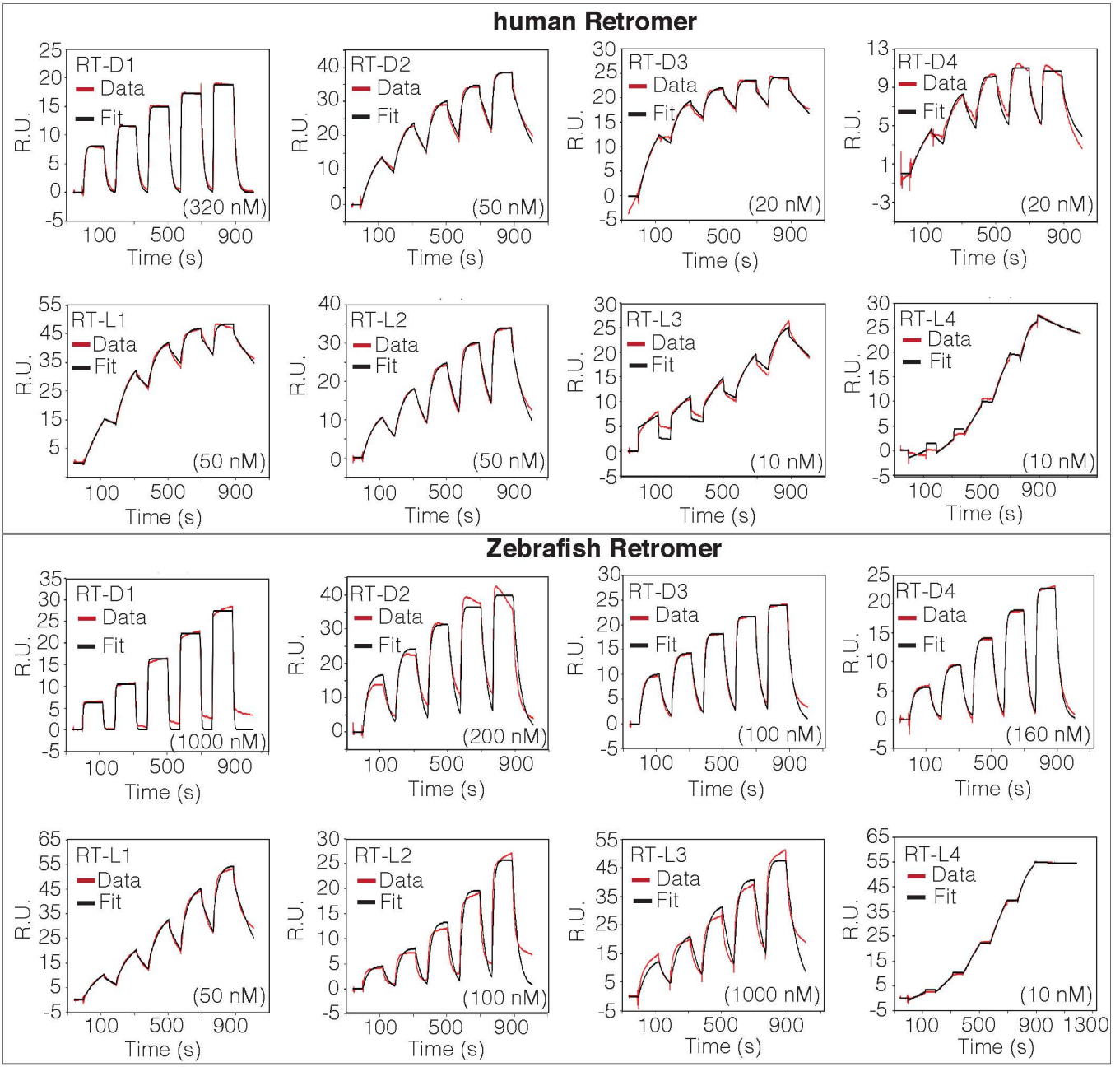

B

hRetromer

	K_{on} ($M^{-1}.S^{-1}$)	K_{off} (S^{-1})	K_D (nM)
RT-D1	2.25×10^6	0.070	31
RT-D2	1.82×10^6	0.005	2.9
RT-D3	6.57×10^6	0.002	0.3
RT-D4	1.79×10^{10}	18.43	1.0
RT-L1	1.54×10^6	0.002	1.4
RT-L2	2.02×10^6	0.010	5.2
RT-L3	1.52×10^6	0.002	1.1
RT-L4	4.91×10^6	0.001	0.2

zRetromer

	K_{on} ($M^{-1}.S^{-1}$)	K_{off} (S^{-1})	K_D (nM)
RT-D1	8.61×10^5	0.253	294
RT-D2	1.24×10^6	0.025	20
RT-D3	3.38×10^6	0.029	8.6
RT-D4	9.03×10^5	0.036	40
RT-L1	6.52×10^5	0.005	8.2
RT-L2	6.71×10^5	0.030	45
RT-L3	7.15×10^4	0.014	198
RT-L4	1.50×10^6	< 0.001	< 0.1

C

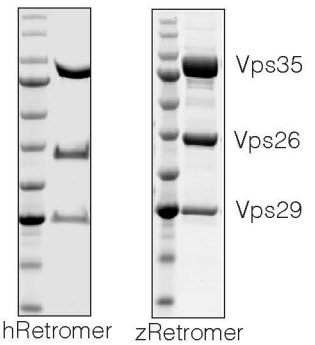

Figure S2. Preliminary SPR binding kinetics of Retromer-associated cyclic peptides.
(A) Single cycle kinetics experiments were performed using SPR with His-tagged human or zebrafish Retromer with varying concentrations of cyclic peptides. In each case, 2-fold serial dilutions of peptide were tested starting from a highest concentration of 200 or 1000 nM as indicated. (B) Binding kinetics of macrocyclic peptides for human and zebrafish Retromer complexes as determined by SPR. (C) Gels showing purity of human and zebrafish Retromer complexes used for Rapid peptide screening and SPR experiments.

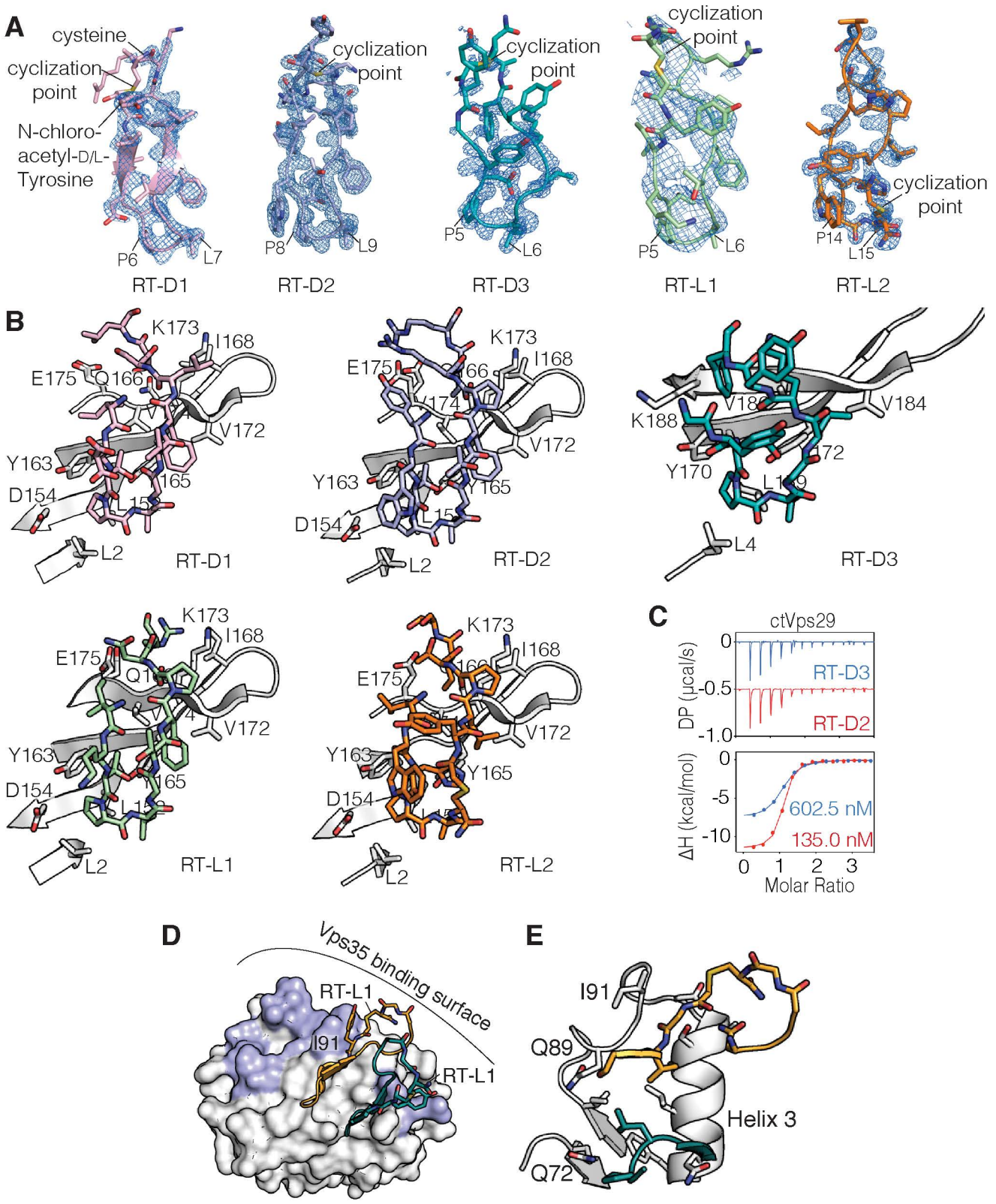

Figure S3. Interaction analysis of Vps29 and cyclic peptides.
(A) Structures of the Vps29 bound cyclic peptides, RT-D1, RT-D2, RT-D3, RT-L1 and RT-L2. For clarity, the main chain backbones are shown in ribbon and side chains are shown in stick form. The electron density shown corresponds to a simulated-annealing OMIT Fo - Fc map contoured at 3σ. (B) Highlighted details of the residues involved in the interactions between Vps29 and bound macrocyclic peptides. (C) ITC thermogram for the titration of RT-D2 (red line) and RT-D3 (blue line) with ctVps29. The graph represents the integrated and normalized data fit with a 1 to 1 binding ratio. The binding affinity (Kd) is given as mean of three independent experiments. (D) Surface and (E) cartoon representations of the human Vps29 – RT-L1 structure highlighting the secondary binding site located opposite to the primary common binding site. Residues involve in contact with Vps35 are shown in light blue.

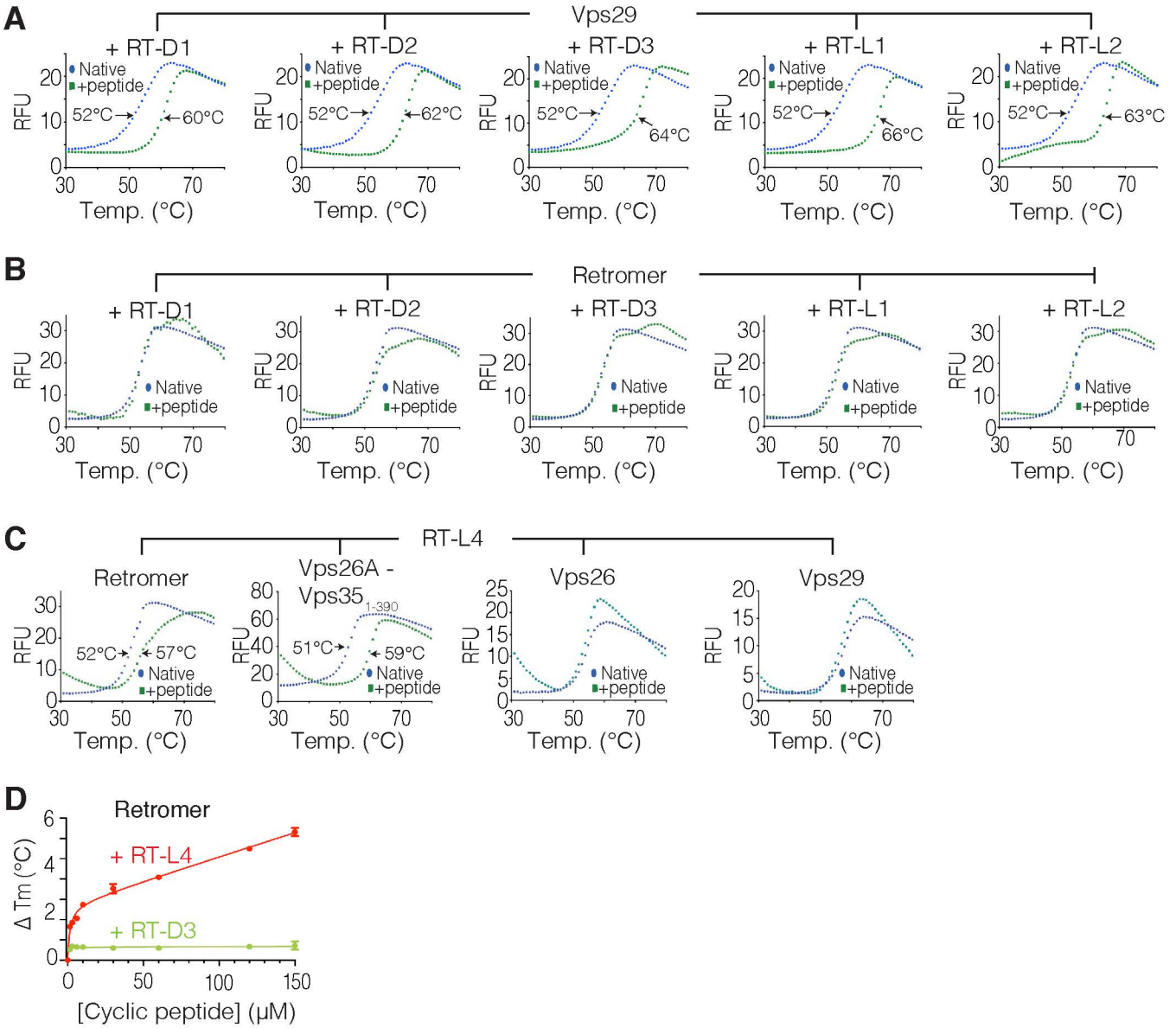

Figure S4. RT-L4 enhances the thermal stability of Retromer in solution.
(A) Temperature dependent unfolding of Vps29 in the presence of 30-fold molar excess of RT-D1, RT-D2, RT-D3, RT-L1 and RT-L2. (B) Temperature dependent unfolding of native Retromer in the presence of 30-fold molar excess of RT-D1, RT-D2, RT-D3, RT-L1 and RT-L2 complexes, and (C) in the presence of 30-fold molar excess of RT-L4. Melting temperatures (Tm) were assessed by differential scanning fluorimetry. The sigmoidal curve is characteristic of cooperative thermal denaturation of a folded protein. A shift in melting temperature indicates the stabilization of the proteins upon the addition of cyclic peptide. (D) Dose-response curve of Retromer in the presence of RT-L4 (red line) or RT-D3 (green line).

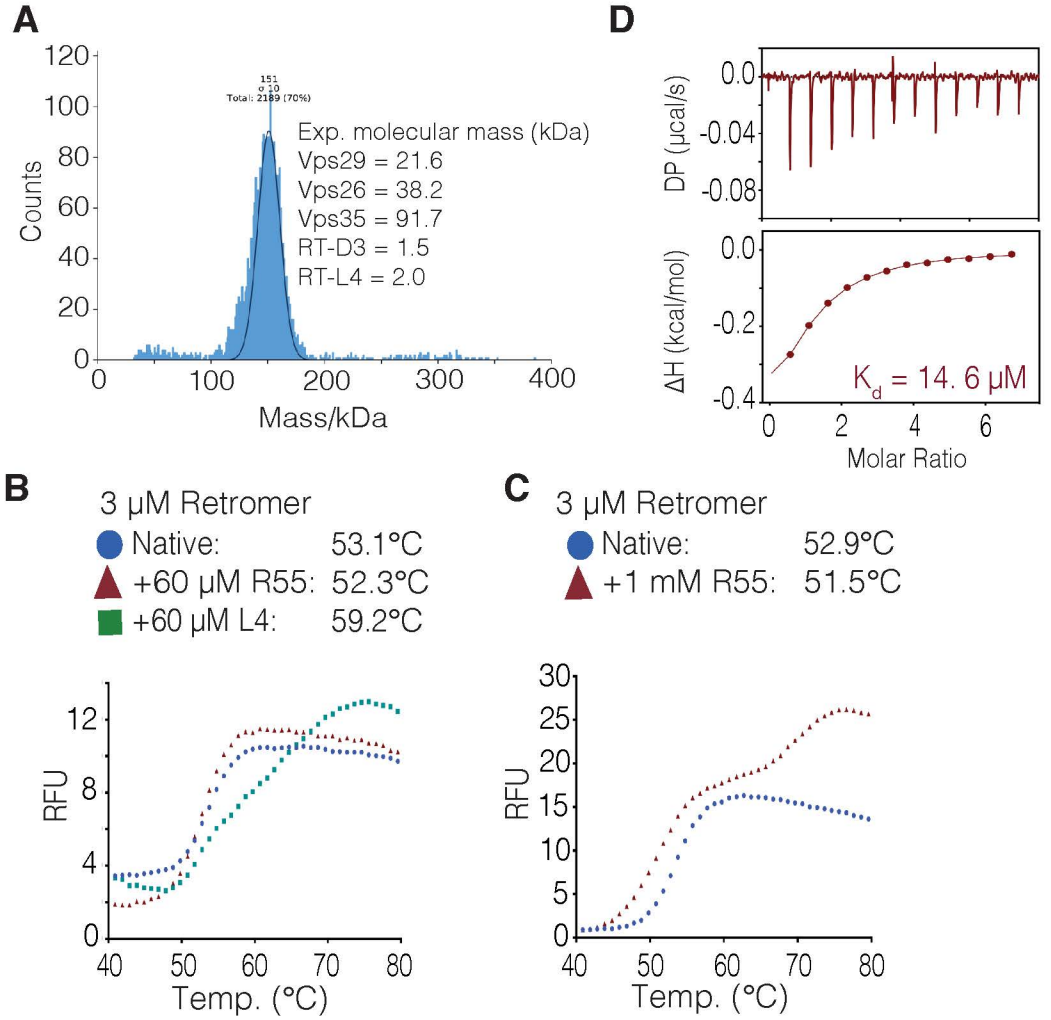

Figure S5. R55 does not significantly increase the thermal-stability of Retromer.
(A) Molecular mass of Retromer in the presence of RT-D3 and RT-L4 monitored by mass photometry. In this experiment, Retromer shows a mass of 151 kDa, corresponding to the heterotrimeric state of Retromer. (B) Temperature dependent unfolding of 3 µM Retromer (blue dot) compared with samples containing 60 µM of R55 (red arrow) or 60 µM RT-L4 (green square). (C) Same as (B) but with 1 mM of R55 showing two stages of unfolding. Note that preparation of 1 mM RT-L4 in aqueous buffer was not possible due to the lower solubility characteristics. (D) ITC thermogram for the titration of R55 with Retromer. The graph represents the integrated and normalized data fit with a 1 to 1 binding ratio. The binding affinity (Kd) is given as mean of three independent experiments.

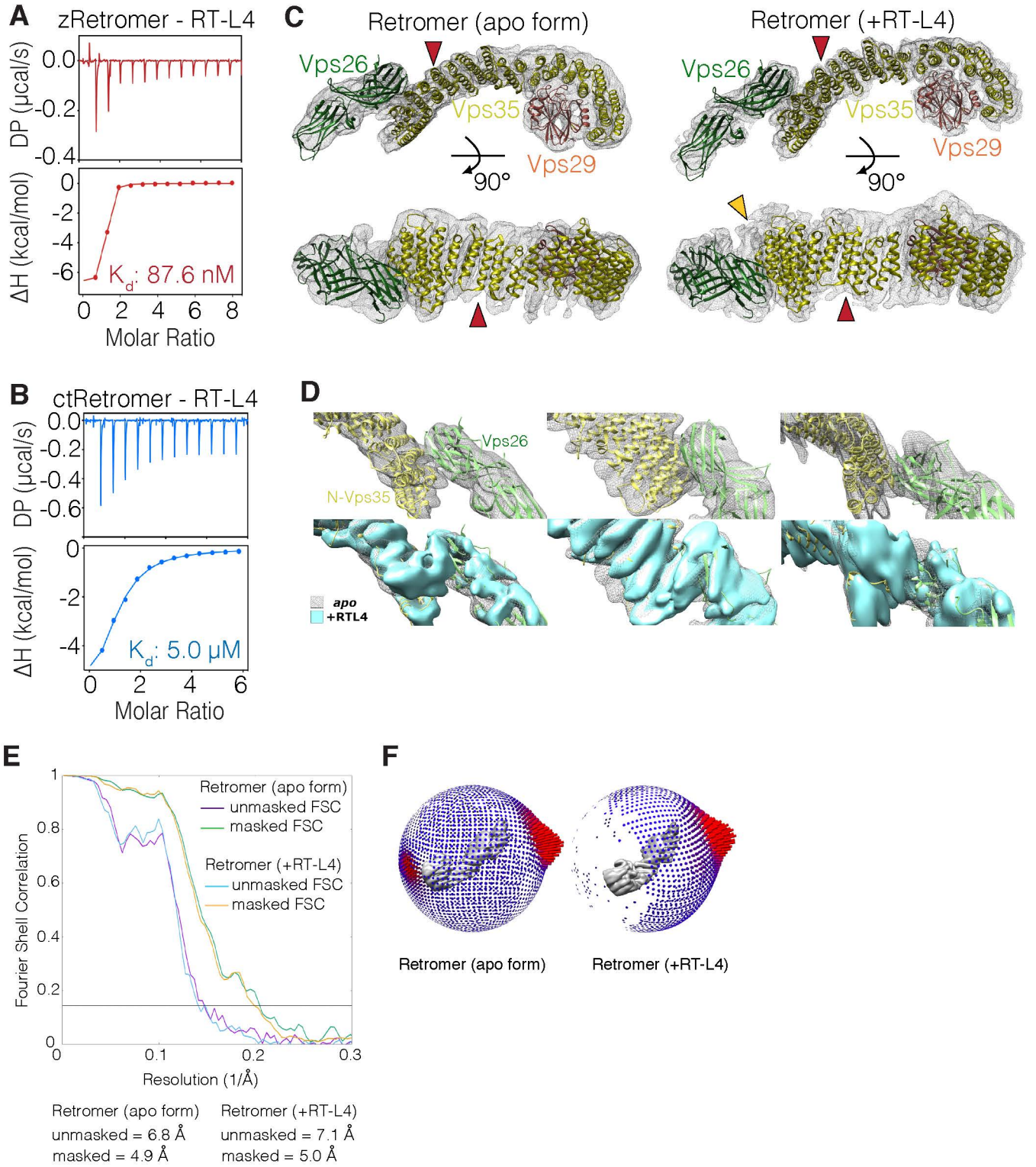

Figure S6. Binding of RT-L4 to Retromer from different species and assessed by cryoEM.
(A) ITC thermograms for the titration of RT-L4 with zebrafish Retromer showing a strong binding similar to human Retromer. (B) ITC thermograms for the titration of RT-L4 with C. thermophilum Retromer shows a lower affinity compared to zebrafish or human Retromer. The graphs represents the integrated and normalized data fit with a 1 to 1 binding ratio. The binding affinity (Kd) is given as mean of at least three independent experiments. (C) CryoEM density map of human Retromer (apo form) and in complex with RT-L4 displayed as mesh surface, with crystal structures of Retromer subcomplexes (PDB ID 2R17 and 5F0L) overlapped to the map. Red arrow indicates the Vps35 model fitting into α helices. Yellow arrow indicates the extra density observed between Vps26 and Vps35 interface in the RT-L4-bound Retromer. (D) Three different views of the Retromer CryoEM structure reconstructions highlighting the Vps35 and Vps26 interface. The cryoEM density from apo Retromer (grey mesh) is overlayed with the cryoEM density from RT-L4-bound Retromer (light blue surface). (E) Fourier Shell Correlation (FSC) plots highlighting masked and unmasked resolution estimates from RELION are shown for Retromer (apo form) and in complex with RT-L4. The intersections of the curve with FSC=0.143 (grey dotted line) are shown. (F) Angular distribution of the particles used for the final round of refinement. The height and colour of the cylinder bars is proportional to the number of particles in those views.

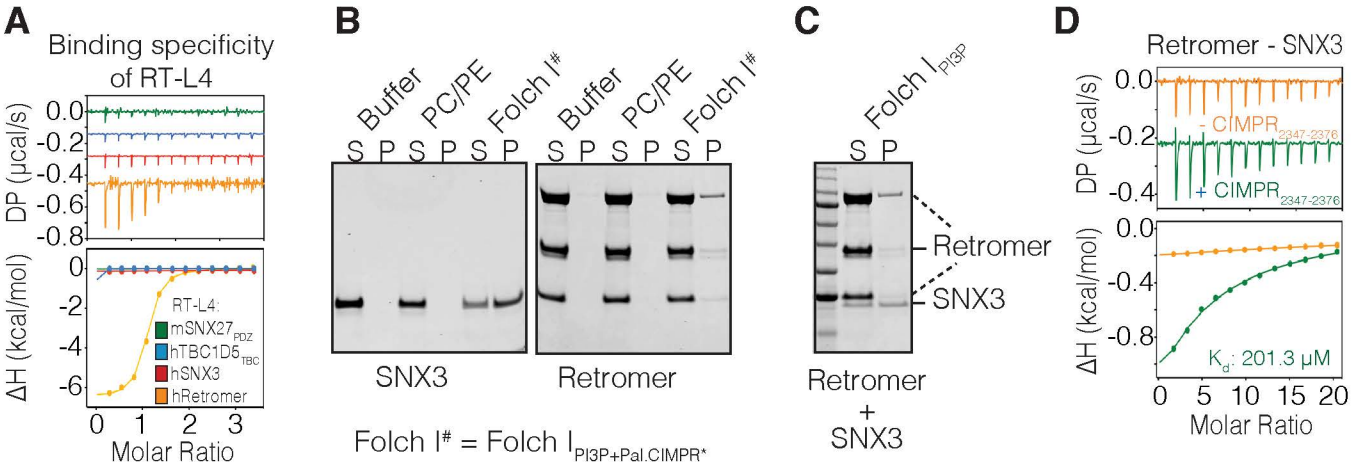

E

```
hVps26A    151 VHQLATYPDVNNSIKMEVGIEDCLHIEFEYNKSKYHLKDVIVGKIYFLLV
hVps26B    149 VHTLSTYPELNSSIKMEVGIEDCLHIEFEYNKSKYHLKDVIVGKIYFLLV
zfVps26A   151 VHQLATYPDVNNSIKMEVGIEDCLHIEFEYNKSKYHLKDVIVGKIYFLLV
ctVps26    147 VYSYRIPPELNSSIKMDVGIEDCLHIEFEYSKSKYHLKDVIVGRIYFLLV

hVps26A    201 RIKIQHMELQLIKKEITGIGPSTTTETETIAKYEIMDGAPVKGESIPIRL
hVps26B    199 RIKIKHMEIDIIKRETTGTGPNVYHENDTIAKYEIMDGAPVRGESIPIRL
zfVps26A   201 RIKIQHMELQLIKKEMTGIGPSTTTETETVAKYEIMDGAPVKGESIPIRL
ctVps26    197 RLKIKHMELSIIRRETTGVAPNQYNESETLVRFEIMDGSPSRGETIPIRL

hVps26A    251 FLAGYDPTPTMRDVNKKFSVRYFLNLVLVDEEDRRYFKQQEIILWRKAPE
hVps26B    249 FLAGYELTPTMRDINKKFSVRYYLNLVLIDEEERRYFKQQEVVLWRKGD-
zfVps26A   251 FLAGYDLTPTMRDVNKKFSVRYFLNLVLVDEEDRRYFKQQEIVLWRKAPE
ctVps26    247 FLGGFDLTPTFRDVNKKFSTRYYLSLVLIDEDARRYFKQSEIILYRQPPE

                 disordered tail
hVps26A    301 KLRK----QRTNFHQRFESPESQA--SAEQPE--------M
hVps26B    298 IVRKSMSHQAAIASQRFEGTTSLG--EVRTPSQLSDNNCRQ
zfVps26A   301 KMRK----R--NFHQRYESPEPRPSLSAEQPE--------M
ctVps26    297 YDN-----------QLLPPPPDQK--QVTAPLA--------
```

F

```
mVps35N     50 LGELRTSMLSPKSYYELYMAISDELHYLEVYLTDEFAKGRKVADLYELVQ
zfVps35N    50 LGELRTSMLSPKSYYELYMAISDELHYLEVYLTDEFAKGRKVADLYELVQ
ctVps35N    49 VSELRTSSLSPKQYYELYMAVFDALRYLSAHLRENHP-VNHLADLYELVQ

mVps35N    100 YAGNIIPRLYLLITVGVVYVKSFPQSRKDILKDLVEMCRGVQHPLRGLFL
zfVps35N   100 YAGNIIPRLYLLITVGVVYVRSFPQSRKDILKDLVEMCRGVQHPLRGLFL
ctVps35N    98 YAGNIIPRLYLMITVGTAYMSIDGAPVKELMKDMMDMSRGVQHPVRGLFL

mVps35N    150 RNYLLQCTRNILPDEGEPTDEETTGDISDSMDFVLLNFAEMNKLWVRMQH
zfVps35N   150 RNYLLQCTRNILPDDGEQAEEEMTGDINDSIDFVLLNFAEMNKLWVRMQH
ctVps35N   148 RYYLSGQARDYLPTGDS---DGPEGNLQDSINFILTNFVEMNKLWVRLQH
```

Figure S7. Binding of SNX3 and Retromer in the presence CIMPR2347-2376 cargo peptide.
(A) ITC measurements of RT-L4 with Retromer, SNX27PDZ, TBC1D5TBC and SNX3 demonstrate the binding specificity of the cyclic peptide to Retromer. (B) Liposome-binding assay of SNX3 and Retromer using Folch I liposomes containing 10% PtdIns(3)P and 10% N-terminal palmitoylated CIMPR2347-2376 peptide. (C) Liposome-binding assay of Retromer and SNX3 mixture as in (B) except Folch I liposomes contain only 10% PtdIns(3)P without the CI-MPR cargo. Retromer binds only weakly to Folch liposomes in the absence of either SNX3 or cargo sequence. In all three SDS-PAGE gels, "S" indicates unbound supernatant and "P" indicates bound pellet after ultracentrifugation. (D) ITC measurement of SNX3 with Vps26A –Vps351-390 subcomplex in the presence of CIMPR2347-2376 cargo peptide. The graph represents the integrated and normalized data fit with a 1 to 1 binding ratio. The binding affinity (Kd) is given as mean of at two three independent experiments. (E) Sequence alignment of the C-terminal region of Vps26 and (F) the N-terminal region of Vps35 showing the similarity between species. Key residues involve in contacts with Vps35 (yellow arrow) and Vps26 (blue dots) are labelled on top of the sequence. h, Homo sapiens; zf, Danio rerio; Ct, Chaetomium thermophilum; m, Mus musculus.

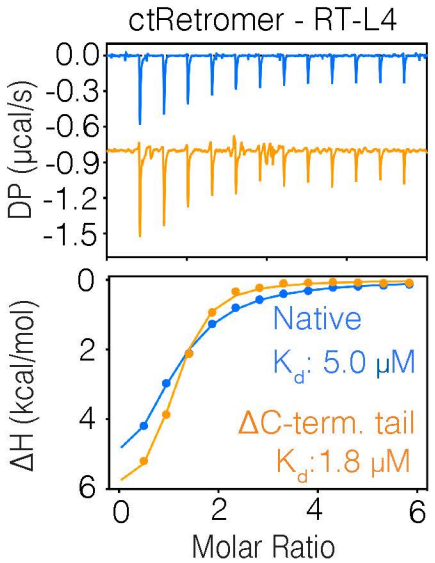

Figure S8. ctVps26 C-terminal disordered tail reveals similar autoinhibitory characteristics.
ITC measurement of RT-L4 with native and ctVps26 C-terminal tail truncated ctRetromer. The graph represents the integrated and normalized data fit with a 1 to 1 ratio binding. The binding affinity (Kd) is given as mean of at least three independent experiments.

GST-TBC1D5$_{TBC}$ pull-down with Retromer

Anti-Vps35

GST-Retromer pull-down with SNX3

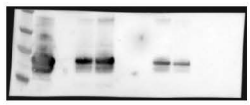

Anti-SNX3

GST-Retromer pull-down with SNX27

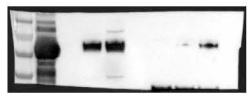

Anti-SNX27

GST-Fam21$_{R19-R21}$ pull-down with Retromer

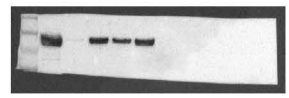

Anti-Vps35

Input lysate of biotinylated RT-D3/RT-L4 based pull-down

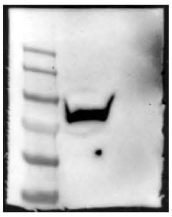

Anti-Vps35

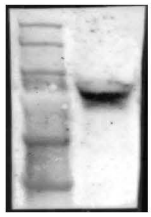

Anti-TBC1D5

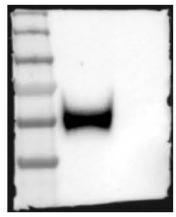

Anti-SNX27

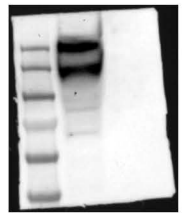

Anti-Fam21c

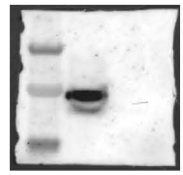

Anti-SNX3

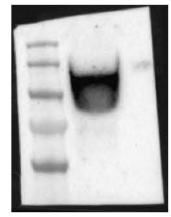

Anti-VARP

Pull-down samples of biotinylated RT-D3/RT-L4 based pull-down assay

Anti-Vps35

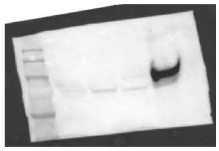

Anti-TBC1D5

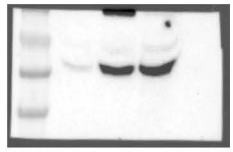

Anti-SNX27

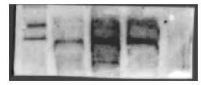

Anti-Fam21c

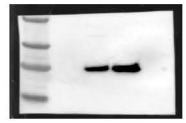

Anti-SNX3

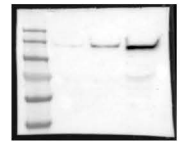

Anti-VARP

Figure S9. Unprocessed original scans of western blots for the main figure.
Unprocessed images of all blots in this study.